CONSTITUTIVE MODELING OF PHOTOPOLYMERIZATION AND ITS APPLICATION TO 3D PRINTING

A Dissertation
Presented to
The Academic Faculty

by

Jiangtao Wu

In Partial Fulfillment
of the Requirements for the Degree
Doctor of Philosophy in the
George W. Woodruff School of Mechanical Engineering

Georgia Institute of Technology
August 2018

CONSTITUTIVE MODELING OF PHOTOPOLYMERIZATION AND ITS APPLICATION TO 3D PRINTING

Approved by:

Dr. H. Jerry Qi, Advisor
School of Mechanical Engineering
Georgia Institute of Technology

Dr. Meisha L. Shofner
School of Materials Science and Engineering
Georgia Institute of Technology

Dr. Thomas Kurfess
School of Mechanical Engineering
Georgia Institute of Technology

Dr. Min Zhou
School of Mechanical Engineering
Georgia Institute of Technology

Dr. David W. Rosen
School of Mechanical Engineering
Georgia Institute of Technology

Date Approved: June 14, 2018

Dedicated to my loving grandmother, parents and my wife

ACKNOWLEDGEMENTS

First I would like to take this opportunity to express my deepest gratitude to my advisor Prof. H. Jerry Qi for his invaluable guidance and support during my Ph.D. study. Prof. Qi always provides me insightful suggestions when I encounter research problems. He dedicated a lot of time to discussing my research and helping me improve the quality of my papers. Without his dedication, I would not be able to finish this thesis. I would also like to thank my thesis committee members: Prof. Thomas Kurfess, Prof. David W. Rosen, Prof. Meisha Shofner and Prof. Min Zhou, for their suggestions regarding my thesis and their precious time serving as my Ph.D. proposal and defense committees.

The Special thanks go to my previous and current lab members. Particularly, I would like to thank Craig Hamel, Zeang Zhao, Chao Yuan, Dr. Yiqi Mao, Dr. Xiaoming Mu, Dr. Kai Yu, Dr. Xiao Kuang, Conner Dunn, Devin Roach, Vincent Li, Xirui Peng, Quanyi Mu, Qian Shi, Ming Lei, Kaijuan Chen, Le An and Dr. Hua Yang for their help on my research and all the good time I had with them.

Finally, I would like to thank my grandma and my parents for giving me all they have and their endless love and support. I did not have a chance to talk about my life here with my grandma and I miss her. I thank my wife Xiaona Li for her unconditional love, accompanying, encouragement and giving me a comfortable family life, without which I could not get through these stressful days.

TABLE OF CONTENTS

LIST OF TABLES

LIST OF FIGURES

LIST OF SYMBOLS AND ABBREVIATIONS

The following table lists universal abbreviations and symbols used in this dissertation.

3D	Three Dimensional
DLP	Digital Light Processing
DoC	Degree of Conversion
DSC	Differential Scanning Calorimetry
FTIR	Fourier transform infrared spectroscopy
PEGDA	Polyethylene (glycol) Diacrylate
ATR	Attenuated Total Reflection
DMA	Dynamic Mechanical Analysis
TTS	Time-temperature Superposition
EPM	Effective Phase Model
CAD	Computer Aided Design
SMP	Shape Memory Polymer
RSC	Reversible Shape Change

DMD	Digital Micromirror Device
UV	Ultraviolet
IR	infrared
FEA	Finite element analysis
p	Degree of Conversion
T_g	Glass transition temperature
C_I	Initiator concentration
C_O	Concentrations of Oxygen
C_{R}	Concentrations of Radicals
C_{M}	Concentration of unconverted C=C double bonds
kp	Propagation rate
k_{Term}	Termination rate
$k_{t,D}$	Termination rate due to species translational diffusion of radicals
$k_{t,RD}$	Termination rate due to reaction diffusion
k_{O}	Reaction rate between oxygen and radicals

τ_n Relaxation time

Λ Volume shrinkage

ρ Density

I Light intensity

A Local depletion rate of light intensity due to the absorbance of the species

$\boldsymbol{\Omega}$ Direction of light propagation

β Photodecomposition rate

C_{RD} Reaction diffusion proportion parameter

k_{p0} Polymerization rate at p=0

E_r Activation energy of transition from the glassy to the rubbery state

$\mathbf{G}$ Deformation gradient

$\mathbf{F}$ Mechanical deformation gradient

$\boldsymbol{\sigma}$ Cauchy stress

Δf_m Crosslink fraction

N_M Total crosslinks of the fully cured polymer

$\overline{f}$ Effective crosslink fraction

E_{eq} Equilibrium modulus

$\mathbf{B}$ Left Cauchy–Green deformation tensor

κ Bulk modulus

μ Shear modulus

$\mathbf{E}_n^e$ Hencky strain of n-th branch

$\mathbf{L}_n^e$ Fourth order isotropic elastic tensor of n-th branch

$\mathbf{D}_n^v$ Viscous stretch rate of n-th branch

$\overline{s}_n$ Equivalent stress of the n^{th} branch

S_n Athermal shear strength

ΔG Activation energy

E_n Elastic modulus of n-th branch

W_a Weight percentage of the photoabsorbers

K Photochemical reaction rate

D Total light dose

α_d Volume shrinkage during the desolvation

α_s Volume ratio after the swelling

λ Lamês first parameter

SUMMARY

Photopolymerization is widely used in many engineering applications such as coating, dental restoration and 3D printing. It is a complex chemical and physical process, through which a liquid monomer solution is rapidly converted to a solid polymer. Many photo curable materials shrink during the photopolymerization process due to the chemical reaction volume shrinkage, which can induce the residual stress in the photocured parts. The residual stress can cause the distortion and warpage of the photocured parts, which affects the accuracy and functionality of the 3D printed structures. Therefore the constitutive modeling for the photopolymerization is important for it applications. In this research, the free-radical photopolymerization reaction kinetics and material property evolution during the curing process are investigated by experiments and theoretical modeling. The model can be applied to investigate the internal stress development of the photocured parts caused by the volume shrinkage during photopolymerization. The constitutive model was utilized to simulate the material property evolution and mechanics during the digital light processing (DLP) 3D printing process. Through FEM simulation, we calculated the print through error, volume shrinkage induced distortion of the DLP printed structure and the results are compared with the experiments. In addition, a simplified theoretical model was built for the DLP grayscale 4D printing. Structures and devices with reversible shape change (RSC) are highly desirable in many applications such as mechanical actuators, soft robotics and artificial muscles. The grayscale pattern was used to control the light intensity distribution of the UV projector in a digital light processing (DLP) 3D printer such that

the same photo irradiation time leads to different curing degrees and thus different crosslinking densities at different locations in the polymer during 3D printing. After leaching the uncured oligomers inside the loosely cross-linked network, bending deformation could be induced due to the volume shrinkage. The bending deformation was reversed if the bent structure absorbed acetone and swelled. Using this 4D printing method, we designed and created RSC structures. The desolvation based 4D printing was studied using experiments and our constitutive modeling. In summary, this dissertation presents the constitutive modeling of the material property evolution and mechanics in free radical photopolymerization and its applications to 3D printing and 4D printing. Compared to previous research on photopolymerization mechanics model, the model in this dissertation considers the detailed material property evolution process, the non-linear viscoelastic property of the material, and the coupling of the material property evolution and mechanical deformation. Therefore it can provide better understanding of the complex material property evolution and mechanical deformation coupling process.

CHAPTER 1. INTRODUCTION

1.1 Background

1.1.1 *Overview*

Photopolymerization is a chemical reaction process which combines small monomer molecules to form a polymer by using light activation. Photopolymerization has been widely used in many engineering fields such as coating, dental restoration, tissue engineering 3D printing and 4D printing [1-15], because of its advantages, including high rates, energy efficiency and freedom from solvents[2,3,16-18]. Although photopolymerization has many advantages, there are still some problems when we apply it to the engineering applications. During the photopolymerization, small monomers connect with each other through the chemical reaction and the original van der Waals forces between molecules are replaced by the covalent bond, which reduces the distance between molecules and causes the volume shrinkage of the photocured material [19-35]. The volume shrinkage of the curing material can induce the residual stress in the photocured parts, which causes the distortion and warpage of the photocured parts, and affects the accuracy and functionality of the 3D printed structures. Therefore, it is important to investigate the mechanics during photopolymerization. Here in this research, the photopolymerization reaction kinetics, material property evolution and mechanics during the free-radical photopolymerization were investigated by experiments, theoretical modeling and FEM simulations. And the theoretical model was implemented in the FEM simulation to investigate the distortion of the DLP 3D printed structure. In addition, a simplified

theoretical model for photopolymerization and desolvation induced reversible shape change was built for investigating the DLP grayscale 4D printing.

1.1.2 *Photopolymerization and reaction induced volume shrinkage*

Polymerization is a chemical reaction that combines small monomer molecules to form a polymer. There are two basic types of polymerization: step polymerization and chain polymerization [36]. In step polymerization, the chemical reaction proceeds stepwise between two reactants by combining their functional groups. A typical example is the formation of nylon 6/6, which is produced by the reaction between hexamethylene diamine and adipic acid. Usually step polymerization is slow. In chain polymerization, the chemical reaction needs to be initiated by catalysts such as free-radical initiators, cationic and anionic initiators. After initiation by a catalyst, the monomers obtain the ability to react with functional groups of other monomers. The monomer chains begin to connect with each other and the main chains grow until they are terminated by other reactive groups. Although the reaction rate can be tuned by the types and concentrations of the initiator, chain polymerization generally proceeds rapidly.

Free radical chain polymerization is the most commonly used method in commercial synthetic polymers [18,37] because it does not require stringent reaction conditions and can be widely applied to various types of monomers. Depending on how radicals are generated, the free radical chain polymerization can be activated by light, voltage, chemical redox triggers and mechanical force[1]. Among these methods, photopolymerization or photocure, where light is used to trigger free radical polymerization, is widely used in many engineering fields [2,38]. In particular, because

photopolymerization can cure a polymer very rapidly, it is one of the most widely used methods in 3D printing [4,9,10,39,40,41 ,42,43]; this is evidenced by the fact that photopolymers are the most consumed 3D printing materials, claiming almost half of 3D printed materials market [44-46].

Figure 1.1 shows the typical photopolymerization process in the photocuring based 3D printing [47]. The light first excites the photoinitiators and the photoinitiators decompose into free radicals after obtaining the energy from light. The free radical then can attack the monomers to activate the polymerization reaction. The active monomer then can connect with other monomers to form the polymer chains. With increase of the polymer chains, the material will increase its molecular weight and become the solid material.

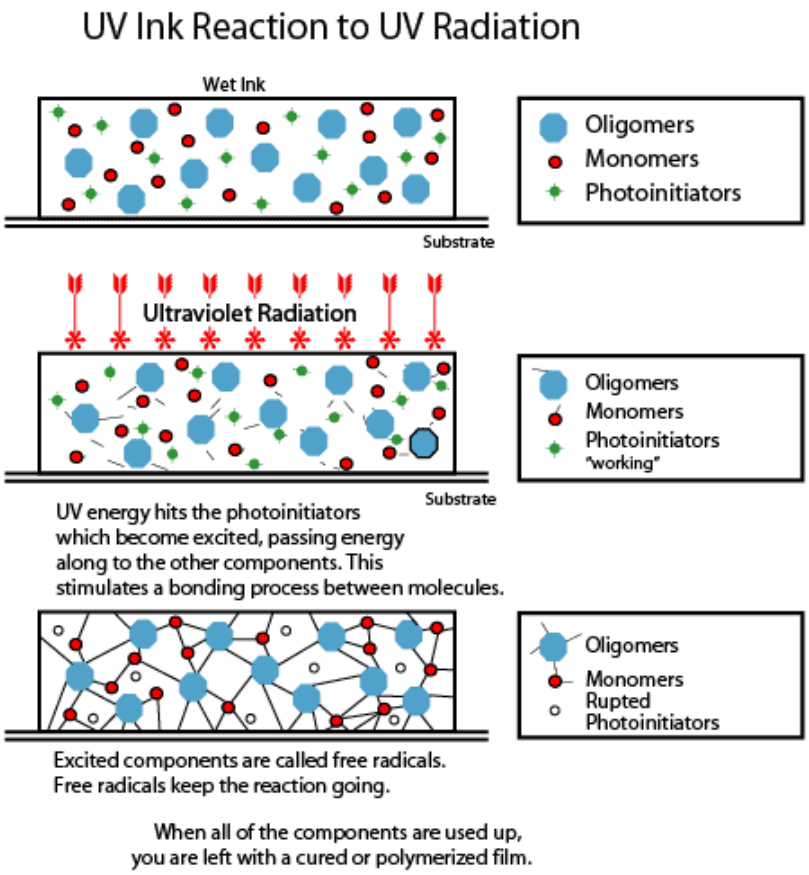

Figure 1.1 The typical free radical photopolymerization reaction process [47].

We already know that the volume shrinkage is a common phenomenon in the photopolymerization process [19-35] and the volume shrinkage can cause internal stress and the distortion of the photocured parts. Figure 1.2 shows two examples. Figure 1.2(a) shows the phenomenon of the fracture or gaps and internal stress in the photocuring based dental restoration[23]. Figure 1.2(b) shows volume shrinkage induced shape distortion of a stereolithography printed thin strip[21]. These two examples indicate that the volume shrinkage is a severe problem in the photocuring applications. But in some cases, we can also utilize the volume shrinkage induced internal stress for the self-folding structures as shown in Figure 1.3[10]. In this example, the nonuniform conversion inside the

DLP photocured thin sheet caused by the photoabsorber induced light attenuation in the thickness direction leads to the nonuniform volume shrinkage and internal stress. After removed from the curing stage, the nonuniform residual stress will bend the structure. By utilizing the internal stress, we can create self-folding origami. From these examples we can see that the volume shrinkage could be harmful to the accuracy of the photocured parts but also could be useful for other applications. Therefore a theoretical model to describe the photocuring process and volume shrinkage induced internal stress is critical for us to utilize the photopolymerization. In this research, the photopolymerization process will be investigated by experiments and theoretical modeling.

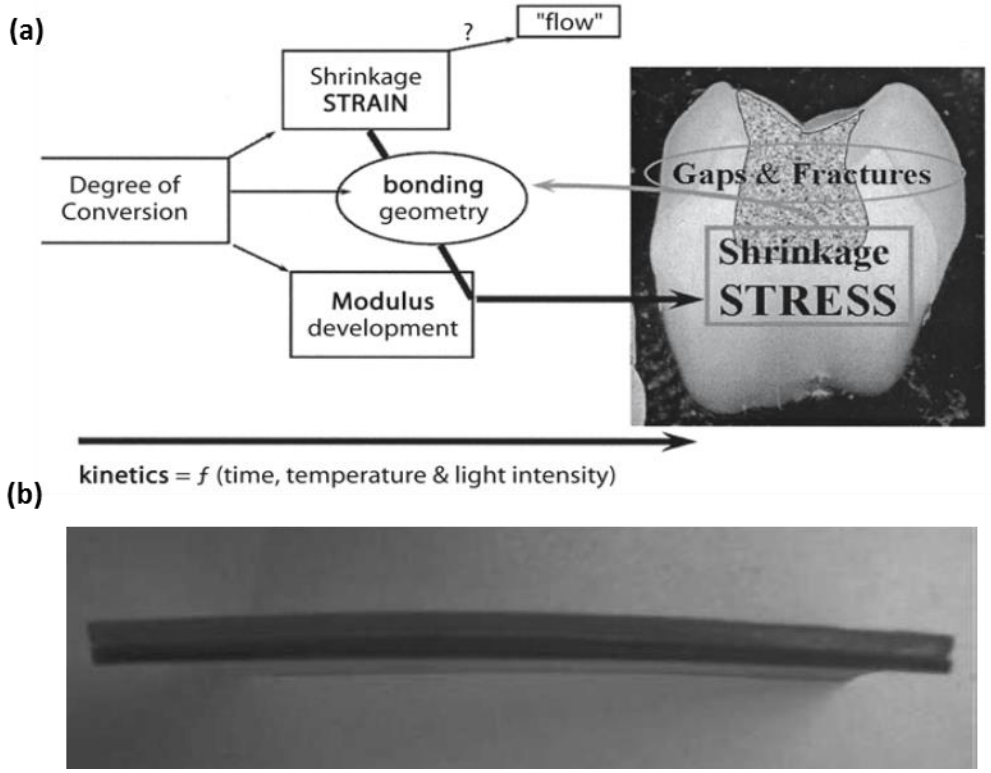

Figure 1.2 The volume shrinkage phenomena during polymerization shrinkage. (a) Stress induced by volume shrinkage in the dental restoration[23]. (b) The volume

shrinkage induced shape distortion of a stereolithography printed acrylic photopolymer laminate [21].

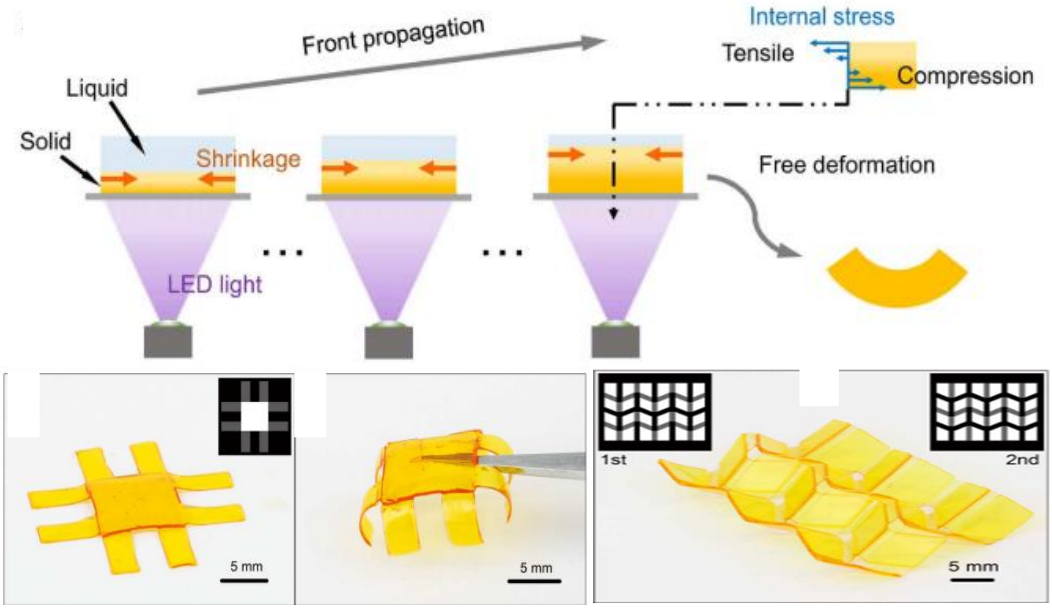

Figure 1.3 The volume shrinkage induced internal stress during photopolymerization for self-folding origami structures[10].

1.1.3 *DLP 3D printing and shape distortion*

DLP 3D printing or Mask Projection Stereolithography (MPSLA) is an advanced additive manufacturing technology which produces the 3D structures through layer-by-layer photopolymerization process[14,48-53]. Figure 1.4 shows the typical DLP 3D printing process [50]. Usually, the DLP printing system includes at least three parts as shown in Figure 1.4: the resin vat, moving stage for the movement of the printing stage in Z direction and the light projector with Digital Micromirror Device (DMD) [14,40,48-53]. The designed 3D structure is first sliced into different layers by the specific slicer software and the image of each sliced layer will be used for printing. The sliced layer image is then exported to the light projector. The digital light projector with DMD then projects

the image to the liquid resin surface and cures the liquid polymer resin into a solid thin layer. Each layer is exposed to the light for a few seconds to dozens of seconds. Then the moving stage moves to the new layer position and a new layer of resin is cured. Through this layer-by-layer material adding process, a 3D structure can be printed. The printing resin usually consists of monomers, photoinitiators, and photoabsorbers. Photoabsorbers are added for reducing the light penetration depth and avoiding the overcuring. During the photopolymerization 3D printing, each layer except the last layer will experience multiple light exposures due to the light penetration [48]. The light penetration is helpful for binding the printing layer to previous layer and building strong interfaces, but it also causes the dimension error in the height direction [48]. Limaye and Rosen [48] investigated the print through error with theoretical modelling and experiments. The overcured depth due to the print through is linked with the total light exposure and was utilized to optimize the geometry of the printing structure to reduce the print through error.

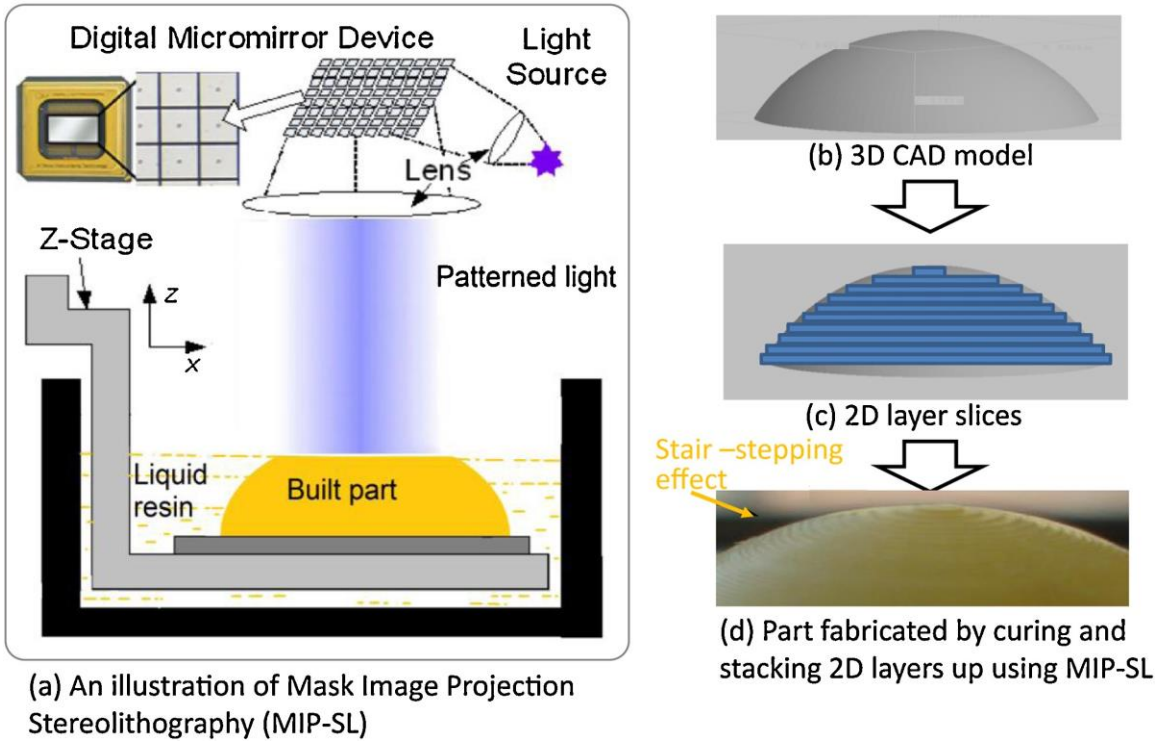

Figure 1.4 The typical DLP 3D printing process [50].

In addition to the print through error, the shape distortion is another problem that affects the accuracy of the printed structure [21,24,54-56]. In last section, we have seen that the reaction volume shrinkage could cause the nonuniform internal stress inside the 3D printed parts and the distortion deformation of the DLP printed structures (Figure 1.2(b)). Previously, Huang et al. applied the dynamic finite element method (FEM) to simulate the curl distortion of the stereolithography printing caused by the temperature change during laser scan [54]. In their method the modulus change and temperature induced volume change are related to the averaged energy dose and curing time by empiric equations. For many materials, the temperature change during the curing process is lower than 10℃ and the material under printing is surrounded by the room-temperature uncured liquid resin. Therefore the thermal expansion volume change is relatively small comparing to the

reaction induced volume change. In this research, the constitutive model for the photopolymerization will be applied to FEM simulation to simulate the layer-by-layer DLP printing process, the print through error and volume shrinkage induced distortion.

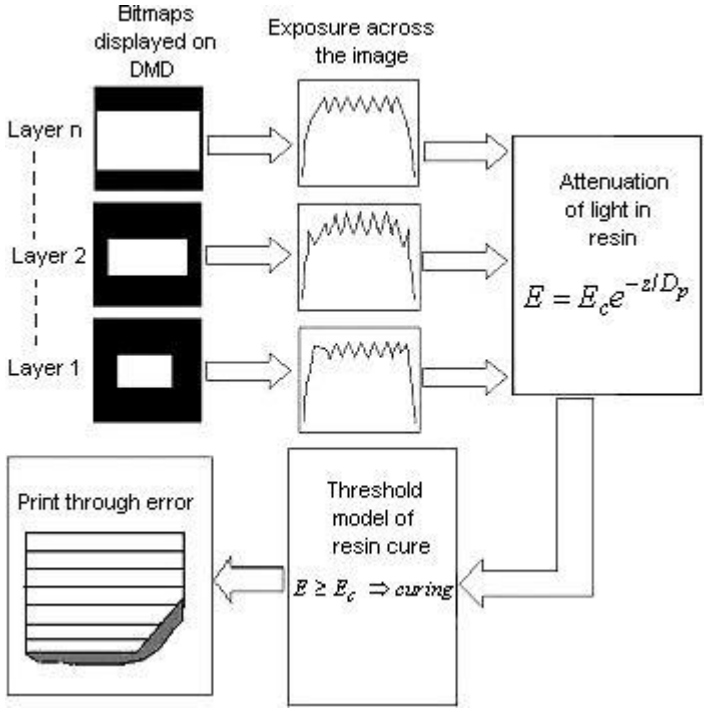

Figure 1.5 The print through error in the DLP printing [48].

1.1.4 *4D printing and DLP grayscale pattern 4D printing*

The 3D printing technology has been applied to fabricate active or smart materials [57-61], which added another dimension to 3D printing. After being printed, these active materials can change their shape over time when subjected to external stimuli such as temperature [62-66], light [67-69], electricity [70-72] and magnetic fields [73-75], which has been called 4D printing[76-80]. Ge et al. created active shape memory composites by 4D printing where shape memory polymer (SMP) fibers were used to activate the shape change of the printed composites[58,81]. Tibbits et al. provided a new design of complex self-evolving

structures by 4D printing hydrophilic materials which can form stretching, folding and bending deformation when subject to hot water[82]. Bakarich et al. has created thermally actuating hydrogels that can be used as a valve to control the flow of water by automatically closing upon exposure to hot water and opening in cold water[83]. By combining the advantages of smart materials and the advanced 3D printing technology, 4D printing provides the tremendous opportunities for designing and fabricating smart structures efficiently and easily.

Recently, Zhao et al. [9] used the grayscale pattern to control the light intensity distribution of the DLP projector and fabricated structure with nonuniform crosslinks density by digital light photopolymerization, as shown in Figure 1.6. The photoabsorber was used to induce the intensity gradient along the light propagation path and the nonuniform crosslink density can be formed due to the intensity gradient. These structures with nonuniform crosslink density are utilized to create active structures. After photocuring, the structure was immersed in the water and the uncured monomers in the less crosslinked part can be washed away, which is called the desolvation approach. Due to the loss of the monomers, the volume of the less cross-linked part would shrink, which can be used to create active bending structures if the distribution of the crosslink density was well designed (Figure 1.6(b)-(c)). And if the bended structure was dried and immersed into a good swelling solution such as acetone, the smaller swelling solution can occupy the space of the contracted part and the structure can recover to the original shape. Therefore the fabricated structure can be activated by the swelling solution. The nonuniform crosslink density can also be controlled by the grayscale pattern. With low grayscale value, the light intensity will be lower. Using this way the self-folding

structures have been fabricated as shown in Figure 1.6(d)-(e). This method provides another possible mechanism for 4D printing. In the method, only 2D planar grayscale level patterns are used to generate the active structures. In this research, we will extend this digital light processing method to 3D printing active structures. We can create 3D structures with different crosslink density in different parts by controlling the grayscale level of the sliced printing image and activate the structure by using the desolvation approach. During the 3D printing process, each printed layer subjects to multiple light exposures and the conversion degree of each part determines the curvature of the printed sample. A theoretical model will be used to predict the conversion and the bending curvature, which can be used to help the design of the active structure.

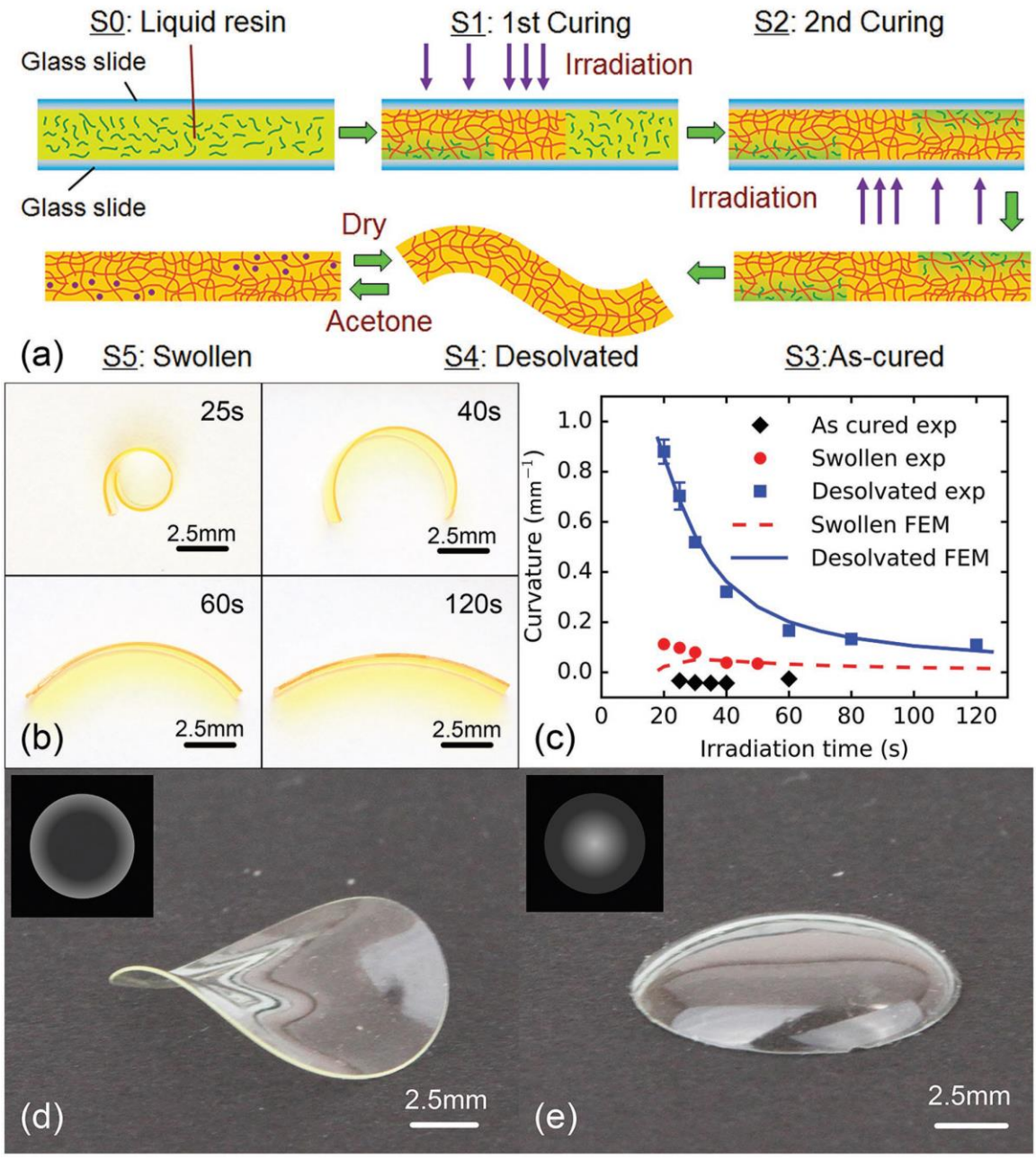

Figure 1.6 The DLP method for creating active structures[9]. (a) The mechanism of DLP grayscale pattern 4D printing. (b) The bending deformation created by the desolvation induced volume shrinkage. (c) The bending curvature after desolvation and swelling as the function of photocuring time. (d) The saddle plate and (e) dome plate created by nonuniform in-plane irradiation.

1.2 Thesis plan

This dissertation research is organized as follows. The constitutive modeling of radical photopolymerization process is investigated in Chapter 2. Then the simulation of the photopolymerization based 3D printing process is studied in Chapter 3. And the DLP Grayscale 4D printing - desolvation induced shape changing is investigated in Chapter 4. The overall conclusion is included in Chapter 5.

CHAPTER 2. CONSTITUTIVE MODELING OF RADICAL PHOTOPOLYMERIZATION PROCESS

2.1 Introduction

Polymerization is a chemical reaction that combines small monomer molecules to form a polymer. There are two basic types of polymerization: step polymerization and chain polymerization [36]. In step polymerization, the chemical reaction proceeds stepwise between two reactants by combining their functional groups. A typical example is the formation of nylon 6/6, which is produced by the reaction between hexamethylene diamine and adipic acid. Usually step polymerization is slow. In chain polymerization, the chemical reaction needs to be initiated by catalysts such as free-radical initiators, cationic and anionic initiators. After initiation by a catalyst, the monomers obtain the ability to react with functional groups of other monomers. The monomer chains begin to connect with each other and the main chains grow until they are terminated by other reactive groups. Although the reaction rate can be tuned by the types and concentrations of the initiator, chain polymerization generally proceeds rapidly. Free radical chain polymerization is the most commonly used in commercial synthetic polymers [18,37] because it does not require stringent reaction conditions and can be widely applied to various types of monomers. Depending on how radicals are generated, the free radical chain polymerization can be activated by light, voltage, chemical redox triggers and mechanical force [1]. Among these methods, photopolymerization or photocure, where light is used to trigger free radical polymerization, is widely used in many engineering fields such as coating, dental restoration, and 3D printing [1-5,40,48], because of its many

advantages, including high rates, energy efficiency and freedom from solvents [2,3]. In particular, because photopolymerization can cure a polymer very rapidly, it is one of the most widely used methods in 3D printing [4,9,10,39]; this is evidenced by the fact that photopolymers are the most consumed 3D printing materials, claiming almost half of 3D printed materials market [44-46]. However, photopolymerization is also a complex chemical and physical process: The liquid monomer solution experiences a rapid liquid-to-solid phase transition in a few to a few tens of seconds; the molecular weight, polymer chain length and crosslink density evolve with the degree of conversion. These changes in microstructure during the curing process influence macroscopic material properties such as Young's Modulus, relaxation time, glass transition temperature, volume shrinkage, and deformation. Large volume shrinkage during curing also causes the development of residual stress, or warping of the photo-cured parts, which affects the accuracy of the 3D printed structure[24-26]. Therefore, it is critical to investigate the material property evolution to obtain better control of the properties[54,55,84].

To study material property changes during the photopolymerization process, it is necessary to model the kinetics of the chemical reactions, describe the evolution of the curing solution's species composition and link the physical properties with the composition. The chemical reaction kinetics of photopolymerization was widely investigated [85-90]. For example, the simplified phenomenal model by Atai and Watts [28] treats the relative conversion of monomers as the only variable to characterize the polymerization process and ignores the variations of other species. Another popular model uses the first-order reaction equations to describe the concentration variations of individual species [91-94], which typically include photoinitiators, free radicals and

monomers. In this method, the rates depend on the reactant concentrations, reaction constants, and reaction conditions (such as light intensity), from which one can obtain all the information on the concentrations of individual species and the detailed reaction process. Therefore, this method is widely used in modeling the photopolymerization system. It should be noted that the polymerization rate is also controlled by the diffusion of species, and thus the reaction rate changes with the increase of viscosity during curing [95-97]. The diffusion-controlled termination occurs when the mobility of the large growing polymer chains is hindered. In such a case, the termination rate of two active polymer chains decreases, because their mobility is limited and the polymer chains need to grow long enough to find another polymer chain to terminate the reaction. The decrease of the termination rate causes a dramatic increase in the rate of conversion. This process is called auto acceleration or gel or Trommsdorff effects [98]. As the viscosity of the system increases to a very high level, the diffusion ability of smaller monomers is also restricted, which causes a decrease in the propagation rate, and the rate of the conversion becomes very slow. Rate variation during the photocuring is an important feature and should be included in a comprehensive understanding of the curing process.

To link the photopolymerization reaction process with material property evolution, one needs to find proper characterization parameters to represent the evolution of the polymerization system. As the photopolymerization reaction proceeds, the monomers grow into long polymer chains, and crosslink occurs between polymer chains. It is straightforward to think that if one would describe the number distribution of polymer chains with different chain lengths, one should be able to calculate the material properties by the superposition method. However, this could quickly become a daunting job due to

the complex distribution functions of the practical polymer branches. Another way to solve this problem is to use the degree of conversion (DoC) of the monomers or the functional groups as the internal variable; many material properties can be linked as the functions of the DoC. In addition, the DoC of the functional groups is a good indication of the averaged composition of the system, and it is easier to measure than the distribution of polymer chains. For example, the DoC can be measured through reaction entropy by differential scanning calorimetry (DSC), infrared spectroscopy absorbance by Fourier transform infrared spectroscopy (FTIR) and the NMR spectrum. Because of these, the DoC is often used to characterize and model the property changes during curing for thermosetting epoxy and adhesives. To investigate the viscoelastic properties, the time-temperature superposition principle can be used to describe the effects of temperature on the time scale of the mechanical behavior [99,100]. The crosslink effects on the time response of cured material are described by the time-conversion supposition [101]. In addition, as the curing proceeds, the glass transition temperature (T_g) of the curing system increases and may become higher than the curing temperature; this results in the cured material entering a glassy state, which could exhibit nonlinear viscoelastic behaviors. Therefore a model that can describe the stress-strain behavior of the cured glassy polymer at large deformation is needed.

From a continuum mechanics point of view, polymerization is a continuous microstructure evolution process, which is always coupled with a mechanical deformation or an external load, such as curing shrinkage deformation or the constraint from the reaction vessel. During the polymerization process, newly formed crosslinks are added to the old crosslinked polymer network. If deformation is introduced at the same

time (such as volume shrinkage), the newly formed crosslinks are found to be in stress free configuration [102]. This is similar to the concept of natural configuration, or phase evolution, which was used by many different groups in studies of materials where new phases or microstructures are formed. For example, Rajagapol, Srinivasa, Wineman, and Negahban [103-106] studied the mechanics of solids with formations of crystal; Wineman and Shaw studied the scissoring and healing of rubbers [107,108]. Long et al. applied this concept to study photomechanics in light activated polymers [93] and developed a general theory for hyperelastic materials [109]. Hossain et al. [110,111] developed the hypoelastic type model, which calculates the stress by using the rate form. Westbrook et al. [112] and Ge et al. [113,114] developed a phase evolution model to capture the same phenomena in stretch induced crystallization behavior.

In this chapter, both experiments and theoretical modeling are used to investigate the free-radical photopolymerization reaction kinetics, material property evolution and mechanics during the photopolymerization process. The experiments to characterize the DoC and the evolution of thermomechanical properties are conducted. For the constitutive model, the photopolymerization reaction kinetics is modeled using the first-order reaction equations. The DoC of the functional group is then used as an internal variable to characterize the reaction system. The glass transition temperature and the viscoelastic properties of the cured polymer are linked to the DoC. The time-temperature-DoC superposition is applied to capture the thermomechanical behaviors of the cured polymer. A parametric study was conducted to investigate how light intensity and photoinitiator concentration affect the curing process. A finite deformation model based on the phase evolution concept is also developed to describe the coupling of mechanical

deformation and material property evolution during curing. Finally, the finite element simulation using the developed constitutive model is applied to simulating the internal stress evolution and bending curvature due to volume shrinkage of a thick sample during the photopolymerization process. The research work presented in this chapter has been published in *Journal of the Mechanics and Physics of Solids* [115].

2.2 Experiments and Results

2.2.1 *Materials and photopolymerization process*

In the present work, the monomer used was polyethylene (glycol) diacrylate (PEGDA) (Mn=250g/mol, Sigma-Aldrich, St. Louis, USA), which is widely used in biomedical applications and 3D printing. We used 3‰ weight percent 2,2-Dimethoxy-2-phenylacetophenone (Sigma-Aldrich, St. Louis, USA) as the photoinitiator. A reaction cell was made by clamping two glass slides that were separated by two plastic shims with the same thickness of 0.11mm to control the height of the solution. The mixed solution was then injected into the reaction cell along the open edge to avoid the effects of oxygen [88,116]. The ultraviolet (UV) light from a spot UV curing lamp (OmniCure S2000, Excelitas Technologies Corp., Waltham, Massachusetts, USA) with a 365nm wavelength bandpass filter was projected on the top of the reaction cell. The light intensity was controlled to be 5mW/cm^2 on the top surface of the solution. The DoC of the samples was controlled by the UV light exposing time. After curing with different exposure times, the samples were taken out of the reaction cells for characterization.

2.2.2 *Degree of conversion measurements*

The DoC was measured by an FTIR (Nicolet iS50, Thermo Fisher Scientific, Waltham, Massachusetts, USA) with the attenuated total reflection (ATR) accessory. The sample was scanned 32 times at a resolution of 1 cm^{-1} and the averaged result of these scans was used. During the polymerization process of the acrylates, the C=C bonds are opened and convert to a single bond in the polymer chains. The DoC of the C=C bonds can be characterized by the decrease of the infrared (IR) absorbance of the C=C bonds. Specifically, the conversion of the C=C bonds was calculated using the absorbance peak area under the absorbance spectra at the peak frequency 1620 cm^{-1} and 1635 cm^{-1}. To count differences in the samples, an internal standard that does not change during the chemical reaction is needed to normalize the peak absorbance value. In our case, the C=O stretching vibration peak at frequency 1725 cm^{-1} was used as the internal standard for the conversion analysis of each sample. The DoC p was calculated as:

$$p = 1 - \frac{(A_{1635cm^{-1}} + A_{1620cm^{-1}}) / A_{1725cm^{-1}}}{[(A_{1635cm^{-1}} + A_{1620cm^{-1}}) / A_{1725cm^{-1}}]_{t=0}} \tag{2-1}$$

where $A_{1620cm^{-1}}$, $A_{1635cm^{-1}}$, $A_{1725cm^{-1}}$ are the absorbance peak area at 1620 cm^{-1}, 1635 cm^{-1} and 1725 cm^{-1} respectively, and $[(A_{1635cm^{-1}} + A_{1620cm^{-1}}) / A_{1725cm^{-1}}]_{t=0}$ is the peak area ratio of the unreacted solution.

2.2.3 *Thermomechanical properties measurement and uniaxial tests*

To characterize the viscoelastic properties of the cured polymers, dynamic mechanical analysis (DMA) tests were performed using a DMA tester (model Q800, TA Instruments, New Castle, DE, USA) in film tension mode. The samples (dimension 10mm×4mm×0.13mm) were first heated to 90 ℃ for the sample cured for 100s, or to

around 30 ℃ above the T_g for others; the samples were then stabilized for 15 minutes to reach thermal equilibrium. A preload of 0.001N was applied to keep the sample straight during the test. During the DMA tests, the strain oscillated at a frequency of 1 Hz, with peak amplitude of 0.1%. At the same time, the temperature was decreased from 90 ℃ to 0 ℃ for the sample cured for 100s, or around 40 ℃ below the T_g for other samples, at a rate of 2 ℃/min. When the low temperature was reached, the sample was stabilized for 10 minutes; then the heating procedure started at a heating rate of 2 ℃/min. Due to the temperature rate effects, the curves from cooling and heating could not overlap and showed hysteresis loops [117]. We found that the average temperature of the peaks in the tanδ curve of the cooling and heating traces can present a good representation of T_g. The tan δ curves and storage modulus curves from cooling and heating were shifted along the temperature axis until the tanδ peaks overlaped at the averaged T_g. Then the shifted tanδ and dynamical storage modulus E' curves were used.

In order to characterize the time-temperature superposition effects, relaxation tests were performed on samples with different polymerization times, using relaxation mode. The pre-strain was set to be 0.15% and a 5 ℃ temperature interval was used. The time-temperature superposition (TTS) principal was performed by shifting the stress relaxation modulus curve along the logarithmic time axis, and the TTS shift factors a_T were determined.

The uniaxial tests were also performed using the DMA tester in the strain rate mode. The thin film sample (10mm ×4mm ×0.11mm) was stretched using a constant strain rate of 5% /min at the room temperature of 28 ℃.

2.2.4 *Volume shrinkage*

The volume shrinkage of the cured polymer was determined by accurately measuring the density of the cured polymer at different curing states [27,118] by using the helium gas pyconmeter (AccuPyc II 1340 Series Pycnometers, Micromeritics Instrument Corporation, Norcross, GA, USA). The mass of a sample was first measured by an analytical balance. Then the sample was placed in a sample chamber with a $0.1cm^3$ insert gas. The volume of the sample was then measured by the gas pyconmeter. The density was calculated by using mass divided by volume.

2.2.5 *Tensile tests under the polymerization condition*

To investigate the coupling between polymerization and mechanical deformation, we also conducted tensile tests under the photopolymerization condition. By curing a sample in the glass slide cell under $5mW/cm^2$ UV light at room temperature 28^oC for 5s, we obtained a partially cured sample, which was then mounted to the tension clamp of a universal mechanical testing machine (Criterion® Series 40 Electromechanical Universal Test System, MTS Inc, Eden Prairie, MN USA) for mechanical testing. We stretched the sample at room temperature (28 ℃). The dimensions of the samples were 14mm×3.42mm×0.13mm. In order to eliminate the oxygen effects, which were pronounced in thin samples [88], both the sample and the clamps were placed inside a box, where the oxygen was purged by nitrogen. The sample was first stretched about 1.1% for estimating the initial curing state of the material; the UV light (intensity $5mW/cm^2$) was then turned on to activate the chemical reaction while the sample was stretched at a strain rate of 6%/min.

2.2.6 *Experimental results*

The FTIR testing results are shown in Figure 2.1(a). As discussed above, the peaks at 1735 cm^{-1} do not change over time. The decrease of the absorbance peak at 1620 cm^{-1} and 1635 cm^{-1} indicates the conversion of the C=C bonds. The DoC is calculated using Eq. (2-1) and the calculated results are shown in Figure 2.1(b). We can see that the reaction accelerates around 4s-5s, then slows down significantly at around 10s. The final conversion is 82.9% around the curing time of 100s. The inset in Figure 2.1(b) shows the increase of the DoC at around 4-5s, which clearly demonstrates the auto-acceleration effect discussed above.

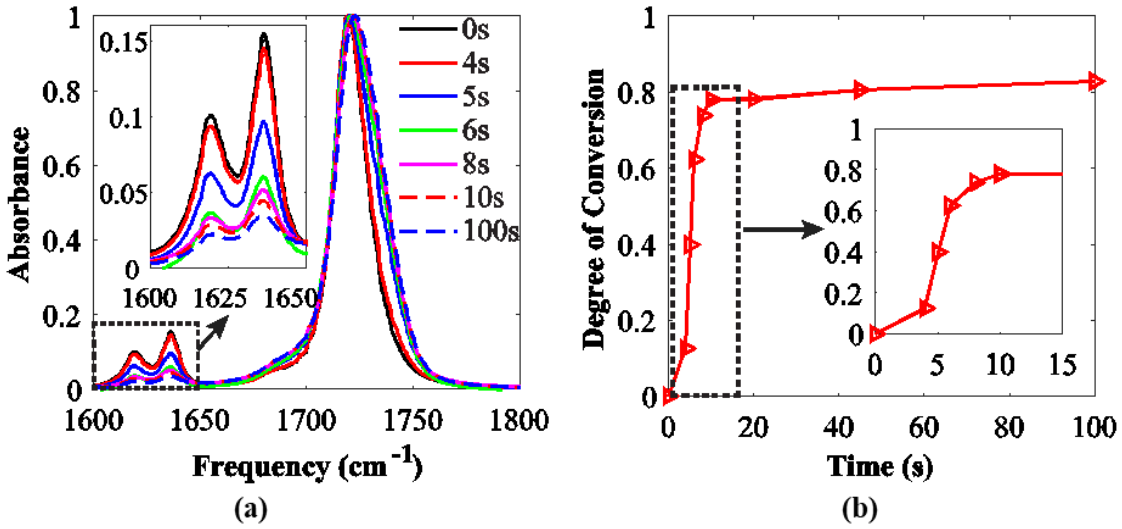

Figure 2.1 Measured degree of conversion of the cured polymer at different curing time. (a) FTIR absorbance spectra. (b) The degree of conversion as a function of time.

The results of the DMA tests are shown in Figure 2.2. Figure 2.2(a) shows the storage modulus of the cured polymer at different curing times. The storage modulus at high temperature increases as the curing time increases; this is due to the increase of the DoC or the crosslink density. The glass transition temperature (Figure 2.2(b)) also increases as the curing time increases. Figure 2.2(c) shows the variation of T_g as a function of the DoC.

Figure 2.2(d) shows the engineering stress-strain curves of the samples prepared using different curing times. We can see that the modulus of the cured material increases as the curing time increases, due to the increase of the crosslink density. In addition, for curing times longer than 8s, the cured polymers show obvious nonlinear viscoelastic stress-strain behaviors. As shown in Figure 2.2(b), T_g reaches about 37^{o}C at 8s, indicating that the cured polymers are in glassy state at room temperature, where glassy polymers typically demonstrate nonlinear viscoelastic deformations at intermediate to large strains.

Figure 2.2(e) shows the result of the uniaxial tension test of the sample under photopolymerization. We can see that before the UV light is turned on the material is a soft. After the UV light is turned on, the stiffness of the material increases rapidly at the beginning due to the fast increasing of the conversion.

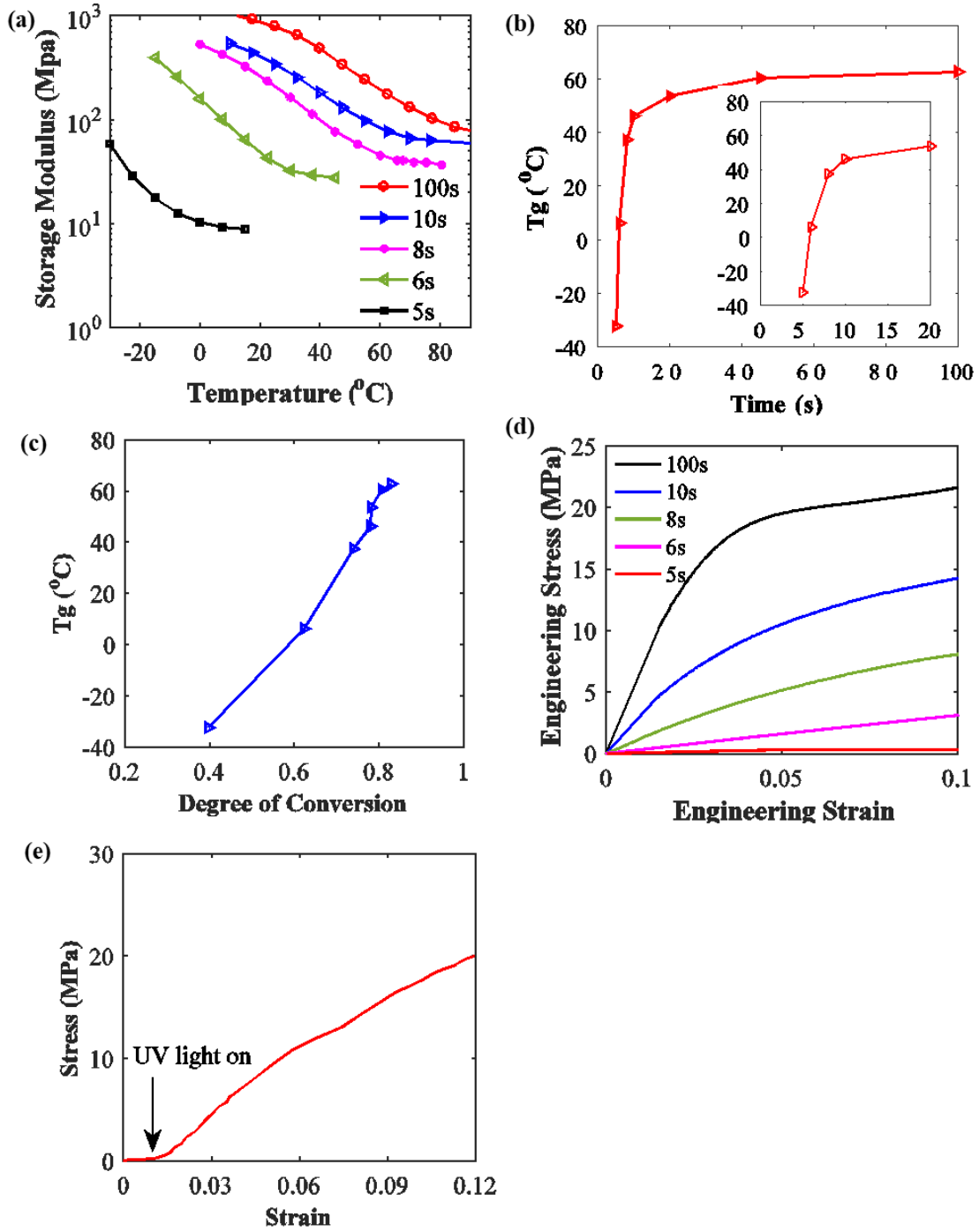

Figure 2.2 The DMA test results of polymer with different curing times. (a) Storage modulus for different samples. (b) Glass transition temperature as a function of the curing time. (c) Glass transition temperature as a function of the DoC. (d) Engineering stress-strain behaviors of the cured samples at different curing times. (e) The engineering stress-strain behavior of the sample under uniaxial tension test during photopolymerization.

2.3 Modeling Photopolymerization Kinetics

2.3.1 *Photopolymerization reaction mechanism*

A photopolymerization reaction typically has four steps: photodecomposition, initiation, propagation and termination [15,116,119,120].

$$\text{Photodecomposition: } P \xrightarrow{nh\nu} 2R^* \quad (2\text{-}2a)$$

$$\text{Initiation: } R^* + M \rightarrow RM^* \ (P^*) \quad (2\text{-}2b)$$

$$\text{Propagation: } R\text{-}M_n^* + M \rightarrow RM_{n+1}^* \text{ or } P^* + M \rightarrow P^* \quad (2\text{-}2c)$$

$$\text{Termination: } RMm^* + RMn^* \rightarrow RMm+nR / RMm+RMn \text{ or } P^* + P^* \rightarrow Pdead \quad (2\text{-}2d)$$

$$\text{Oxygen inhibition: } RM_m^* + O_2 \rightarrow RM_mOO \quad (2\text{-}2e)$$

First, light attacks photoinitiator molecules, which consequently decompose into radicals R* (* represents that the species has an active site) (Eq. (2-2a)). Usually one photo-initiator decomposes into two effective radicals. The effective radicals then attack the monomers M and activate the functional groups in the monomers (Eq. (2-2b)). When the monomers become active RM*, they can react with other monomers. Then polymer chains begin to propagate or crosslink with other polymer chains (Eq. (2-2c)). An active site does not vanish until it is terminated; therefore the polymer chain can also be in active state (P*). We can simply write it as P*+M→P*. The termination occurs when two radicals react with each other and become dead polymers P_{dead} (Eq. (2-2d)). The termination reaction occurs in two mechanisms: combination or disproportionation. By combination, two radical chains can form one dead polymer chain $RM_{m+n}R$ (Eq. (2-2d)),

while by disproportionation two dead polymer chains are produced RM_m+RM_n (Eq. (2-2d)). These two mechanisms can be simply written as $P^*+ P^* \rightarrow P_{dead}$. Oxygen in the environment can also inhibit polymerization reaction by combining with radicals and plays an important role in many photopolymer systems [88]. The inhibit mechanism can be described by Eq. (2-2e).

2.3.2 *Photopolymerization kinetics*

The photopolymerization reaction can be modeled using a set of first order reaction equations. Light penetrates the solution from the top surface to the bottom and is absorbed by photoinitiators, photoabsorbs and other light reactive species in the matrix. In this process, the light intensity is attenuated. The variation of the light intensity depends on the concentration of the absorbing species and the molar absorptivity. The light intensity variation with changes in the spatial position in the sample can be described by the Beer-Lambert law in Eq. (2-3a) [86,93,116,121,122]:

$$\mathbf{\Omega}(\mathbf{x},t) \bullet \nabla I(\mathbf{x},t) = -A(\mathbf{x},t) I(\mathbf{x},t) \tag{2-3a}$$

where $I(\mathbf{x},t)$ is the light intensity at position $\mathbf{x}$ and time t, $\mathbf{\Omega}(\mathbf{x},t)$ is the direction of light propagation and $A(\mathbf{x},t)$ is the local depletion rate of light intensity due to the absorbance of the species. From the above discussion, $A(\mathbf{x},t)$ can be calculated as:

$$A(\mathbf{x},t) = \alpha C_I(\mathbf{x},t) + A_{\text{absorber}}(\mathbf{x},t) + [A_{polymer}\, p(\mathbf{x},t) + A_{\text{monomer}}(\mathbf{x},t)(1-p(\mathbf{x},t))] \tag{2-3b}$$

where α is initiator molar absorptivity, C_I is the initiator concentration, $A_{\text{absorber}}(\mathbf{x},t)$, $A_{polymer}$, A_{monomer} are the absorption from photoabsorbers, converted polymer and unreacted

monomers respectively, and $p(\mathbf{x},t)$ is the DoC. During curing, the C=C bond is converted to a C-C bond, which changes the molar absorptivity of the curing material. Therefore the last two terms in Eq. (2-3b) are added to describe this change [123]. In this paper, we did not consider the effect of light refraction; this is because for photo-curing systems (including 3D printing), light is irradiated in (or close to) the perpendicular direction. For general cases, light may not be perpendicular to the solution surface, the propagation angle may change due to the difference of the refractive index, then the light propagation direction vector should be changed according to the refraction principal.

In this paper, light was irradiated above the curing cell for all the experiments and one dimensional version of Eq. (2-3a) can be written as Eq. (2-3c) to solve the light distribution in the thickness direction,

$$\frac{\partial \mathrm{I}(z,t)}{\partial \mathrm{z}} = -A(z,t)\mathrm{C}_I(z,t)I(z,t) \tag{2-3c}$$

where z is the coordinate of the material point in the thickness direction or the light direction.

After absorbing the energy from light photons, the initiators decompose into active species. The evolution of the initiator concentration is generally modeled by the first order chemical reaction differential equations [15,30,41,88,93].

$$\frac{\partial C_I(\mathbf{x},t)}{\partial t} = -\beta I(\mathbf{x},t)C_I(\mathbf{x},t) \tag{2-4}$$

where β is the photodecomposition rate. Likewise the concentrations of radicals and oxygens can be calculated as

$$\frac{\partial C_R(\mathbf{x},t)}{\partial t} = m\beta C_I(\mathbf{x},t)I(\mathbf{x},t) - 2k_{Term}(C_R(\mathbf{x},t))^2 - k_O C_R(\mathbf{x},t)C_O(\mathbf{x},t) \tag{2-5}$$

$$\frac{\partial C_{\mathrm{O}}(\mathbf{x},t)}{\partial t} = -k_{\mathrm{O}} C_{\mathrm{O}}(\mathbf{x},t)C_R(\mathbf{x},t) \tag{2-6}$$

where k_{Term} is the termination rate, C_O and C_{R} are the concentrations of oxygen and the concentrations of radicals, respectively, and k_{O} is the reaction rate between oxygen and radicals. The first term on the right side of Eq. (2-5) comes from the photodecomposition, which is proportional to the first term in Eq. (2-4). The proportion coefficient *m* is the number of radicals generated in photodecomposition, which depends on the type of photoinitiator; in our system, m=2. As described above, when two active radicals encounter each other, they can combine to form a dead polymer, and the two radicals terminate, which will reduce the concentration of active radicals. This is described by the second term in Eq. (2-5). In real reactions, the monomolecular termination also exists, and the termination mechanism can be very complicated. Here, we only considered the termination mechanism by two radical combinations; other mechanisms can be included in the model if necessary. To include the effect of oxygen, the last term is added in Eq. (2-5). The evolution of oxygen concentration is described by Eq. (2-6).

The monomers in the solution are gradually consumed by combining with radicals. In this process the reactive functional groups, such as C=C double bonds, are reduced and the monomers connect to the polymer primary chains. The concentration of the unconverted functional groups (C=C double bonds) can be calculated as:

$$\frac{\partial C_{\mathrm{M}}(\mathbf{y},t)}{\partial t} = -k_p C_M C_R \tag{2-7}$$

where C_M is the concentration of unconverted double bonds, and k_p is the propagation rate. The DoC of the double bonds can then be calculated as:

$$p(\mathbf{x},t) = 1 - \frac{C_M(\mathbf{x},t)}{C_M(\mathbf{x},t=0)} \tag{2-8}$$

In the above equations, the concentrations are defined in the initial configuration. Although the volume shrinkage during the chemical reaction can increase the concentrations of different species, the effect of the volume concentrations largely cancels in Eqs. (2-4)-(2-6) (except the higher order terms in these equations). We found that the volume shrinkage does not affect DoC noticeably (see Figure 2.18 in Supplementary Information).

Generally speaking, the propagation rate k_p in Eq. (2-7) and the termination rate k_{Term} in Eq. (2-5) are not constant and contribute to the auto acceleration where the chemical reaction changes sharply due to increasing viscosity [98,124]. As discussed above, auto-acceleration is closely related to the free radical termination rate, which is affected by the diffusion of radicals [98]. The diffusion controlled termination reaction starts at a very early stage of the polymerization reaction. Any factors that can influence the diffusion can affect the termination rate. The termination rate varies with conversion of monomers due to two dominant mechanisms: termination due to species translational diffusion of radicals ($k_{t,D}$) and termination due to reaction diffusion ($k_{t,RD}$). These two mechanisms occur in parallel; therefore the termination rate can be calculated as [124],

$$k_{Term} = k_{t,D} + k_{t,RD} \tag{2-9}$$

The species translational diffusion contribution $k_{t,D}$ is a combination of center-of-mass translational diffusion ($k_{t,TD}$) and segmental diffusion $k_{t,SD}$. $k_{t,TD}$ describes diffusion of the radicals' center of mass, which depends on the viscosity of the solution. As the reaction proceeds, the viscosity of the solution increases, leading to a decrease in the center of mass translational diffusion. Therefore $k_{t,TD}$ is inversely proportional to the relative viscosity e^{cp}, where c is a relative viscosity coefficient and p is the DoC [125]. In order to react with each other, not only should the radicals be close enough to meet, but the reactive functional groups must be reoriented in order to encounter by segmental diffusion $k_{t,SD}$, which is often treated as a constant. The center of mass translational diffusion and segmental diffusion occur consecutively (species need to be close to each other first, then orient into proper position); the species diffusion constant can thus be calculated as

$$\frac{1}{k_{t,D}} = \frac{1}{k_{t,SD}} + \frac{1}{k_{t,TD}} = \frac{1}{k_{t,SD}} + \frac{e^{cp}}{k_{t,TD0}} \tag{2-10}$$

where $k_{t,TD0}$ is the rate at zero conversion.

In addition to species translational diffusion, the reaction diffusion ($k_{t,RD}$) is another critical termination mechanism. The radical end also moves when the polymer chain growth due to the propagation reaction other than the diffusion process. Therefore the reaction diffusion rate is modeled to be proportional to the propagation rate k_p and the Doc,

$$k_{t,RD} = C_{RD} k_p (1 - p) \tag{2-11}$$

where C_{RD} is the reaction diffusion proportion parameter.

The polymerization rate k_p decreases in the high conversion, which can be modeled as [91,92,126]:

$$k_p = \frac{k_{p0}}{1 + \frac{k_{p0}}{k_{p,D0}} e^{cp}} \tag{2-12}$$

where k_{p0} is the polymerization rate at p=0, $k_{p,D0}$ is a parameter used to characterize the diffusion controlled propagation reaction.

Combining Eqs. (2-9)-(2-12), we obtain the total termination rate k_{Term}:

$$k_{Term} = \frac{1}{1/k_{t,SD} + \exp(cp)/k_{t,TD0}} + \frac{C_{RD}(1-p)k_{p0}}{1 + \frac{k_{p0}}{k_{p,D0}} \exp(cp)} \tag{2-13}$$

2.4 Modeling Material Property Evolution during Curing

Here we are interested in the mechanical properties of the polymer at different curing stages. When the curing advances, the polymer chain length and crosslink density increase, and liquid monomers transform into a viscous solid. These change the properties of the curing polymer dramatically.

2.4.1 *The glass transition temperature (T_g).*

The glass transition temperature is an important indication of the extent of curing and of the viscous property. As curing proceeds, the small monomers grow into large molecules and link to each other. The entire system has a wide distribution of polymer

chains with different molecular weights. The macroscopic properties measured in the experiments are the average behaviors of these chains. As discussed above, to characterize the average properties of the whole system, the DoC is a suitable evaluation parameter.

The relationship between the T_g and the DoC has been widely investigated. Generally, it can be modeled by the empirical Dibenedetto equation [127,128]. But sometimes the Dibenedetto equation cannot capture the dramatic T_g change at high DoC. Gan et al. [129] developed a viscoelastic type model for the curing polymer, which considers the crosslink effects on the mobility of the curing system and can well capture the T_g evolution of a wide variety of curing systems. Here we employ this viscoelastic type model to consider the T_g change during the curing process:

$$T_g = \frac{E_r}{R\ln[g_1(1-p)^{\xi} + g_2]} \tag{2-14}$$

where E_r is the activation energy of transition from the glassy to the rubbery state, R is the gas constant, ξ is the parameter for accounting the effects of chain entanglement. g_1, g_2 are two material constants.

2.4.2 *Volume shrinkage*

Volume shrinkage is common in a polymerization process and is a critical property in 3D printing. A large volume shrinkage can cause distortion of the 3D printed parts and can affect the accuracy of the printed shape. The relationship between volume shrinkage and the degree of conversion was investigated in the past [23,27], and a linear relationship between the volume shrinkage and the degree of conversion was shown:

$$\Lambda = \frac{V_0 - V}{V_0} = \chi p \tag{2-15a}$$

where V and V_o are the volume of the cured polymer and original uncured solution, and χ is the material property that is related to the free volume of the system. For the convenience of experimental measurements, the volume V is changed to be expressed as the density ρ :

$$\Lambda = \frac{\rho - \rho_0}{\rho} = \chi p \tag{2-15b}$$

2.4.3 *Constitutive modeling*

2.4.3.1 Kinematics

The deformation of the polymerizing material can be described by the deformation gradient. If a material point described by position vector $\mathbf{X}$ in the initial configuration moves to position $\mathbf{x}(\mathbf{X},t)$ in the current configuration, the deformation gradient during this motion is $\mathbf{G} = \frac{\partial \mathbf{x}}{\partial \mathbf{X}}$. During the polymerization process the material will experience volume shrinkage. The deformation gradient can be decomposed into a shrinkage-induced deformation part and a mechanical part [130]:

$$\mathbf{G} = \mathbf{G}^M \mathbf{G}^s \tag{2-16a}$$

where $\mathbf{G}^s$ is the shrinkage-induced deformation gradient and $\mathbf{G}^M$ is the mechanical deformation gradient. The curing shrinkage is isotropic; therefore, the shrinkage deformation gradient can be calculated as [130]:

$$\mathbf{G}^s = \sqrt[3]{(1-\chi p)}\mathbf{I} \tag{2-16b}$$

For the convenience in this description, we set $\mathbf{F} \equiv \mathbf{G}^M$ as the mechanical deformation gradient.

2.4.3.2 Basic assumptions

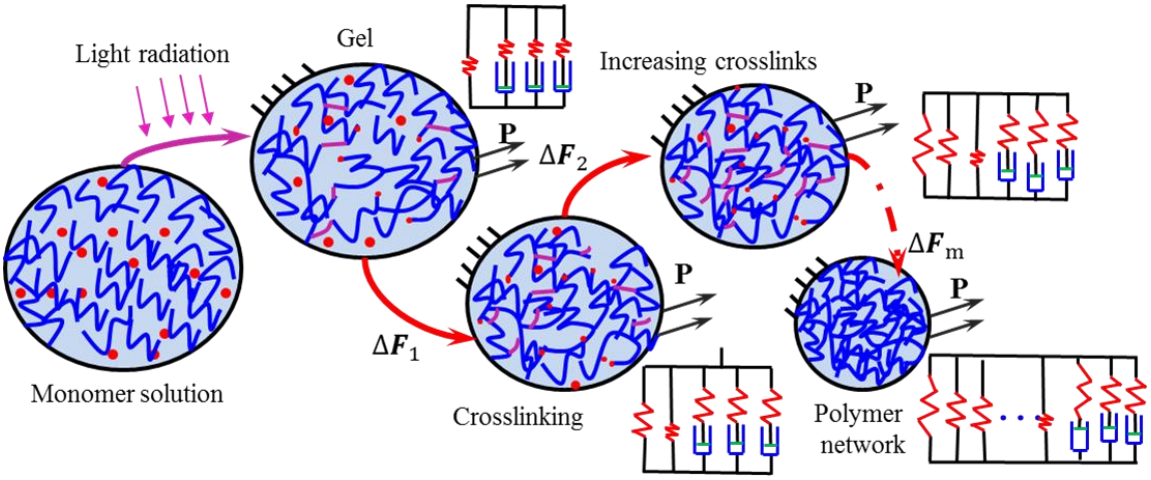

Figure 2.3 Diagram to show the phase evolution model.

As discussed before, photopolymerization is a complex process that couples material property evolution and mechanical deformation. To describe this coupling, we construct a model by using the incremental method. Figure 2.3 shows the concept of the mechanics during photopolymerization. Overall, we assume that the polymer system starts as a viscous melt in which the crosslinks are introduced; the viscosity of this melt changes as a function of temperature as well as the DoC. Specifically, we make the following assumptions:

1. Before the gel point, the material is in a liquid state, which can carry a short-term load due to viscosity but cannot carry any long-term load. Therefore, the material in liquid state is modeled as a viscous melt.

2. As polymerization proceeds, the polymer chains start to grow and crosslink, and soon the material passes the gel point. After the gel point, the crosslinks contribute to the equilibrium behaviors so that the material can carry the long-term load.
3. After the gel point, the increase of the crosslink density in the original polymer network results in a continuous increase in the material's stiffness, but the newly formed crosslinks are in a stress-free state and will not carry any current load when they are formed [102,131]. Therefore the newly formed crosslinks will not affect the current stress until the deformation state has changed.
4. The viscous (nonequilibrium) behaviors of the material can be described by the multibranch model, which consists of a series of Maxwell elements arranged in parallel. The total number of branches does not change, but the relaxation times in individual dashpots follow the principle of time-temperature-DoC superposition.

2.4.3.3 Mechanics during phase evolution

Figure 2.4 shows the one-dimensional rheological analogy for this model; it consists of two parts: the equilibrium branches and *N* non-equilibrium branches. The number of equilibrium branches increases as the number of crosslinks increases, and this can be described by the phase evolution model [109]. The non-equilibrium branches represent the stress relaxation mechanisms of the polymer. The newly added crosslinks will hinder the old crosslinks to relax in the rate of the old relaxation rate; therefore, the relaxation time will be shifted to the new relaxation time according to the time-temperature-DoC superposition. Following Figure 2.4, the total stress $\boldsymbol{\sigma}^{total}$ can be calculated by the summation of the stress in the equilibrium branches and in the non-equilibrium branches.

$$\boldsymbol{\sigma}^{total} = \boldsymbol{\sigma}_{eq} + \sum_{n=1}^{N} \boldsymbol{\sigma}_{neq,n} \tag{2-17}$$

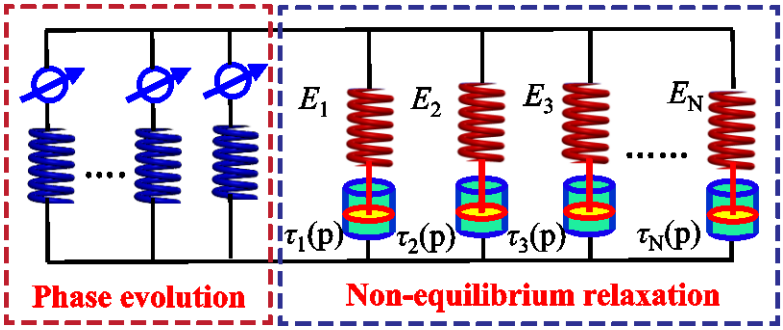

Figure 2.4 The one-dimensional rheological model for the viscoelastic mechanical properties modeling.

As the photopolymerization proceeds, the number of crosslinks increases with time. According to assumption 3, the newly formed crosslinks are in a stress-free state. In time increment *m*, the number of the newly formed crosslinks is ΔN_m during this time interval. We thus can define a crosslink fraction Δf_m as:

$$\Delta f_m = \frac{\Delta N_m}{N_M} \tag{2-18}$$

where N_M is the total crosslinks of the fully cured polymer. Here, we term these the crosslink fraction Δf_m as a new phase. It should be noted that the conceptual 'phase' in this model is different from the phase in the crystalline that has different crystal domains formed at different time steps.

The crosslinks formed in liquid state cannot bear the long-term load, there is no equilibrium branch before the gel point. At the gel point ($t=t_0$), the newly formed phase will deform immediately to satisfy the boundary conditions [109]. At $t=t_0$, the mechanical

deformation gradient is $\mathbf{F}_0$, which only acts on nonequilibrium branches. The stress can be calculated by the summation of the stress in the nonequilibrium branches.

$$\boldsymbol{\sigma}^{total}(t=t_0)=\boldsymbol{\sigma}_{neq}(\mathbf{F}_0) \tag{2-19}$$

At time increment Δt, a new phase with crosslink fraction $\Delta f_1=\frac{\Delta N_1}{N_c}$ forms. During this process, the mechanical deformation is increased by $\Delta\mathbf{F}_1$. The total stress is:

$$\boldsymbol{\sigma}^{total}(t=t_0+\Delta t)=f_0\boldsymbol{\sigma}_{eq}(\Delta\mathbf{F}_1)+\Delta f_1\boldsymbol{\sigma}_{eq}(\Delta\mathbf{F}_1)+\boldsymbol{\sigma}_{neq}(\Delta\mathbf{F}_1\mathbf{F}_0) \tag{2-20}$$

where f_0 is the total crosslink fraction before the gel point. At time t= $t_0+m\Delta t$, the m-th new phase forms. By assuming that all the existing phases undergo the same deformation gradient increment, we can express the deformation gradient in the phase formed at time t= $t_0+i\Delta t$ as:

$$\mathbf{F}_{i\to m}=\Delta\mathbf{F}_m...\Delta\mathbf{F}_{i+1}\Delta\mathbf{F}_i=\prod_{j=i}^{m}{}^{L}\Delta\mathbf{F}_j \tag{2-21}$$

where $\prod_{j=i}^{m}{}^{L}()$ means that the multiplicative operation sequence is toward the left. The total stress is:

$$\boldsymbol{\sigma}^{total}(t=t_0+m\Delta t)=\boldsymbol{\sigma}_{eq}^{total}+\boldsymbol{\sigma}_{neq}^{total}=f_0\boldsymbol{\sigma}_{eq,0}(\mathbf{F}_{1\to m})+\sum_{i=1}^{m}\Delta f_i\boldsymbol{\sigma}_{eq}(\mathbf{F}_{i\to m})+\boldsymbol{\sigma}_{neq}(\mathbf{F}_{1\to m}\mathbf{F}_0) \tag{2-22a}$$

Eq. (2-22a) can be written in the form of integration as

$$\boldsymbol{\sigma}^{total}(t)=f_0\boldsymbol{\sigma}_{eq,0}(\mathbf{F}\mathbf{F}_0^{-1})+\int_0^t\dot{f}\boldsymbol{\sigma}_{eq}(\mathbf{F}_t\mathbf{F}_s^{-1})ds+\boldsymbol{\sigma}_{neq}(\mathbf{F}) \tag{2-22b}$$

Computationally, to calculate the stress in each phase, we need to store the crosslink fraction and deformation gradient in each phase as internal variables, which will consume computer memory resources and CPU time quickly as the total time increases, making the model computationally very expensive. Therefore, an effective phase model (EPM) was developed by Long et al. [109] to address this problem. In this method, the stresses induced by the new phase are first calculated and then combined into the equivalent effective phase with an effective deformation. In such a way, we only need to record the effective phase fraction and effective deformation in each step. The details of this method can be found in references Long et al. [109] and Ge et al. [113]. Here we employed this EPM method to reduce the excessive requirements on computational resources.

In the EPM, we use one effective phase to represent the mechanical behavior of all phases. The effective phase has a combined effective crosslink fraction $\bar{f}$ and an effective deformation gradient $\bar{\mathbf{F}}_m$. At time t= $t_0 + m\Delta t$, the effective crosslink fraction is the summation of the crosslink fractions of all phases $\bar{f}_m = f_0 + \sum_{i=1}^{m} \Delta f_i$. The stresses of all equilibrium branches with phase evolution can be calculated as:

$$\boldsymbol{\sigma}_{eq,m}^{total} = \bar{f}_m \boldsymbol{\sigma}_{eq}(\bar{\mathbf{F}}_m) \tag{2-23}$$

After Δt time, the crosslink fraction increases and a new phase forms with crosslink fraction Δf_{m+1} while the material deforms $\Delta \mathbf{F}_{m+1}$. The total stress in the (m+1)-th increment is

$$\boldsymbol{\sigma}_{eq,m+1}^{total} = \bar{f}_m \boldsymbol{\sigma}_{eq}(\Delta \mathbf{F}_{m+1} \bar{\mathbf{F}}_m) + \Delta f_{m+1} \boldsymbol{\sigma}_{eq}(\Delta \mathbf{F}_{m+1}) \tag{2-24}$$

To combine all the phases into the effective phase at the current time, Eq. (2-23) needs to be updated:

$$\boldsymbol{\sigma}_{eq,m+1}^{total} = \bar{f}_{m+1}\boldsymbol{\sigma}_{eq}(\bar{\mathbf{F}}_{m+1}) = \bar{f}_{m+1}\boldsymbol{\sigma}_{eq}(\Delta\bar{\mathbf{F}}_{m+1}\bar{\mathbf{F}}_{m}) \tag{2-25}$$

Combining Eq. (2-24) and Eq. (2-25), we can relate the new phase to the effective phase:

$$\bar{f}_{m+1}\boldsymbol{\sigma}_{eq}(\Delta\bar{\mathbf{F}}_{m+1}\bar{\mathbf{F}}_{m}) = \bar{f}_{m}\boldsymbol{\sigma}_{eq}(\Delta\mathbf{F}_{m+1}\bar{\mathbf{F}}_{m}) + \Delta f_{m+1}\boldsymbol{\sigma}_{eq}(\Delta\mathbf{F}_{m+1}) \tag{2-26}$$

In this equation, $\bar{f}_{m+1}$, $\bar{f}_{m}$, Δf_{m+1}, $\Delta\mathbf{F}_{m+1}$, $\bar{\mathbf{F}}_{m}$ are all known and only the effective deformation increment $\Delta\bar{\mathbf{F}}_{m+1}$ is unknown. Applying the Newton–Raphson scheme, we can solve this equation. Then the new effective deformation $\bar{\mathbf{F}}_{m+1} = \Delta\bar{\mathbf{F}}_{m+1}\bar{\mathbf{F}}_{m}$ of the (m+1)-th increment can be calculated and recorded.

2.4.3.4 Evolution of crosslinks

The equilibrium modulus is directly related to the crosslink density by

$$E_{eq} = 3\mu_{eq} = 3Nk_bT \tag{2-27}$$

where μ_{eq} is the shear modulus, k_b is the Boltzmann constant, and T is the temperature.

Previous works [9,132,133] indicate that equilibrium modulus and the DoC follow the exponential relationship after the gel point:

$$E_{eq} = E_c \exp(b(p - p_{gel})) + E_d \tag{2-28}$$

where the E_c, E_d and b are fitting parameters. Therefore, the crosslinks' evolution after the gel point can be expressed using the exponential function,

$$N = \frac{1}{3k_bT}[E_c \exp(b(p - p_{gel})) + E_d] \tag{2-29}$$

Before the gel point, since the equilibrium branch does not exist, we can set it to be zero or to be a very small value for the convenience of numerical simulations.

At t=t_0+ mΔt, a newly formed phase is expressed as

$$\Delta N_m = \frac{dN}{dt}\Delta t = \frac{1}{3k_bT}[bE_c \exp(b(p - p_{gel}))\frac{dp}{dt}]\Delta t \tag{2-30a}$$

Then the crosslink fraction of this phase is $\Delta f_m = \frac{\Delta N_m}{N_M}$.

2.4.3.5 Mechanical behaviors of equilibrium branches

For the polymeric material, the equilibrium branch can be considered as a neo-Hookean material with the shear modulus of the completely crosslinked network as $\mu_M = N_M k_b T$.

The Cauchy stress of *m*-th phase can be calculated by:

$$\boldsymbol{\sigma}_{eq} = J^{-1}(\mu_M J_{eq}^{-2/3}\mathbf{B}_{eq}^{'} + \kappa_M \ln J_{eq}\mathbf{I}) \tag{2-31a}$$

$$\mathbf{B}_{eq}^{'} = \mathbf{B}_{eq} - \frac{tr(\mathbf{B}_{eq})}{3}\mathbf{I}, \quad \mathbf{B}_{eq} = \mathbf{F}_{eq}\mathbf{F}_{eq}^{T}, \quad J_{eq} = \det(\mathbf{F}_{eq}) \tag{2-31b}$$

where κ_M are the bulk modulus of the completely cross-linked polymer, $\mathbf{I}$ is the second order identity tensor, $\mathbf{B}_{eq}^{'}$ is the deviatoric part of the left Cauchy–Green deformation tensor, $\mathbf{F}_{eq}$ is the mechanical deformation gradient of *m*-th phase, and $\mathbf{F}_{eq}$ can be $\bar{\mathbf{F}}_m$, $\Delta\bar{\mathbf{F}}_{m+1}$, $\Delta\mathbf{F}_{m+1}$, $\Delta\mathbf{F}_{m+1}\bar{\mathbf{F}}_m$, $\bar{\mathbf{F}}_{m+1}$ or $\Delta\bar{\mathbf{F}}_{m+1}\bar{\mathbf{F}}_m$ in Eqs. (2-23)-(2-26).

2.4.3.6 The nonequilibrium behaviors

Nonlinear viscoelastic properties are the main mechanical characteristics of polymer materials. Here we assume the nonlinear viscoelastic behavior of the photocurable resin follows the time-temperature-DoC superposition. We start with a model that has multiple Maxwell branches (shown in Figure 2.4) [134-136]. We assume that we have *N* Maxwell element branches and that each branch experiences the same mechanical deformation gradient **F**. The total deformation gradient can be decomposed into an elastic part and a viscous part.

$$\mathbf{F} = \mathbf{F}_n^{\,e}\mathbf{F}_n^{\,v} \tag{2-32}$$

where $\mathbf{F}_n^{\,v}$ is the relaxed configuration obtained elastically unloaded by $\mathbf{F}_n^{\,e}$, the subscript *n* represents the n-th branch. The Cauchy stress can be calculated as:

$$\boldsymbol{\sigma}_{\text{neq,n}} = \frac{1}{\det(\mathbf{F}_n^e)}[\mathbf{L}_n^e : \mathbf{E}_n^e] \tag{2-33}$$

where $\mathbf{E}_n^e$ is the Hencky strains, $\mathbf{E}_n^e = \ln \mathbf{V}_n^e$, $\mathbf{V}_n^e$ is the left stretch tensor calculated from the polar decomposition $\mathbf{F}_n^e = \mathbf{V}_n^e\mathbf{R}_n^e$, and $\mathbf{L}_n^e$ is the fourth order isotropic elastic tensor and is defined as

$$\mathbf{L}_n^e = \kappa_n \mathbf{I}\otimes\mathbf{I} + 2\mu_n(\mathbf{I} - \frac{1}{3}\mathbf{I}\otimes\mathbf{I}) \tag{2-34}$$

where κ_n, μ_n are the bulk modulus and shear modulus of *n*-th branch.

The viscous velocity gradient on each branch can be calculated as:

$$\mathbf{l}_n^v = \mathbf{D}_n^v + \mathbf{W}_n^v = \dot{\mathbf{F}}_n^v(\mathbf{F}_n^v)^{-1} \tag{2-35}$$

where $\mathbf{D}_n^v$ is the viscous stretch rate and $\mathbf{W}_n^v$ is the spin rate. By assuming the spin rate to be zero, we have $\dot{\mathbf{F}}_n^v = \mathbf{D}_n^v \mathbf{F}_n^v$. The viscous stretch rate can be modeled as:

$$\mathbf{D}_n^v = \frac{\dot{\gamma}_n^v \boldsymbol{\sigma}_n'}{\sqrt{2}\bar{s}_n}, \quad \bar{s}_n = [\frac{1}{2}\boldsymbol{\sigma}_n' : \boldsymbol{\sigma}_n']^{1/2} \tag{2-36}$$

where $\bar{s}_n$ is the equivalent stress of the nth branch and $\boldsymbol{\sigma}_n'$ is the deviatoric part of the Cauchy stress in the nth branch. The viscous flow can be calculated as:

$$\dot{\gamma}_{\mathrm{n}}^v = \frac{\sqrt{2}\bar{s}_n}{2\mu_n \tau_n} \tag{2-37}$$

where τ_n is the relaxation time of n-th branch.

2.4.3.7 Temperature-conversion and stress dependent relaxation time

The relaxation time of each Maxwell element is a function of temperature and the DoC. Following the method used in Simon et al. (2000), the relaxation time of polymerized material at temperature T with the DoC p can be represented by:

$$\tau_n(p,T) = a(p,T)\tau_n\left(p_{ref}, T_{g,ref}\right) \tag{2-38}$$

where $a(p,T)$ is the temperature-DoC superposition shift factor, $\tau_n\left(p_{ref}, T_{g,ref}\right)$ is the relaxation time of the reference sample with the DoC p_{ref} at the reference temperature $T_{g,ref}$, which is T_g of the reference sample. Here we choose the polymer cured at 100s as the reference state.

The shift factors can be calculated as:

$$\log_{10} a(p,T) = \frac{C}{T - T_\infty} - \frac{C}{T_g(p) - T_\infty} \tag{2-39a}$$

where T is the temperature, $T_g(p)$ is the glass transition temperature of the cured polymer with the DoC p, $T_\infty = T_g(p) - C_2$, and C and C_2 are two fitting parameters. Finally, we have

$$\log_{10} a(p,T) = \frac{C}{T - T_g(p) + C_2} - \frac{C}{C_2} \tag{2-39b}$$

To capture the nonlinear viscoelastic behavior of the cured sample at low temperature (lower than its T_g), we consider that the relaxation time can be reduced significantly by the applied stress due to the activation energy change. Following the previous work [137], we have

$$\tau_n\left(p,T,\sigma\right) = a(p,T)\tau_n\left(p_{ref},T_{g,ref}\right)\exp\left(-\frac{\Delta G}{k_B T}\frac{\bar{s}_n}{S_n}\right) \tag{2-40}$$

where ΔG is the activation energy, S_n is the athermal shear strength, which describes the resistance of the material to the nonlinear viscoelastic shear deformation, and $\bar{s}_n$ is the equivalent stress of the n-th branch in Eq. (2-36).

It should be noted that for glassy polymers, viscoplasticity is used to describe the non-recoverable deformation observed under constant or near constant temperature. It can be modeled in two approaches. The first approach is based on the Boyce model [138] which assumes the plastic flow in the material caused by the activation of kinks in the polymer chains [139,140]. The second approach, which is used in this paper, assumes that the plastic response of polymers is caused by nonlinear viscoelasticity where the relaxation time does not only depend on temperature, but also dilatation, shape distortion, and shear

stress [141-143]. Taking the view of the second approach, the "plastic" deformation can be recovered if the temperature is increased to well above the glass transition temperature. At low temperature, the high shear stress can reduce the relaxation time significantly and causes the viscous flow. If the stress is removed, the relaxation time increases significantly again, and the material exhibits "plastic" deformation. When the temperature is increased to well above the glass transition temperature, the relaxation time is low again and the "plastic" deformation can be recovered. In fact, if the first approach can be modified by considering the dependency of relaxation on temperature, "plastic" deformation can also be recovered.

According to the Boyce et al[144], the athermal shear strength can be related to the shear modulus of the material as:

$$S_n = \frac{0.077\mu_n}{(1-\nu)} \tag{2-41}$$

The activation energy ΔG is constant at the low degree of conversion, but changes dramatically after the polymer network forms [145]. Here we model the ΔG using the empirical relationship:

$$\Delta G = \Delta G_0 + h\sinh(p / p_0) \tag{2-42}$$

where ΔG_0 is the activation energy of the material at low DoC and p_0 is the critical DoC for the activation energy, *h* is an empirical material constant.

2.5 Results and Discussion

2.5.1 *Material parameters characterization*

In this section, the material parameters used in the model are obtained by fitting different experimental results. Specifically, parameters associated with the reaction kinetics (or the DoC) are obtained by fitting FTIR measurements; parameters associated with the evolution of T_g are obtained by fitting the T_g results from DMA tests; the parameters for shift factors are determined by the stress relaxation tests; parameters in the multibranch model are determined by fitting the storage modulus and tan δ curves from the DMA tests; parameters in the stress-strain behavior are determined by the uniaxial tensile tests.

2.5.1.1 Reaction kinetics

The FTIR results are used to obtain parameters associated with the reaction kinetics. The details of the fitting method can be found in the Supplementary Information. The material constants used in the model are summarized in Table 2-1, and the fitted results are shown in Figure 2.5(a). It can be seen that the model captures the auto-acceleration effect where the DoC increases rapidly at curing degree around 12%. The polymerization rate decreases and tends to stop at around 15s, and the maximum DoC is 82.9%. The model results match the experimental conversion rate well. Figure 2.5(b) shows the propagation and termination reaction rates from the model as functions of the DoC. We can see that both the propagation and the termination rates decrease dramatically at high conversion. It is also seen that at the beginning of the reaction, the termination rate is much higher than the propagation rate, which is the reason why the polymerization is slow at the low conversion.

Table 2-1 Parameters used in the modeling of photopolymerization

Parameters for reaction kinetics (FTIR measurements; SI Section)					
α (m^2/mol)	45.83	$A_{monomer}$ (m^{-1})	0	$A_{polymer}$ (m^{-1})	1806.9
C_{O20} (mol/m^3)	1.05	β (s^2/kg)	8.999E-04	k_{p0} (m^3/mol/s)	1.86048
kp_{D0} (m^3/mol/s)	8.994E+08	k_{SD} (m^3/mol/s)	4.39E+03	c	34.149
k_{TD0} (m^3/mol/s)	10024.43	C_{RD}	1.0146	K_O (m^3/mol/s)	3499.9
Do (m^2/s)	0				
Parameters for T_g (T_g from DMA tests; Section 5.1.2)					
E_r (J/mol)	18959	g_1	109603	g_2	722.20	ξ	3.73
Parameters for volume shrinkage (Pyconmeter measurement; Section 2.5.1.3)					
			χ		0.24
Parameters for equilibrium branch (Uniaxial tension; Section 2.5.1.4)					
E_c (MPa)	1.059	E_d (MPa)	3.321	b	5.248
Parameters for nonequlibrium branches (DMA tests; Section 2.5.1.5 and SI Section)					
E_n (Mpa) n=1,2,..30	3.1897; 3.93254; 4.73212; 5.68973; 7.29328; 9.0777; 10.5624; 13.6055; 16.6365; 19.4448; 21.4905; 24.3312; 27.7104; 32.3655; 37.6868; 42.5355; 45.8291; 49.1156; 47.1021; 55.1153; 48.3834; 59.233; 59.1445; 52.6966; 57.5982; 57.0555; 59.6453; 64.19; 68.5159; 96.2441				
τ_n (s) n=1,2,..30	60724.1; 13591.8; 2806.48; 671.709; 165.818; 39.601; 10.182; 2.637; 0.6288; 0.1571; 0.04158; 0.01163; 0.003274; 9E-04; 2.314E-04; 5.64E-05;1.35E-05; 3.15E-06; 7.25E-07; 1.6E-07; 3.33E-08; 6.88E-09; 1.46E-09; 3.02E-10; 5.63E-11; 1.01E-11; 1.83E-12; 3.09E-13; 4.54E-14; 5.75E-15				
Shift factor	C(℃)	61000	C_2 (℃)		511.792
Parameters for nonlinear viscoelastic behavior (Uniaxial tension; Section 2.5.1.6)					
ΔG_0 (J)	0	h(J)	6.858E-25	p_0	0.0683

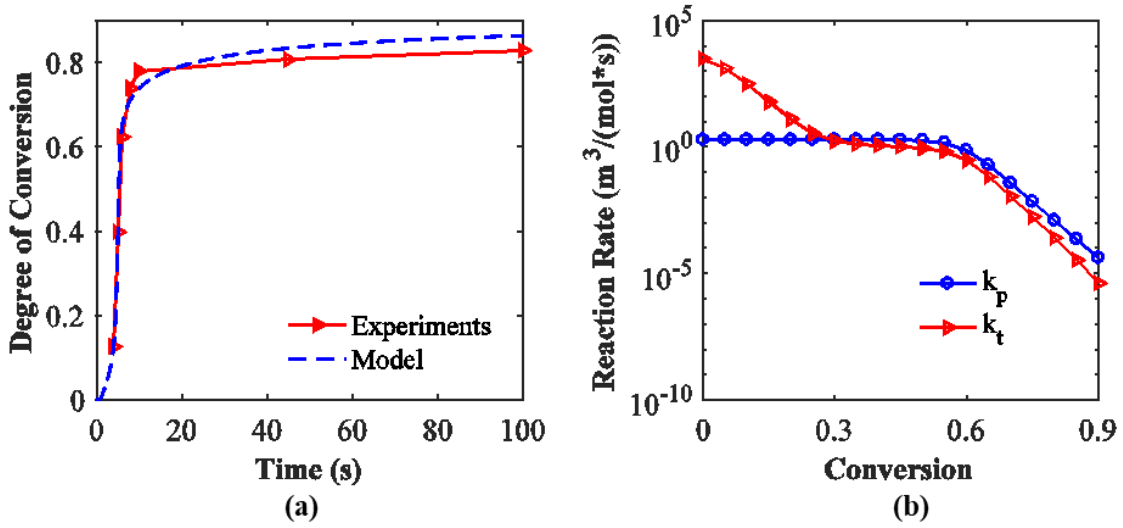

Figure 2.5 The chemical reaction process. (a) The FTIR results for measuring the degree of conversion. (b) The model simulations of the propagation and termination rate as functions of the degree of conversion.

2.5.1.2 Glass transition temperature

The DoC measurements, together with the DMA test results, were used to fit the T_g evolution in the curing process by applying Eq. (2-14). The fitting parameters are listed in Table 2-1. The T_gs of polymers with different curing times were measured using DMA tests. The T_g as a function of curing time and as a function of conversion are plotted in Figure 2.6(a) and 2.6(b), respectively.

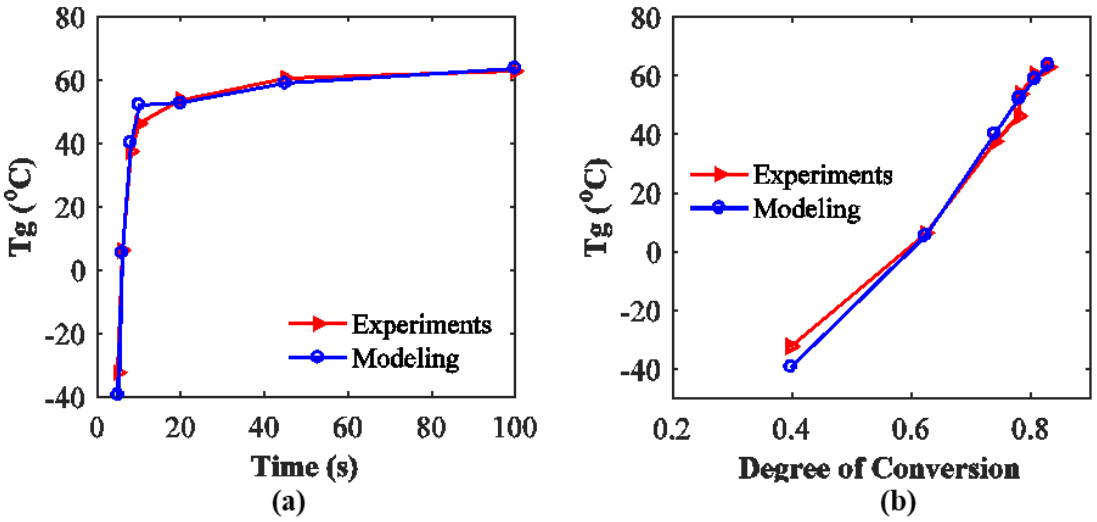

Figure 2.6 The T_g as the function of (a) time and (b) DoC.

2.5.1.3 The Volume shrinkage

The volume shrinkage is calculated by Eq. (2-15b). The relationship between the shrinkage and the DoC is fitted using a linear relation (Figure 2.7). The determined shrinkage constant χ is 0.24.

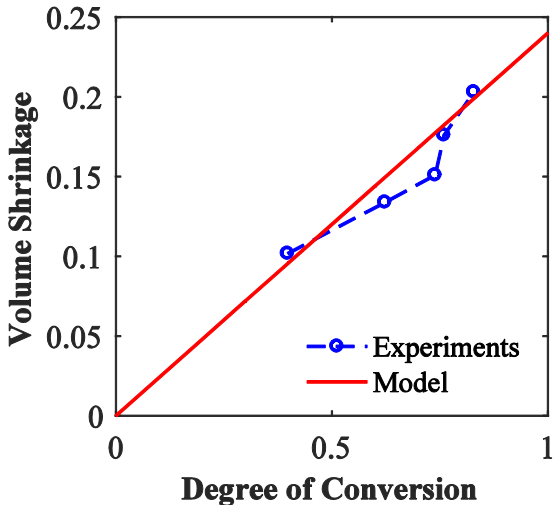

Figure 2.7 The relationship between volume shrinkage and degree of conversion.

2.5.1.4 Crosslink density evolution in the equilibrium branch

For samples at different curing states, the equilibrium modulus changes according to Eq. (2-28). Here, we use the plateau region of the storage modulus at high temperature (30 ℃ higher than the T_g) as the modulus of the equilibrium branch. The crosslink density can then be calculated using Eq. (2-29). The material parameters used in Eq. (2-29) are also listed in Table 2-1. The comparison between the experiments and the model are plotted in Figure 2.8. We can see that the model can capture the crosslink density change well.

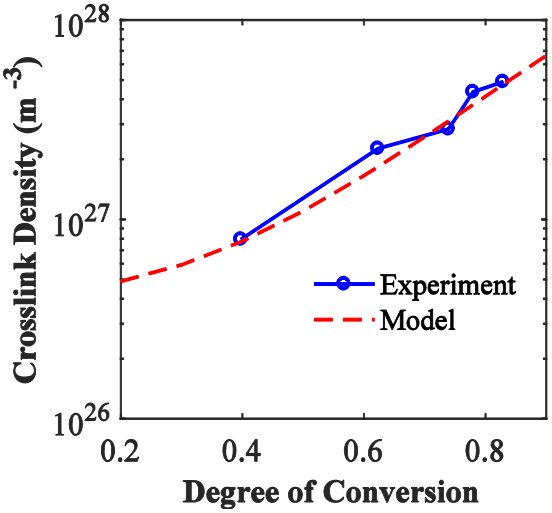

Figure 2.8 The crosslink density evolution as a function of the DoC.

2.5.1.5 The dynamic modulus and relaxation time

As discussed in the previous section, at any curing state our model has many equilibrium branches and *N* nonequlibrium branches. Determining the material parameters in these branches require the consideration of experimental details. In our experiments, the cured sample was removed from the curing cell and the material was left in a relaxed state for some time before testing. Therefore, there was no need to consider the deformation history in the equilibrium branches; all equilibrium branches could be considered as one spring that has the total modulus of all equilibrium branches or the equilibrium modulus of the sample. To characterize the modulus and relaxation time of the nonequlibrium branches, the stress relaxation and the DMA test results were used.

We used the fully cured sample (the sample cured with 100s) as the reference curing state to fit the shift factors, dynamic modulus and relaxation time; the viscoelastic properties of other curing states were calculated based on the time-temperature-DoC superposition in Eq. (2-38) and Eq. (2-39). Specifically, first, the shift factors of the fully

cured sample were determined by the stress relaxation tests, based on the time-temperature superposition principle (TTSP) [135]. The Tg of the sample was taken as the reference temperature to calculate the shift factor. The details of the calculating procedure are provided in the SI. The shift factors are plotted as a function of temperature in Figure 2.9(a), and the fitted curve is also shown. The fitting parameters C and C2 are listed in Table 1. Second, using the fitted shift factors, we fit the storage modulus E′ and the tan δ curves of the fully cured sample from the DMA tests to determine the moduli and relaxation times for the N nonequlibrium branches. The storage moduli and tan δ at different temperatures can be calculated using Eqs. (2-44a)-(2-44c). Employing the nonlinear regression (NLREG) method [146,147], the modulus and relaxation time of each branch were determined and are listed in Table 2-1. Figure 2.9(b) plots a comparison of the storage modulus and tan δ curves from the experiment and model fitting for the reference sample at different temperatures. To validate the quality of the fitted parameters, we used the determined parameters (moduli and the relaxation times at 100s) and Eq. (2-39b) to predict the temperature-DoC dependent relaxation times of the cured sample with different DoCs. Figure 2.10(a) compares the shift factors for the experimental and the modeling results. We can see that the time-temperature-DoC superposition can well describe the relaxation time variation during the photopolymerization process. With Eq. (2-39b) and Eq. (2-38), we can also predict the relaxation times of samples with different DoCs. According to Eq. (2-38), the relaxation times for the samples with different DoC are the result of shifts in the relaxation times of the fully cured samples; therefore, we can easily calculate them by multiplying the shift factor by the relaxation times of the fully cured sample. It is noted that the moduli of

nonequilibrium branches do not change as the DoC changes; by using the predicted relaxation times and the moduli of the nonequilibrium branches, we can predict the storage moduli of samples with different DoCs. The results are plotted and compared with the experimental results in Figure 2.10(b).

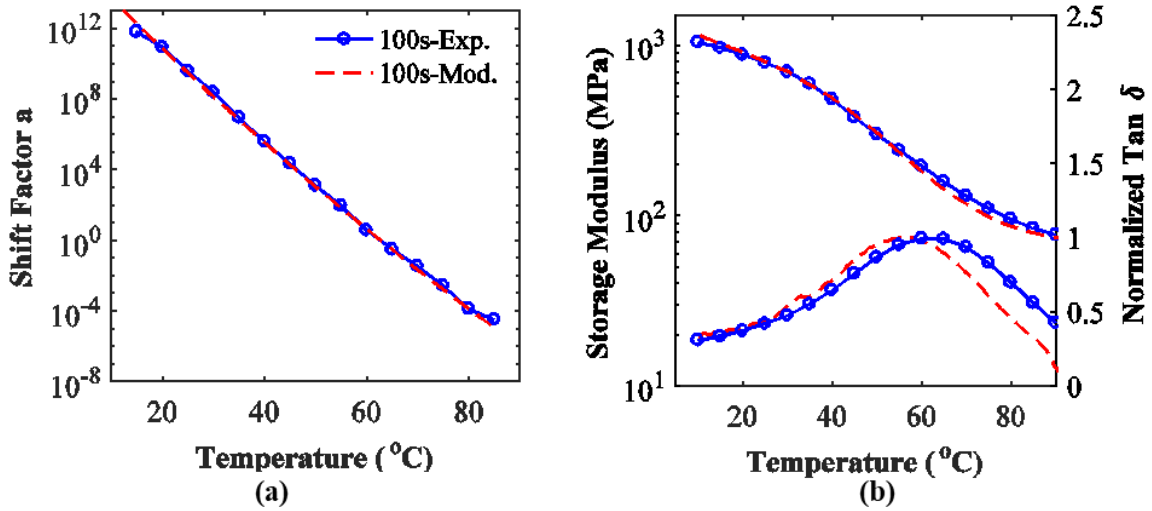

Figure 2.9 Viscoelastic properties of fully cured sample (t=100s). (a) Shift factors used in constructing the master curves, (b) the dynamic storage modulus and tan δ. Solid line: results from experiments, dashed line: results from model.

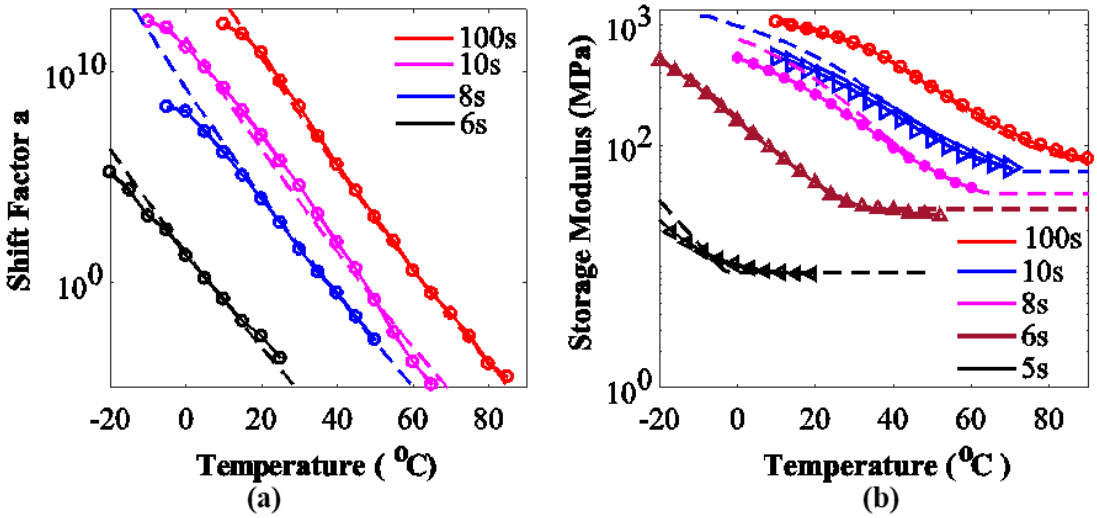

Figure 2.10 The viscoelastic properties of cured samples at different curing states. (a) The shift factors as a function of the temperature. (b) The storage Modulus. Solid line with symbols: results from experiments, dashed line: results from model.

2.5.1.6 Stress-strain behavior

The uniaxial tension tests were performed on samples at different curing states to characterize the material's mechanical behaviors. By using the previously determined moduli of the equilibrium and nonequlibrium branches and relaxation times, and combining the stress-dependent relaxation time method in Eq. (2-40), we can fit the activation energy parameters in Eq. (2-41) by using the experimental strain-stress curves at different curing times. Here we used the Poisson's ratio of ν=0.499 in Eq. (2-37). The fitting parameters used in the model are also summarized in Table 2-1. The fitted strain-stress curves of the cured samples at different curing states are compared with the experimental results in Figure 2.11. We can see that the material model can capture the stress-strain behaviors well.

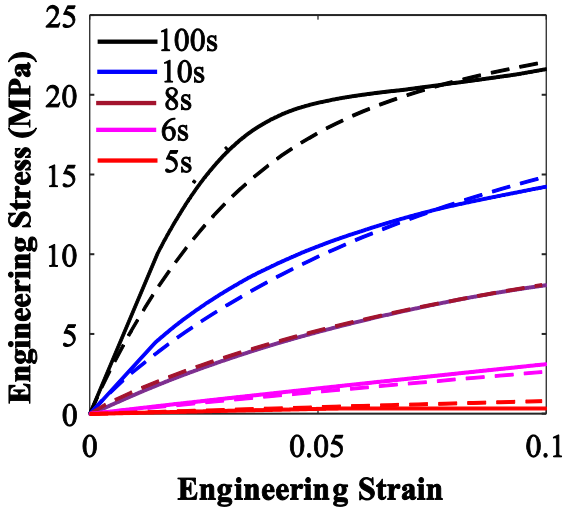

Figure 2.11 The uniaxial tension tests on samples at different curing times. Solid lines: results from the experiments, dashed lines: results from the model.

2.5.2 *Parametric Studies*

Using the above model and the identified parameters, we can predict the effects of different curing conditions on the photopolymerization process and material properties. Here we investigated the effects of light intensity and the photoinitiator concentration, and we compare the modeling results with selected experiments. All the parameters used here were the same as those determined in previous sections except the light intensity and the photoinitiator concentration. When studying the light intensity effects, we kept the photoinitiator concentration 0.3% constant; when studying the photoinitiator concentration effects, we kept the light intensity 5mW/cm^2 constant.

Figure 2.12(a) – 2.12(c) shows the effects of the light intensity on the DoC, the T_g evolution and crosslink density change. It is noted that the light intensity has little effect on the DoC, T_g, and crosslinking density if the light irradiation time is long. However, the light intensity has a strong effect on the curing speed. From Figure 2.12(a) we can see that at low light intensity, the chemical reaction is slow at the beginning, and the time for

the slow reaction period is much longer. At high light intensity the initial reaction is very fast, which means we can cure the liquid resin into a solid material very quickly. For example, at 2mW/cm^2, auto-acceleration occurs at ~7s; at 20mW/cm^2, auto-acceleration occurs ~2s. This can dramatically reduce the printing time in 3D printing. To validate the results, we did experiments for the case of light intensity of 10mW/cm^2, which is twice the light intensity of previous characterization tests. The experimental results are also plotted in Figure 2.12(a) – 2.12(c) using blue circles. We can see that the model can match the material properties' evolution. Figure 2.12(d) shows the modeling and experimental results for the stress-strain behavior of the cure sample using light intensity of 10mW/cm^2. The stress in the experiments is slightly higher than the modeling result. This might be because at the high light intensity, the material properties are very sensitive to the uncertainty (or variations) in light intensity because the conversion rate is very fast. Figure 2.12(d) shows the stress-strain behaviors for the samples cured for 10s with different light intensities. We can see that differences in the material properties of the samples with same curing time can be very dramatic if the light intensity is different.

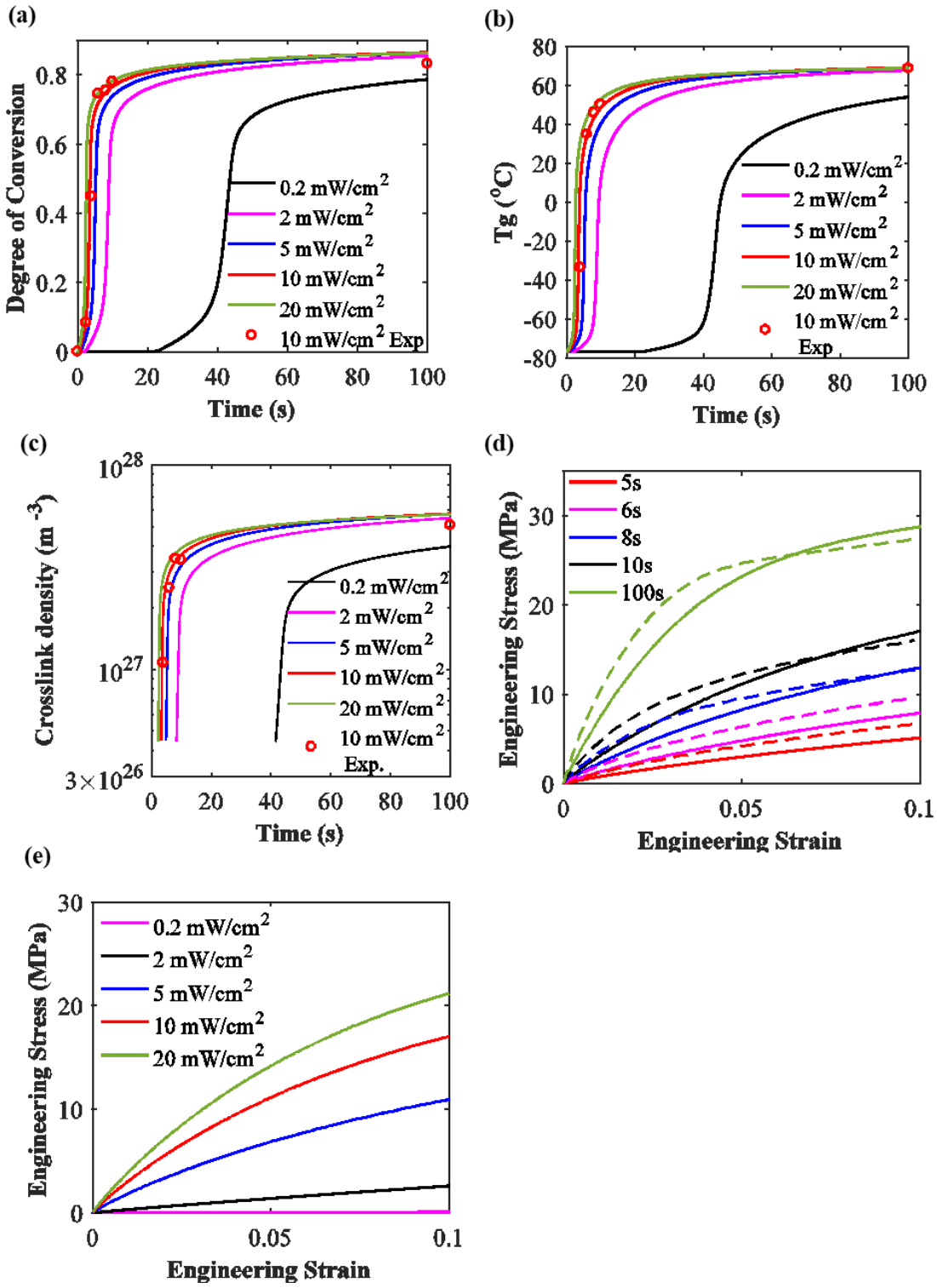

Figure 2.12 The effects of the light intensity on the polymerization process and the material properties evolution. (a) DoC, (b)T_g and (c) crosslink density evolution as the function of time at different light intensities. The blue circles are the experimental results. (d) Comparison of modeling and experimental results of the

stress-strain curves of the cured material at light intensity 10mW/cm^2. Dashed line: experimental results, solid line: model. (e) The modeling results of the stress-strain behavior of the sample cured for 10s at different light intensities.

Figure 2.13(a) – 2.13(c) shows the effects of the photoinitiator concentration on the DoC, the T_g evolution and crosslink density. Here, the light intensity is 5mW/cm^2. From Figure 2.13(a) we can see that at low photoinitiator concentration, the chemical reaction is also slow at the beginning, and the time before auto-acceleration is much longer. We also validate the modeling results by experiments for the case of photoinitiator concentration of 0.7%, which is commonly used in 3D printing. The experimental results are also plotted in Figure 2.13(a) – 2.13(c) using blue circles. We can see that the model can match the material properties' evolution. Figure 2.13(d) shows the stress-strain behaviors from modeling for the sample cured with 10s with different photoinitiator concentrations. Figure 2.13(e) compares the stress-strain behaviors from modeling and experiments for the sample with photoinitiator concentration of 0.7%. We can see that overall the model can capture the material property evolution at different concentrations of photoinitiators. Figure 2.13 also shows that one can use the photoinitiator concentration to control the reaction rate if the light intensity is limited by the equipment. We also note that there are small differences in the final DoC and T_g for different photoinitiator concentrations, even when the curing time is much longer than 100s. The reason is that at high values of DoC, the viscosity of the curing system is very high and the propagation of the reaction becomes slow. For the high photoinitiator concentration case, the reaction rate is higher, and large numbers of radicals can be generated at the beginning part of the reaction before the DoC is very high. Therefore, the propagation reaction can still proceed at a relatively high DoC.

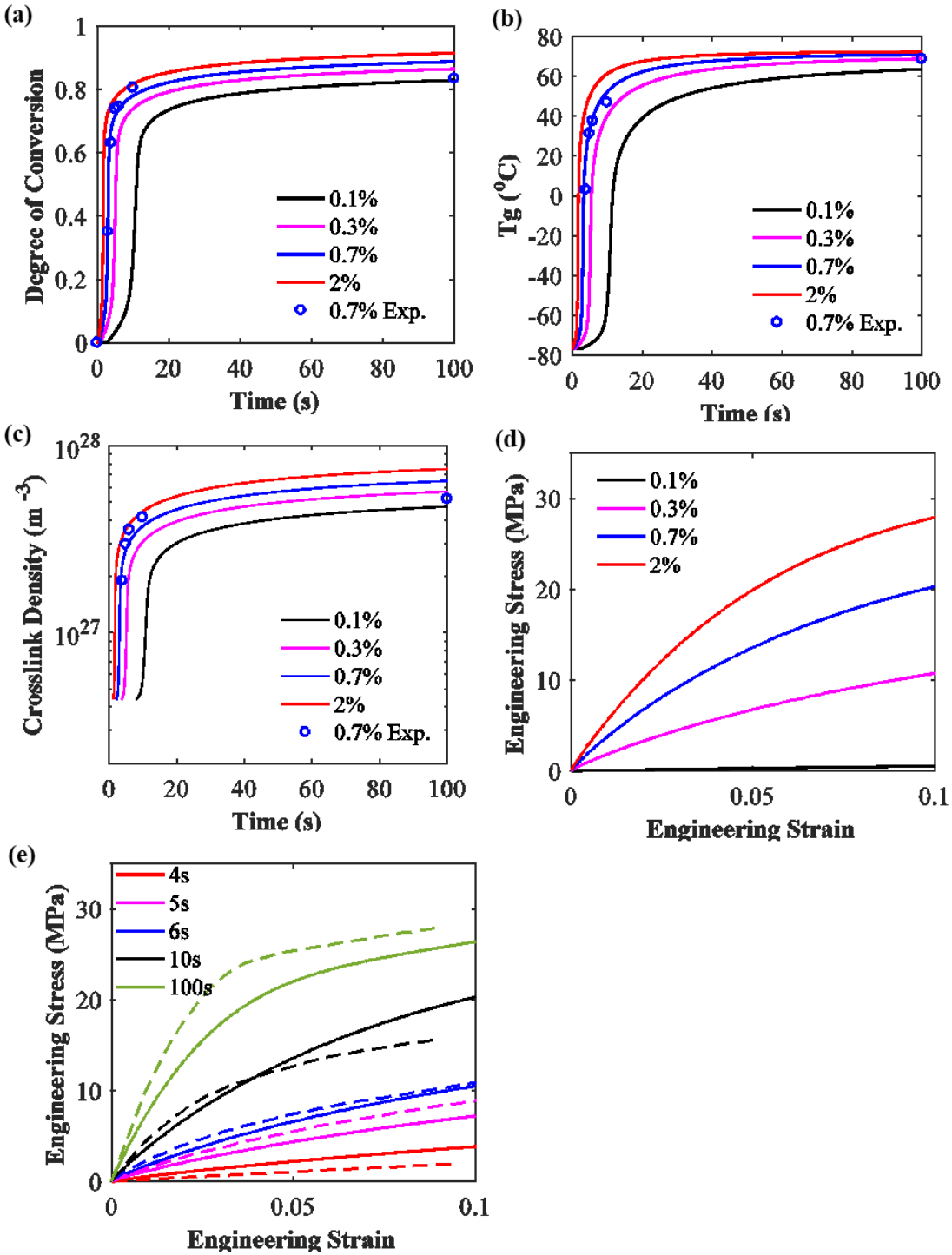

Figure 2.13 The effects of the photoinitiator concentration on the polymerization process and the material properties evolution. (a) DoC, (b)T_g and (c) crosslink density evolution as the function of time at different photoinitiator concentrations. The blue dots are the experimental results. (d) The stress-strain behaviors from modeling for the samples cured for 10s with different photoinitiator concentrations. (e) Comparison of modeling and experimental results of the stress-strain curves of

the cured material at photoinitiator concentration 0.7%. Dashed line: experimental results, solid line: modeling results.

2.5.3 *Application of the model*

2.5.3.1 The stress strain behavior of a curing sample under mechanical loading

As we discussed before, the formation of new crosslinks can couple with mechanical deformation. Although under most curing conditions, the mechanical deformation is mainly volume shrinkage, we consider a more dramatic coupling by stretching the sample while it is cured to evaluate our phase evolution model. To validate the model, we conducted an experiment for the strain stress behavior of the curing sample under uniaxial loading, as described in Section 2.5. The stress-strain behavior of the sample during this process is shown in Figure 2.14. The same process was also simulated by our model. During the curing process, the temperature increases about 10 ℃. Therefore, we set the temperature to be 10 ℃ higher than the room temperature (28℃). The result from model prediction is also shown in Figure 2.14. The stress-strain curve of the initial stretching of the pre-cured material is plotted with the blue line. As a comparison, the modeling result is also plotted. The red dashed line and the solid line show the experimental and modeling stress-strain curves of the sample under external stretching while being photocured. We can see that the modulus of the material increases rapidly in the beginning, due to fast conversion of the polymerization reaction. The model result is slightly higher than the experimental value, which may be because the shadow of the fixture on the ends of the sample hinders the reaction of the material at the sample ends. To show the material properties evolution, the strain-stress curve of the fully cured material is also plotted in Figure 2.14. We can see that at a relatively long time, the

material is fully cured and the final part of the stress-strain curve is mainly controlled by the material properties of the fully cured material.

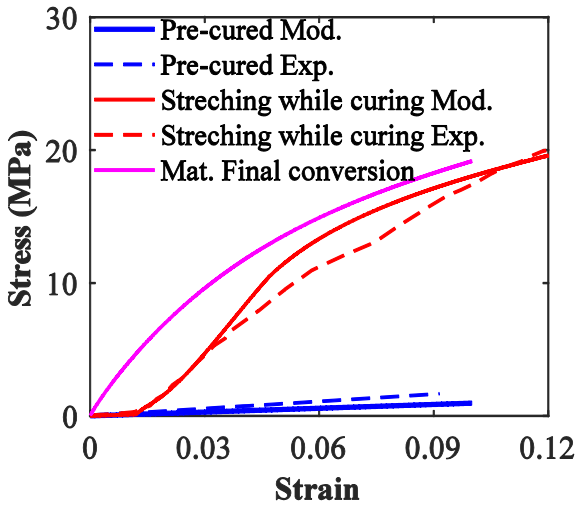

Figure 2.14 The stress-strain behavior of a curing sample under uniaxial tension loading.

2.5.3.2 The internal stress of thick sample during the photopolymerization

The internal stress caused by nonuniform DoC (due to, for example, nonuniform light) is a critical problem in the application of photopolymerization, such as 3D printing. Large internal stress can cause distortion of the polymerized structure, and even crash of the sample. On the other hand, the internal stress can be utilized to create self-folding structures. For example, Zhao, et al. [10] used the photopolymerization shrinkage internal stress caused by the nonuniform light field in the solution to fabricate 3D origami structures. Here, we show an example of how our model can be used to calculate the internal stress evolution during the photopolymerization process as well as the shape change after it is removed from the curing cell of a relatively thick sample.

The above constitutive model was implemented as a user material subroutine (UMAT) in the finite element analysis (FEA) software ABAQUS (Simulia, Providence, RI) and

was used in the simulation. For the FEA simulation of thick samples, a 50mm(L)x9.5mm(W)x0.6mm(T) sample was studied. Figure 2.20 shows the FEA model. Here, we consider the case where no photoabsorbers were added so that light was attenuated due to photoinitiators and the cured polymer. The FEA model of the DoC calculation started from t=0 (when light is on) but the shrinkage deformation started when the resin passes the gel point. Before the gel point, the shrinkage deformation did not play a role and a very small modulus was given to the material to make simulation stable. The chemical reaction was solved by writing a USDFLD user subroutine. Considering the symmetric boundary condition, only one-fourth of the model was used (see Figure 2.20). The three translational freedoms of the nodes on the top surface were fixed. On the symmetry surface, two nodes at the corner of the top surface were fixed, which would be used to fix the model after we released the boundary condition in the second step. The simulation consisted of two steps: during the first step, we simulated the curing process; in the second step, the sample was removed from the substrate, which was achieved by removing the boundary condition of the fixed top surface. The 20-node quadratic brick, reduced integration element C3D20R was used. Light with intensity of $5mW/cm^2$ was projected from the top of the surface. After curing for some time, the light was turned off and the sample was taken out of the curing cell (Step 2). We measured the bending curvature caused by the internal stress.

The DoC evolution during the curing process is shown in Figure 2.15(a). We can see that the difference in DoC at different height can be very large: the difference between top and bottom surfaces is around 39% for the sample cured for 6.1s. We also show the calculated internal stress evolution during the curing process in Figure 2.15(b). Due to

curing shrinkage, the internal stress could be very high, which is harmful for applications of photo curing to manufacturing, such as coatings. After releasing the boundary condition of the cured sample, the sample will bend due to internal stress as shown in Figure 2.16(a). The simulation results are compared with experimental results. As shown in Figure 2.16(a), the bending curvature of the sample is slightly higher than the simulation result. The possible reason is that the boundary of the top surface is fixed in the model, but in experiments the first cured materials adhere to the glass slide surface. In Figure 2.16(b), we show the internal stress of samples with curing times of 8s and 9s, respectively, before the samples were released.

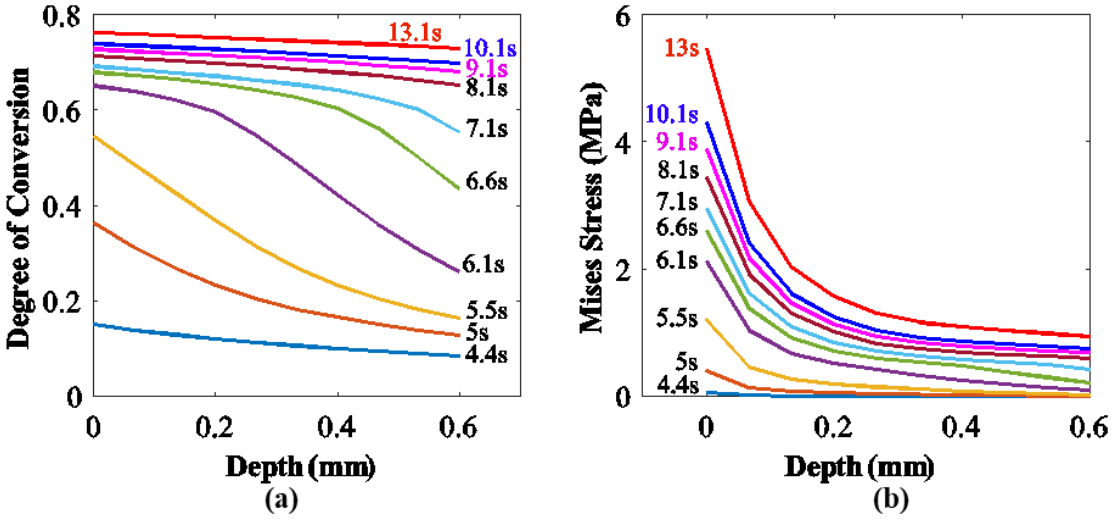

Figure 2.15 The DoC evolution (a) and the internal stress evolution (b) caused by the curing volume shrinkage of a thick sample during the curing process.

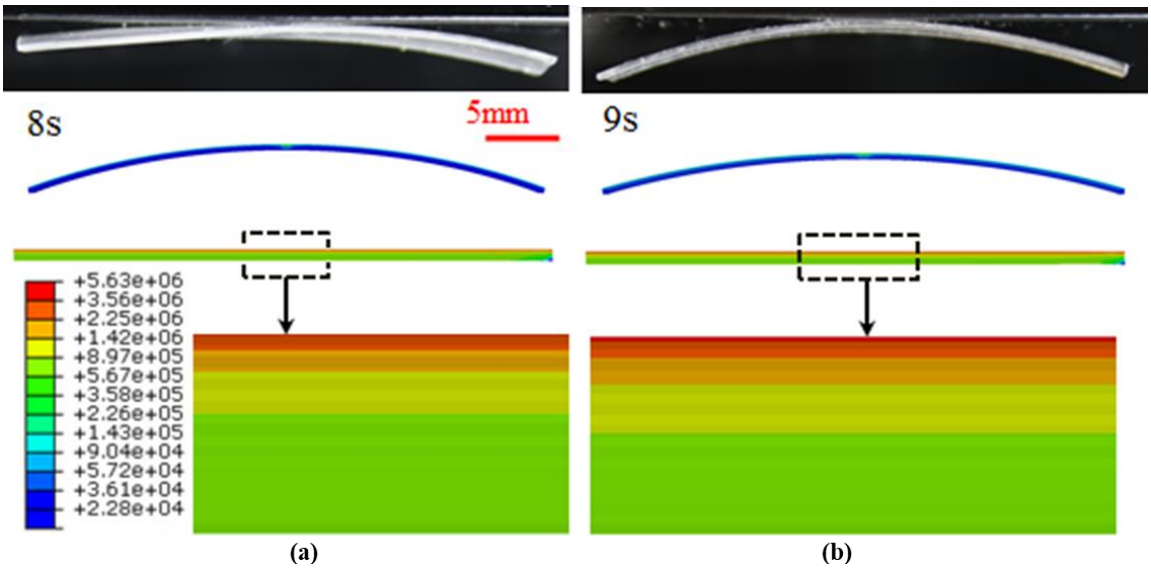

Figure 2.16 Bending curvatures of the cured thick samples with different curing times (light intensity 5mW/cm2, 0.3% photoinitiator) after taken out from the curing cell. (a) The experimental (top) and simulation (middle) results of the sample with curing times 8s. The bottom contour plot shows the distribution of Mises stress (Pa unit) before the sample is released. (b) The experimental (top) and simulation (middle) results of the bending curvature of the sample with curing time 9s. The bottom contour plot shows the distribution of Mises stress (Pa unit) before the sample is released.

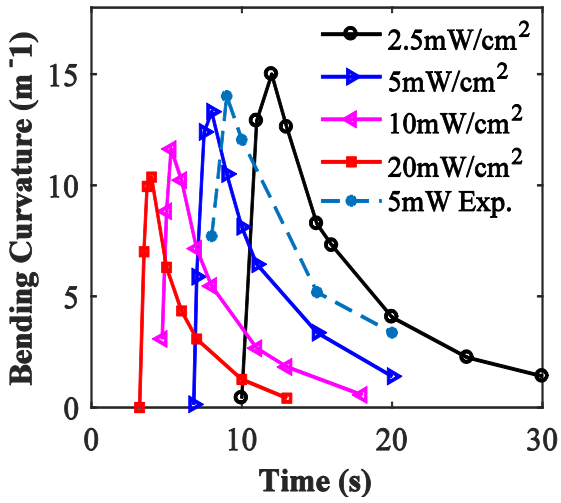

Figure 2.17 The bending curvature as a function of pre-curing time and light intensity.

Using this model, we studied the influence of curing time and light intensity on the bending curvature of the cured thick samples. The bending curvature of the samples as a function of pre-curing time and light intensity are shown in Figure 2.17. We can see that the bending curvature increases with curing time and then decreases; this is controlled by the gradient of the DoC and by the material stiffness. At the beginning, the differences of DoC at different heights is relatively large, but the volume shrinkage is relatively small, and the material stiffness with low DoC is very low. If the curing time is very long, the difference of the DoC in the material becomes very small which will also result in low bending curvature. Therefore we can obtain a maximum bending curvature at the intermediate curing time. The effects of the light intensity on the bending curvature are also plotted in Figure 2.17. The maximum bending curvature is not sensitive to changes in the light intensity. But the time to reach the maximum bending curvature decreases as the light intensity increases because of the much faster reaction rate. The experimental results for the curing time of $5mW/cm^2$ are also shown in Figure 2.17. The variance of the bending curvature and the maximum bending curvature in the experiments are nearly the same as the variance found in the simulation. The time required to reach the maximum bending curvature in the simulation is a little less than that on the experiments. The reason may be the different boundary conditions in the experiment and simulation as well as the temperature effects of the thick sample.

2.6 Conclusions

In this chapter, the evolution of mechanical properties in photopolymer during the photocuring process was investigated using theoretical modeling and experimentation. The chemical reaction kinetics was modeled using the first order reaction differential

equations. The polymerization propagation rate and the termination rate were described using the diffusion controlled model. To link the property changes with the chemical reaction, the degree of conversion of monomers was used as the internal variable to describe the curing system. The glass transition temperature and the volume shrinkage evolution were linked with the degree of conversion of monomers. A multi-branch model was used to capture the viscoelastic properties of the cured polymer at different curing times. To characterize the time-dependent deformation behavior of cured polymer under low temperature and finite deformation, nonlinear viscoelastic properties model was used. The polyethylene (glycol) diacrylate (PEGDA) monomer based curing system was used as the modeling material. Thin films of cured polymer at different curing states were made by controlling the radiation time. The degree of monomer conversion, volume shrinkage, glass transition temperature, dynamic mechanical properties and stress strain behavior were measured for different curing states. The theoretical model was applied to simulate the property variations during curing. The results indicated that the model could capture these properties' changes during curing. The parametric studies using the model indicated that light intensity did not affect the final degree of cure significantly, but a higher photoinitiator concentration could promote a higher final degree of cure. To demonstrate the application of this model, we studied the complex curing-mechanical loading coupling process. The incremental strain method combined with the material evolution model could describe the curing-mechanical loading coupling process properly. In addition, the internal stress of a thick sample caused by the volume shrinkage during photopolymerization was investigated. The variation of the internal stress in the thick sample during the photopolymerization was determined using the FEM simulation. The

model could be extended to model many industrial curing processes such as photopolymerization 3D printing, surface coating and automotive part curing process.

2.7 Supplementary Information

2.7.1 *Reaction kinetics*

In all of the experiments, the light shined above the curing cell, therefore the light intensity is only the function of the z coordinate and time and the one dimension model in Eq. (2-3c) was used. The curing cell is in cuboid shape (very thin in the thickness direction). The following boundary conditions and initial conditions are used:

At the top surface (z=0) of the liquid solution: $I(z=0,t) \equiv I_0$

The initial concentration (t=0): $C_{\mathrm{i}}(z,t=0) = C_{i0}$, $C_{\mathrm{R}}(z,t=0) = 0$, $C_{\mathrm{O}}(z,t=0) = C_{O0}$, $C_M(z,t=0) = C_{M0}$.

Since oxygen was kept out by the glass slides, the initial concentration of the oxygen inside the solution was chosen to be the equilibrium concentration [148], and the diffusion coefficient D_o was set to be 0. The molar absorptivity α was taken from a reference paper [149], and $A_{polymer}$ was measured experimentally. Since PEGDA monomers do not absorb light with wavelength of 365nm [150], the $A_{monomer}$ is set to be 0. Note that we used the molar absorptivity, not the molar distinction coefficient, and this can be converted by absorptivity $\alpha = 2.303 \times$(molar distinction coefficient).

Using the experimentally measured DoC data, we can fit the reaction kinetic parameters [125]. Here, we used the parameters in Buback's work [91] as the initial starting point and used the Matlab optimization functions 'patternsearch' and 'fmincon' to

minimize the standard deviation of the DoC between the modeling and experimental results. The fitted parameters are listed in Table 2-1 in the main text.

We also compared if volume shrinkage would affect the DoC. Figure 2.18(a)&(b) shows the evolution of the photoinitiator concentration and the radical concentration, which are higher when the volume shrinkage is considered. However, the DoC evolution for the two cases are almost identical as shown in Figure 2.18(c).

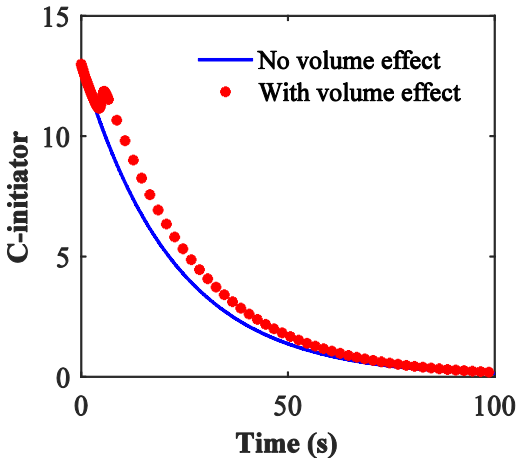

(a)

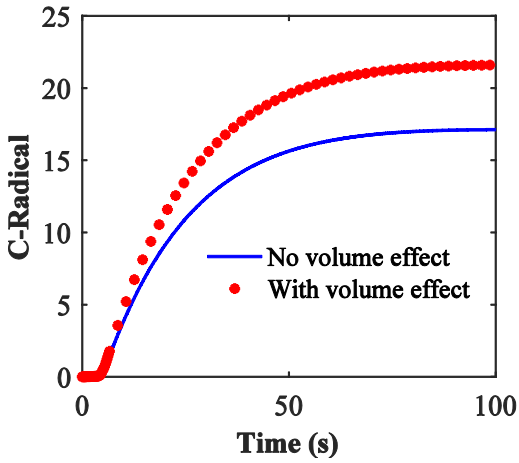

(b)

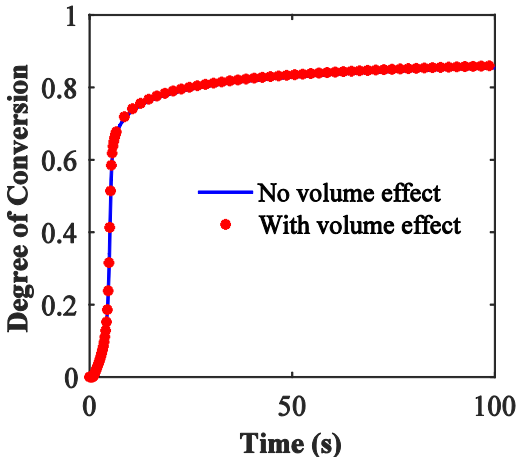

(c)

Figure 2.18 Effects of volume shrinkage to a) the photoinitiator concentration, b) the radical concentration, c) the DoC.

2.7.2 *The dynamic modulus and relaxation time of nonequilibrium branches*

2.7.2.1 The shift factors

The shift factor measurements and calculations were based on the TTSP. Stress relaxation tests of the material samples prepared with different curing times were performed with the temperature held around the T_g of the material. The stress relaxation behavior of the samples was measured with a temperature interval of 5^{o}C. Figure 2.19(a) shows the testing results of the reference sample (cured with 100s). The T_g of the sample was 62.7 ^{o}C. We first took the reference temperature to be 60 ^{o}C to calculate the shift factors. The relaxation curve of 60 ^{o}C was kept fixed and other curves with different temperatures were shifted horizontally along the time axis to construct the master curve. Figure 2.19(b) shows the constructed master curve of the reference sample. The shift factors were determined from the shifting time, and the results are shown in Figure 2.19(c). Note that the shift factors were calculated at the temperature of 60 ^{o}C, and we needed to shift this to the T_g of the sample (62.7 ^{o}C). We can easily calculate the shift factor at T_g by interpolation from the curve in Figure 2.19(c). And then the shift factors at T_g of the material can be calculated by using the shift factor curve at 60 ^{o}C and dividing by the shift factor value at temperature T_g. The calculated results are shown in Figure 2.19(d). Using the same procedure, the shift factors of samples with different curing times were measured and calculated. The results are shown in Figure 2.19(d).

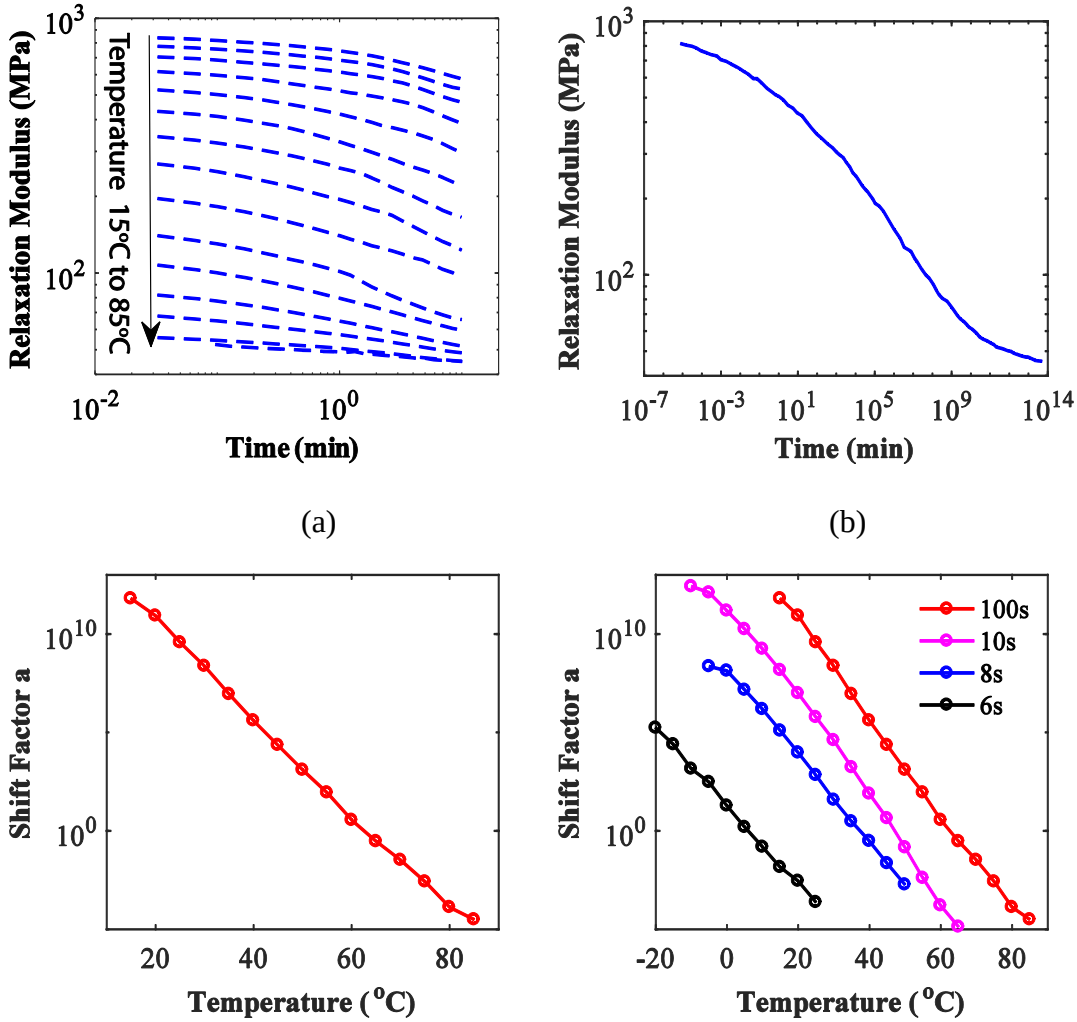

Figure 2.19 Stress relaxation behavior and shift factor measurements of the cured samples with different curing times. (a) The relaxation tests results of the reference sample. (b) The constructed master curve of reference sample. (c) The shift factors of the reference sample at reference temperature 60°C. (d) Shift factors of samples with different curing times. The reference temperature is taken to be the T_g of the sample.

2.7.2.2 The Storage modulus and tan δ

Using the 1D multi-branch model, the total stress of the system can be calculated as:

$$\sigma = E_{Eq}\varepsilon + \sum_{n=1}^{N} E_{non}^{n} \int_0^t \frac{\partial \varepsilon}{\partial s} \exp\left[-\int_s^t \frac{dt'}{\tau_n(T)} \right] ds \tag{2-43}$$

where E_{Eq} is the Young's modulus of the equilibrium branch, E_{non}^{n} and τ_n are the Young's modulus and temperature dependent relaxation time of the *n*th nonequilibrium branch. The dynamic mechanical properties such as storage modulus E_s, loss modulus E_l and tan δ of the cured polymer at different curing states can be modeled as [135]:

$$E_s(T) = E_{eq} + \sum_{n=1}^{N} E_n \frac{\omega^2 \left[a(p,T)\tau_n(T) \right]^2}{1 + \omega^2 \left[a(p,T)\tau_n(T) \right]^2} \tag{2-44a}$$

$$E_l(T) = \sum_{n=1}^{N} E_n \frac{\omega a(p,T)\tau_n(T)}{1 + \omega^2 \left[a(p,T)\tau_n(T) \right]^2} \tag{2-44b}$$

$$\tan\delta = \frac{E_s}{E_l} \tag{2-44c}$$

where $a(p,T)$ is the shift factor for the time-temperature superposition. Since we are modeling the curing process, the shift factors at different curing states are different. Therefore, the shift factor is also dependent on the DoC *p* as shown in Eq. (2-39). By fitting the DMA curves of the fully cured samples (here sample cured with100s), we can get the modulus and the relaxation time of each branch using the methods in [135]. Then we can calculate the viscoelastic properties of the material with different DoCs.

2.7.3 *Schematic diagram to show the model used in the FEM simulation*

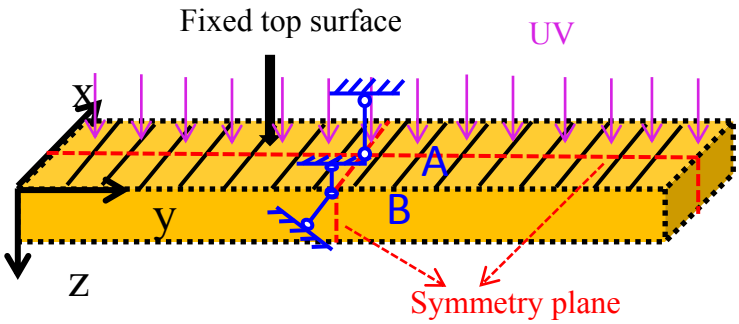

Figure 2.20 Schematic diagram of the model used in the FEM simulation in Sec. 2.5.3.2.

CHAPTER 3. FEM SIMULATION OF DIGITAL LIGHT PROCESSING 3D PRINTED STRUCTURES

3.1 Introduction

Additive manufacturing (AM) or three-dimensional (3D) printing technology which builds the 3D structure through the layer-by-layer material adding process has developed rapidly in recent years[42]. It has been widely applied to the aerospace engineering, automotive, civil engineering, electronics and biomedical devices [151-153]. Digital Light Processing (DLP) 3D Printing is one of the widely used 3D printing technology[14,40,48-53]. In the DLP printing, the digital light projector was used to flash the sliced layer image to the liquid resin surface and cure the liquid polymer resin into a solid material in the layer-by-layer manner. Due to the rapid photocuring reaction process, the DLP printing is a very efficient printing method. Since the material experience a rapid liquid to solid phase change during the photocuring process, its material property will change dramatically[115]. In addition, for many of the resin materials the volume shrinkage occurs during the photocuring process because of the chemical structure and interaction force change[21,22,30]. Large volume shrinkage can cause the development of the internal stress of the printed structure and the undesired deformation such as the curling and warpage of the printed parts[20,154,155]. Therefore, it is important to investigate the volume shrinkage induced distortion of the printed parts.

Usually, a typical DLP printing system includes three parts as shown in Figure 3.1(a): a light projector with high light intensity, a moving stage and the resin vat[14,40,48-53]. Before the 3D printing process begins, the geometry file of the printing part needs to be

sliced by the special software into pictures and will be exported to the projector. The liquid monomer resin for printing is contained in the resin vat. The digital light projector then flashes the sliced layer image to the liquid resin surface and cures the liquid polymer resin into a solid thin layer. Each layer is exposed to the light for a few seconds to dozens of seconds. Then the moving stage moves to the new layer position and a new layer of resin is cured by the projected light pattern. Through this layer-by-layer material adding process, a 3D structure can be printed. Here we will investigate this layer-by-layer DLP 3D printing process by experiments and theoretical simulations.

To build a theoretical model for layer-by-layer 3D printing process, we need to describe the material property evolution process, the volume shrinkage deformation and the mechanics during photocuring. Previously, Huang et al. built a theoretical model and applied the dynamic finite element method (FEM) to simulating the curl distortion of the stereolithography printing caused by the temperature change during laser scan[54]. In their method the modulus change and temperature induced volume change are related to the averaged energy dose and curing time by empiric equations. The laser scan curing was simulated by dynamic FEM. Xu et al. modeled the hardness of the curing material during the stereolithography printing as a linear function of the total light exposure[156]. Jiang et al. also used a phenomenal model to describe the elastic modulus as a function of the light exposure energy and exposure time[157]. In these methods, the material conversion process is usually simplified. In addition, the mechanics of volume change deformation of the photocuring material was not well investigated and even not mentioned. Previously we used the chemical reaction kinetics to investigate the material evolution process during photopolymerization, which includes the effect of auto acceleration on the

material conversion rate[115]. The material property evolution and volume shrinkage are modeled as the function of the degree of conversion (DoC). And we also build a finite deformation phase evolution model to describe the coupling of the material property evolution and volume shrinkage deformation and the stress development during photocuring. Here we will apply this model to investigate mechanics during the photocuring process of DLP 3D printing. In addition to describing the photocuring material conversion evolution, volume shrinkage deformation and photocuring mechanics, we also need to simulate the layer-by-layer material adding process. In the FEM simulation, the material adding process is the way how we add or activate the elements which will be photocured. The two typical methods of adding elements in the FEM simulation are the quiet element and inactive element method. In the inactive element method, the elements which are in uncured state will be deactivated first and reactivated when they will be added to the printing structure. The inactive element method has been widely used in simulations of the material adding process such as metal welding [158,159]. Wu et al. have utilized inactive element method to simulate the stress and crack development in the maskless photopolymerization additive manufacturing process using the commercial FEA software Abaqus[24]. In this research work, the inactive element method is utilized to simulate the layer-by-layer liquid resin element adding process.

In this chapter, the experimental and theoretical modeling methods to investigate the volume shrinkage induced distortion of the DLP printed polymer structures are provided. The chemical reaction kinetics was investigated by experiments and theoretical modeling. The material property evolution and chemical reaction induced volume shrinkage were related to the DoC of the material. A phase evolution constitutive model was developed

to describe the mechanics during photopolymerization. And the model has been applied to the FEM simulation to investigate the layer-by-layer DLP 3D printing process, the printing through error and distortion caused by the volume shrinkage.

3.2 The layer-by layer 3D printing process and simulation method

3.2.1 *The DLP 3D printing experiment method*

The materials of the resin consist of poly(ethylene glycol) diacrylate (PEGDA, Mn 250) oligomers, 0.45% photoinitiators (Irgacure 819), and 0.06% photoabsorbers (Sudan I). The structures used to print were designed by Solidworks software (Dassault Systèmes SOLIDWORKS Corp., Massachusetts, USA). Then the structure was exported as Stl file and imported to the slicer software Creation Workshop (DataTree3D, Dallas, Texas, USA). The grayscale value of the sliced picture of each layer can be changed by the Matlab code to control the light intensity of the light projector. The sliced picture was then projected onto the liquid resin by using the digital micromirror device (DMD) projector. The printing stage was controlled by a linear translation motor. After one layer was cured, the printing stage moved down to the next layer position. And the new layer-image was passed to the projector to cure the new layer. Through this layer-by-layer printing method, the whole structure can be printed. Thin samples with different printing parameters can be printed and then removed from the printing stage to measure the possible distortion. And then we can compare the results with FEM simulations.

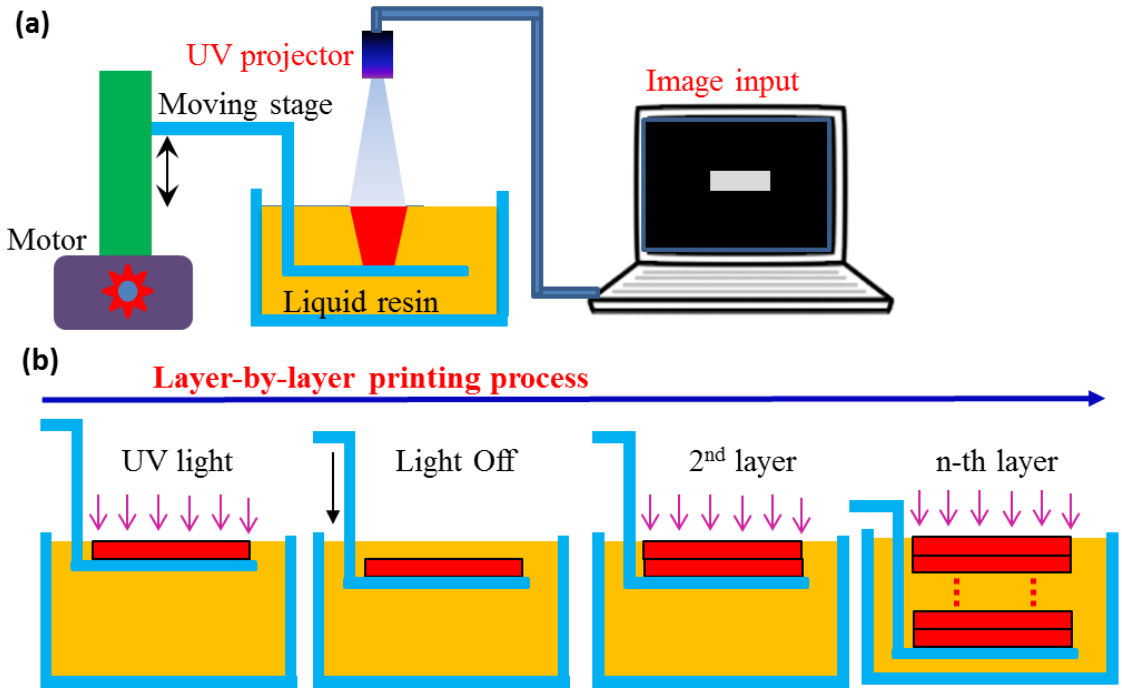

Figure 3.1 A schematic to show the DLP printing method. (a) The basic setup of the DLP 3D printer. (b) The layer-by –layer 3D printing process.

3.2.2 *The simulation method for layer-by-layer printing process*

The layer-by-layer 3D printing as shown in Figure 3.1 is a typical material addition process which has been widely investigated in the metal welding [160-163] or electron beam directed energy deposition simulations[164]. For the FEA simulation of the material addition process, an important problem is how to activate the elements which correspond to the newly added material. There are two basic methods which have been implemented, i.e. the quiet element and inactive element approach. In the quiet element method, the whole model structure is predefined and exists through all the simulation steps. And the elements which are not deposited are given a specific different material property so that they will not affect the already deposited model. For the inactive element approach, the elements are all deactivated in the beginning of the simulation and reactivated sequentially according to material adding process. The quiet element method is easy to

implement, but the artificial defined material property for the quiet element will cause the accumulation of the undesired stress. The inactive element method has been implemented to simulate the stress and crack development during large area maskless photopolymerization additive manufacturing process[24] using the commercial FEA software Abaqus. In this method the deactivation and the reactivation of the elements are achieved using the 'Model Change' option in Abaqus. Here in this paper, we will use the same element activation method. The implementation process of the simulation can be described by the flow chart and schematic shown in Figure 3.2.

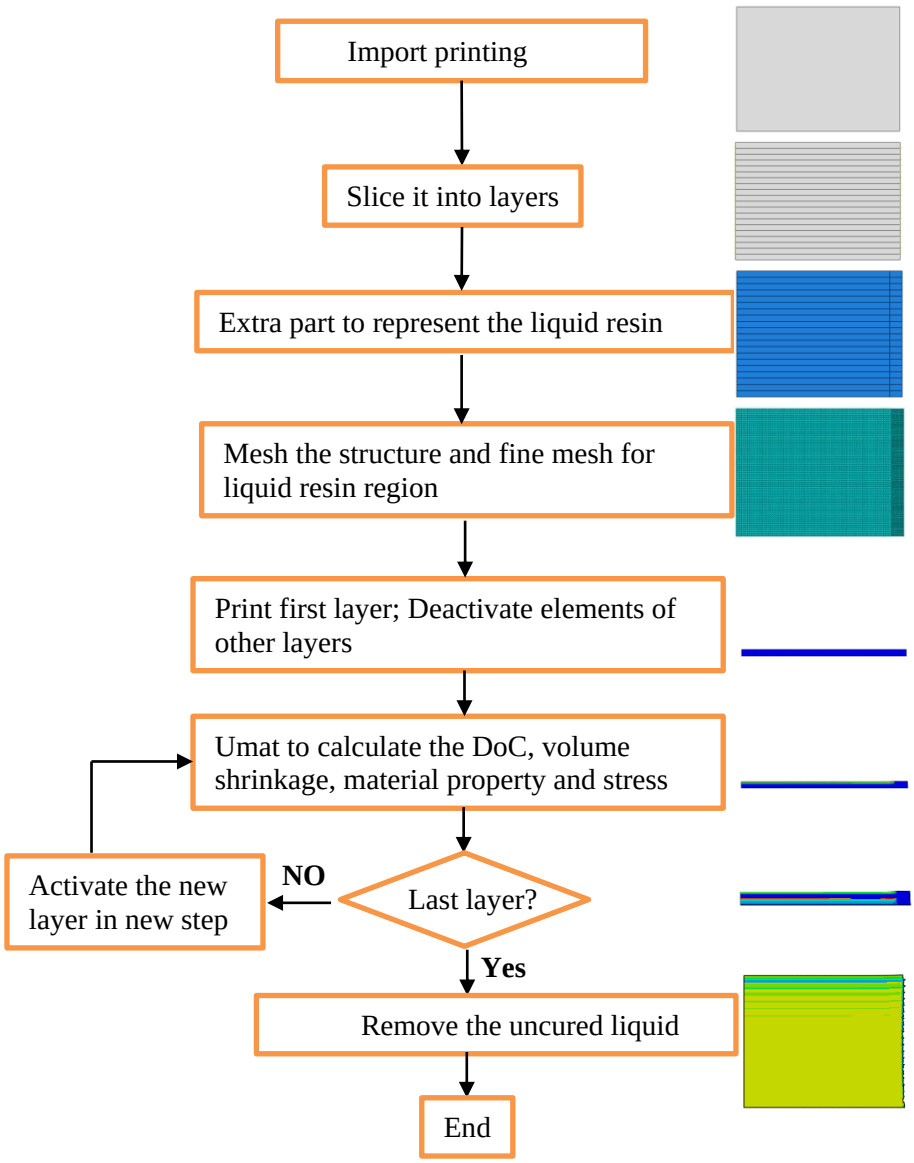

Figure 3.2 FEA Simulation process of 3D printing.

The original model structure can be built by the Abaqus CAE or Abaqus python script or imported from other computer aided design (CAD) system. In the actual printing process, the material shrinks due to the reaction induced volume shrinkage. But the uncured resin around the curing material will fill into the shrunk region to occupy the shrunk space and be cured. If we need to obtain the accurate printing size, the filling process should be simulated. In order to simulate this process, we added extra liquid

element part around the structure with predesigned dimension. Then the model can be partitioned into different layers, which is similar to the slicing process of the actual 3D printing. Next, the structure can be meshed into elements and the element size for the extra liquid resin region should be refined to avoid the numerical interpolation error. After that, we created multiple simulation steps which correspond to the printing process of each layer. In the first printing step, only the elements of the first printing layer were activated and all other elements are deactivated. A user material (UMat) subroutine was implanted in Abaqus to model the chemical reaction kinetics, material conversion, material property evolution, volume shrinkage deformation and residual stress development. And only the materials under the region of the UV light can be cured. The details of the theoretical photo curing model will be discussed in the following sections. After the first layer is cured, the elements in the second layer were activated and cured. Due to the volume shrinkage, the elements near the free boundary maybe largely distorted. Therefore, the nodes position of new layer needs to be revised when the distortion is too large. This process was implemented until the last layer was cured. The whole printing process can be implemented in the python code using the Abaqus python script. Part of the extra liquid element can be cured if they entered the region of the UV light. Only the elements with material conversion p higher than the critical p_c can be considered as the part of the printed structure. Because the extra liquid elements need very fine element size which increased the computational resource consumption, we only use them to verify the simulation method and the printing size of the actual structure.

3.3 The material property characterization during the photocuring of the resin

During the photocuring process, the resin material will gradually change from liquid monomer to solid polymer and the functional group of the material, the C=C double bond in our system, will be reduced by the chemical reaction. To characterize the material property change during the chemical reaction, we first run the FTIR test to investigate the chemical reaction kinetics. We cured thin samples of the resin between two glass slides. By controlling the curing time, we obtained samples with different DoCs. The samples were tested using the FTIR (Nicolet iS50, Thermo Fisher Scientific, Waltham, Massachusetts, USA) in the attenuated total reflection (ATR) mode. The peak area of the C=C bonds absorbance spectra (frequency 1635 cm^{-1} and 1620 cm^{-1}) was used to characterize the conversion of the material. The C=O stretching vibration peak at frequency 1725 cm^{-1} was used as the internal reference to normalize the measured value to avoid the sample difference. We can write the DoC φ of the resin as[115]:

$$p = 1 - \frac{(A_{1635cm^{-1}} + A_{1620cm^{-1}}) / A_{1725cm^{-1}}}{[(A_{1635cm^{-1}} + A_{1620cm^{-1}}) / A_{1725cm^{-1}}]_{t=0}} \tag{3-1}$$

where $A_{1635cm^{-1}}$, $A_{1620cm^{-1}}$, $A_{1725cm^{-1}}$ are the absorbance peak area at 1635 cm^{-1}, 1620 cm^{-1}, and 1725 cm^{-1} respectively. The FTIR results are shown in Figure 3.3(a). We can see that the concentration of the C=C bonds decreases dramatically with curing time. And we calculated the DoC of the material using Eq. (3-1) and the results are shown in Figure 3.3(b). The chemical reaction proceeded very quickly in the first few seconds and then the reaction rate became slow due to high viscosity of the cured material.

We also tested the modulus change of the cured resin by using the uniaxial tension tests. A dynamic mechanical analysis (DMA) tester (model Q800, TA Instruments, New Castle, DE, USA) was used to stretch the thin film sample with strain rate 5%/min at the

room temperature. The dimension of the testing sample is 10mm×2.5mm×0.11mm. To avoid the conversion gradient in the cured material, we prepared separate resin without the photoabsorber and cured this resin between glass slides to make thin film samples. The stress-strain curves of samples with different DoCs are shown in Figure 3.3(c). And the modulus of the material with different DoC is plotted in Figure 3.3(d). We can see that the modulus of the material changed dramatically when the conversion of the material is high.

Unitizing these experiment results, we will develop a theoretical model to describe the chemical reaction kinetics, material property evolution, volume shrinkage deformation and mechanics during 3D printing curing process.

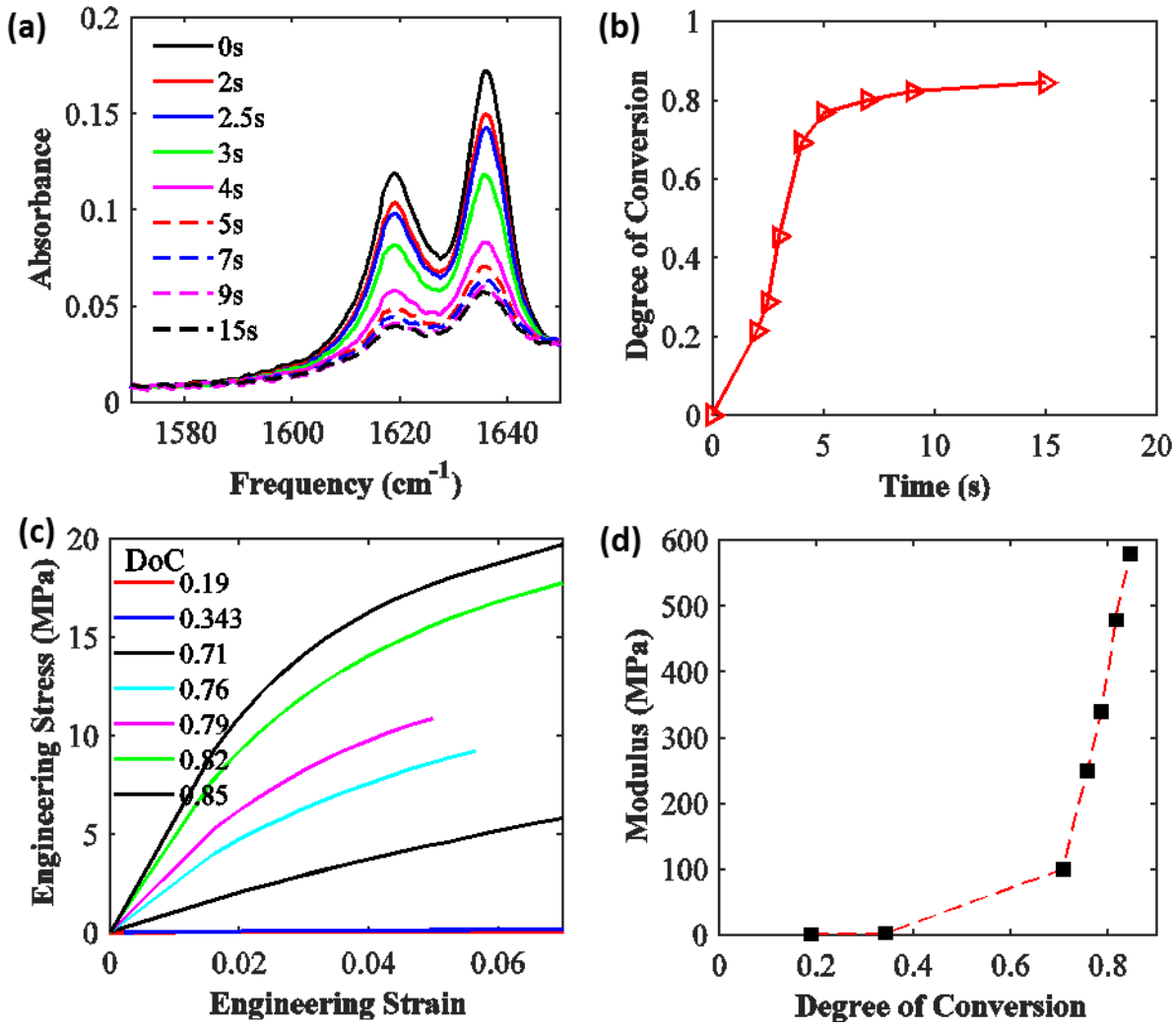

Figure 3.3 The reaction kinetics and material evolution during UV photocuring process. (a) The FTIR spectra of the resin material with different curing time. (b) The calculated DoC using the FTIR results. (c) The modulus change as a function of DoC. (d) The volume shrinkage as a function of DoC.

3.4 Theoretical model for material property evolution and mechanics during photocuring process

3.4.1 *The photocuring chemical reaction kinetics during printing*

In order to accurately describe the material property evolution process of the photocuring process during the 3D printing, we need to model the photopolymerization

reaction kinetics. The photopolymerization reaction kinetics has been widely investigated [13,86,93,116,121,122,148,165]. Previously we have studied the chemical reaction and material evolution in the photopolymerization process using a theoretical model which considers the effects of the diffusion controlled reaction rate[115]. Here we will simply introduce this model and apply it to the 3D printing simulation.

The photopolymerization reaction is described using a set of first order reaction equations. The light propagation through the liquid resin is attenuated due to the absorption of photoabsorbers and photoinitators. The light intensity variation in the spatial position in the resin can be described by the Beer-Lambert law. Since the light is irradiated in the perpendicular direction of the liquid resin surface, the 1D case of Beer-Lambert law is used:

$$\frac{\partial \mathrm{I}(z,t)}{\partial \mathrm{z}} = -(\alpha \mathrm{C}_I(z,t) + W_a A_{absorber}) I(z,t) \tag{3-2}$$

where I is the light intensity, z is the coordinate of the material point in the depth direction, α is initiator molar absorptivity, C_I is the initiator concentration, $A_{absorber}$ is the absorption from photoabsorbers, W_a is the weight percentage of the photoabsorbers. For the 3D printing resin, photoabsorbers are mainly used to attenuate the light to avoid the over cure and the light absorption is mainly caused by the photoabsorbers, i.e. $W_a A_{absorber} >> \alpha C_I$.

The typical polymerization reaction can be described by four steps: photodecomposition, initiation, propagation and termination[41,115,116,119,120]. In the photodecomposition step, the photo initiators absorb the photons and decompose into active species. The evolution of the initiator concentration can be calculated as [30,88,93]

$$\frac{\partial C_I(\mathbf{x},t)}{\partial t} = -\beta I(\mathbf{x},t) C_I(\mathbf{x},t) \tag{3-3}$$

where β is the photodecomposition rate. Then the concentrations of radicals and oxygens can be calculated as

$$\frac{\partial C_R(\mathbf{x},t)}{\partial t} = m\beta C_I(\mathbf{x},t) I(\mathbf{x},t) - 2k_{Term}(C_R(\mathbf{x},t))^2 - k_O C_R(\mathbf{x},t) C_O(\mathbf{x},t) \tag{3-4}$$

$$\frac{\partial C_{\mathrm{O}}(\mathbf{x},t)}{\partial t} = -k_{\mathrm{O}} C_{\mathrm{O}}(\mathbf{x},t) C_R(\mathbf{x},t) \tag{3-5}$$

where k_{Term} is the termination rate, C_O , C_{R} , k_{O} are the concentrations of oxygen, the radicals, and the reaction rate between oxygen and radicals respectively, *m* is the number of radicals generated in photodecomposition. For the photoinitiator Irgacure 819 used in this paper, two radicals can be generated for each photo initiator i.e. m=2. The active radicals can be terminated by bimolecular termination when two active radicals react, which can be described by the second term in the right-hand side of Eq. (3-3). The oxygen molecule can also react with radicals to reduce the concentration of radicals (the third term in Eq. (3-3)). The oxygen in the resin will be consumed by the radicals and its concentration evolution can be calculated by Eq. (3-4).

After activated by radicals, the functional group of monomer, C=C double bonds here in our system, will be reactive and can connect with other monomers to form polymer chains and crosslinks. The C=C double bonds will be consumed during the polymer chain propagation step. The concentration of the unconverted functional groups can be described by:

$$\frac{\partial C_{\mathrm{M}}(\mathbf{x},t)}{\partial t} = -k_p C_M C_R \tag{3-6}$$

where C_M is the concentration of unconverted double bonds, and k_p is the propagation rate. The reaction extent can be described by the DoC of the double bonds:

$$p(\mathbf{x},t) = 1 - \frac{C_M(\mathbf{x},t)}{C_M(\mathbf{x},t=0)} \tag{3-7}$$

Previous research has shown that the propagation rate k_p and the termination rate k_{Term} are controlled by the radical diffusion process[98,124] or the viscosity of the curing material. The viscosity can be related to the DoC of the material and then the propagation rate and the termination rate can be linked to the DoC by following equations:

$$k_p = \frac{\mathrm{k}_{p0}}{1 + \frac{\mathrm{k}_{p0}}{\mathrm{k}_{p,\mathrm{D0}}} e^{cp}} \tag{3-8a}$$

where k_{p0} is the polymerization rate at p=0, $\mathrm{k}_{p,\mathrm{D0}}$ is a parameter used to characterize the diffusion-controlled propagation reaction, e^{cp} is the relative viscosity of the cured material.

$$k_{Term} = \frac{1}{1/k_{t,SD} + \exp(cp)/k_{t,TD0}} + \frac{C_{RD}(1-p)k_{p0}}{1 + \frac{k_{p0}}{k_{p,D0}}\exp(cp)} \tag{3-8b}$$

where $k_{t,SD}$ is the segmental diffusion rate, $k_{t,TD0}$ is the center-of-mass translational diffusion rate at zero conversion. The first term in the equation represents the termination due to species translational diffusion of radicals. The second term describes the reaction diffusion termination rate. C_{RD} is the reaction diffusion proportion parameter. The detailed description of the diffusion controlled reaction rates can be found in previous

research[91,92,115,124,126]. By solving these equations we can get the DoC evolution of the material during photocuring.

3.4.2 *The material property evolution with DoC*

After determining the DoC evolution of the material, we can relate the material property to the DoC. Previous researchers have used the constant modulus and Poisson's ratio to represent the property of resin material in stereo lithography apparatus (SLA) [55,166]. Here we use an empiric model to relate the modulus as the function of the DoC of the resin material[9,132,133].

$$E = E_c \exp(bp) + E_d \tag{3-9}$$

3.4.3 *Volume shrinkage and mechanics during 3D printing process*

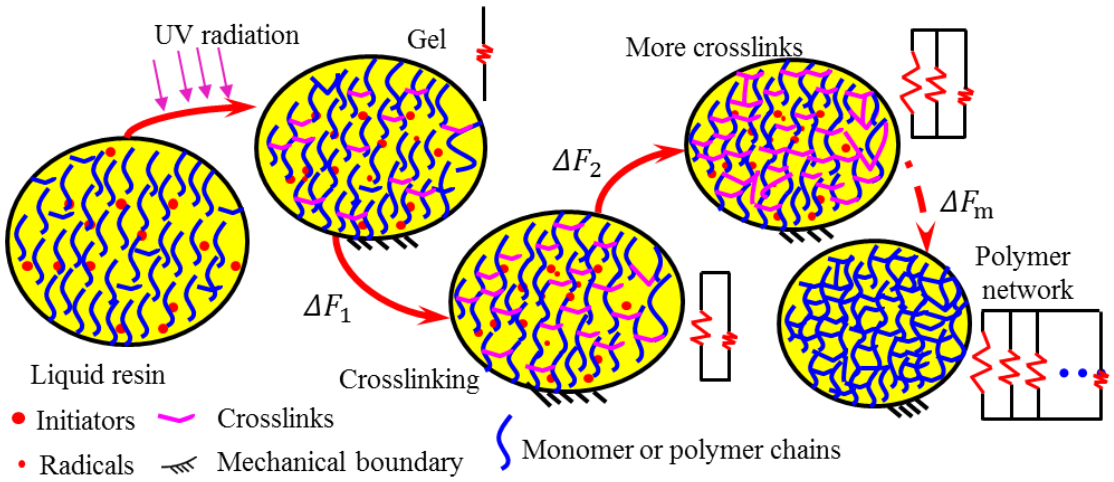

Figure 3.4 A schematic to show the material evolution process and mechanical deformation during photopolymerization.

During 3D printing, the material changes from liquid to solid state and the volume shrinkage also evolves. To solve the problem of the coupling between the material

property evolution and volume shrinkage deformation, we build a phenomenal phase evolution model which considers the photopolymerization as a crosslinking increasing process. In this model, we divided the photocuring process into small time steps and assume the crosslinks formed at different time steps as the newly born 'phase'. We assume that the newly formed crosslinks are in stress and strain free state and cannot carry any current load when they are formed [102,131]. Therefore, the newly formed crosslinks will not affect the current stress until the deformation state has changed. With the increase of the crosslinks, the stiffness of the material will increase. To model this we use the spring to represent the crosslinks formed at different time steps. At each time step, new crosslinks form and we add a new spring to represent them. The deformation of the crosslinks formed at different time step will be accumulated after they were born. Figure 3.3 explains this process. More detailed description can be found in our previous paper. In our previous model for the photopolymerization, we added the multiple Maxwell elements to describe the viscous properties of the cure polymer. Here we will apply this phase evolution model to the complex layer-by-layer 3D printing process. Usually the layer thickness of actual printing is relatively small, about ~30 μm-200 μm, and we need many printing simulation steps for the actual printed structure. Since we focused on the volume shrinkage induced distortion and the volume shrinkage strain is relatively small, here we only consider the stiffness increase of the material to simply the model and reduce the computation time and resource consuming.

The deformation gradient of the curing material can be decomposed into the shrinkage-induced deformation and the mechanical deformation[130]:

$$\mathbf{G} = \mathbf{G}^{M}\mathbf{G}^{s} \tag{3-10}$$

where $\mathbf{G}^M$, $\mathbf{G}^s$ are the mechanical and volume shrinkage deformation gradient respectively. The curing shrinkage is isotropic; therefore, the shrinkage deformation gradient can be calculated as [130]:

$$\mathbf{G}^s = \sqrt[3]{(1-\Lambda)}\mathbf{I} \tag{3-11}$$

where Λ is the volume shrinkage.

For convenience, we set $\mathbf{F} \equiv \mathbf{G}^M$ as the mechanical deformation gradient.

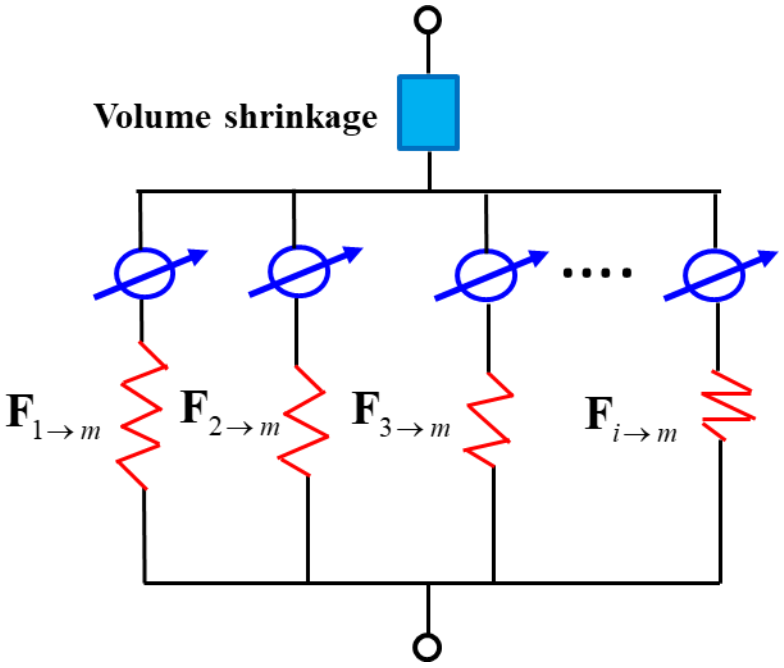

Figure 3.5 The one-dimensional rheological analogy for photocuring phase evolution model. The switch will be turned on when new crosslinks form.

Figure 3.5 shows the one-dimensional analogy for this model. We divided the photocuring process into small time increment steps and the springs in this figure represent the crosslinks formed at different time steps. At time increment *m*, we can calculate the number of the newly formed crosslinks ΔN_m during this time interval. The newly formed crosslinks will increase the modulus of the material and the modulus is assumed to be proportional to the crosslink density.

We define the crosslink fraction Δf_m as:

$$\Delta f_m = \frac{\Delta N_m}{N_M} = \frac{\Delta E_m}{\Delta E_M} \tag{3-12}$$

where N_M is the total crosslinks of the fully cured polymer. Here, we term these crosslinks with crosslink fraction Δf_m as a new phase. The conceptual 'phase' is only used to represent the modulus change of the new material and is different from the general phase in the crystalline.

At time increment Δt, a new phase with crosslink fraction $\Delta f_1 = \frac{\Delta N_1}{N_M}$ forms. During this process, the mechanical deformation is increased by $\Delta \mathbf{F}_1$. The stress can be calculated as:

$$\boldsymbol{\sigma}^{total}(t = \Delta t) = \Delta f_1 \boldsymbol{\sigma}(\Delta \mathbf{F}_1) \tag{3-13}$$

At next time step, a new phase with crosslink fraction Δf_2 forms, and the deformation gradient increased by $\Delta \mathbf{F}_2$. The newly formed phase only carries the current deformation $\Delta \mathbf{F}_2$ to satisfy the boundary condition and the deformation of the old phase Δf_1 has changed to $\Delta \mathbf{F}_2 \Delta \mathbf{F}_1$. Then the stress can be calculated as:

$$\boldsymbol{\sigma}^{total}(t = 2\Delta t) = \Delta f_1 \boldsymbol{\sigma}(\Delta \mathbf{F}_2 \Delta \mathbf{F}_1) + \Delta f_2 \boldsymbol{\sigma}(\Delta \mathbf{F}_2) \tag{3-14}$$

In the same manner, at time step t= $t_0 + m\Delta t$, the m-th new phase Δf_m forms. The deformation gradient of the phase formed at time t= $t_0 + i\Delta t$ can be calculated as:

$$\mathbf{F}_{i\to m} = \Delta\mathbf{F}_m ... \Delta\mathbf{F}_{i+1}\Delta\mathbf{F}_i = \prod_{j=i}^{m}{}^{L}\Delta\mathbf{F}_j \tag{3-15}$$

where $\prod_{j=i}^{m}{}^{L}()$ means that the multiplicative operation sequence is toward the left. Then we can calculate the total stress as:

$$\boldsymbol{\sigma}^{total}(t = t_0 + m\Delta t) = \sum_{i=1}^{m}\Delta f_i \boldsymbol{\sigma}(\mathbf{F}_{i\to m}) \tag{3-16}$$

For the polymer material, the stress can be described by the compressible neo-Hookean material model.

$$\boldsymbol{\sigma} = \frac{\mu}{J}(\mathbf{b} - \mathbf{I}) + \frac{\lambda}{J}(\ln J)\mathbf{I}, \mathbf{b} = \mathbf{F}\mathbf{F}^T \tag{3-17}$$

where μ, λ are the shear modulus and Lamé's first parameter of the completely cross-linked polymer respectively, and $\mathbf{I}$ is the second order identity tensor, $\mathbf{b}$ is the left Cauchy–Green deformation tensor, J is the determinant of $\mathbf{F}$, and $\mathbf{F}$ is the mechanical deformation gradient of m-*th* phase in Eq. (3-16).

To calculate the total stress of the whole material, we need to know the crosslink fraction and deformation gradient in each phase. And with the increase of the time steps, the number of phase will also increase. Therefore the information we need to keep track of for each phase will consume large amount of computer memory resources and CPU time. To solve this problem, Long et al. [109,113] developed an effective phase model (EPM) which utilized the equivalent effective phase. At each time step, the deformation and stress are first calculated and then converted into equivalent effective phase. Therefore only the effective phase fraction and effective deformation in each step are recorded,

which largely reduced the consumption of the computational resources. Here we will simply introduce this model and apply it to the 3D printing simulation.

We define the effective phase as a summation of all phases and use it to keep track of the stress and equivalent deformation of the material. We define the effective crosslink fraction $\bar{f}$ and effective deformation gradient $\bar{\mathbf{F}}_m$. The effective crosslink fraction of the effective phase at time t=mΔt is the total crosslink fractions of all phases $\bar{f}_m = f_0 + \sum_{i=1}^{m} \Delta f_i$. The total stresses can be written as:

$$\boldsymbol{\sigma}^{total} = \bar{f}_m \boldsymbol{\sigma}\ (\bar{\mathbf{F}}_m) \tag{3-18}$$

After Δt time, a new phase with crosslink fraction Δf_{m+1} forms and new deformation $\Delta \mathbf{F}_{m+1}$ occurs. We can first calculate the total stress in this step as:

$$\boldsymbol{\sigma}_{m+1}^{total} = \bar{f}_m \boldsymbol{\sigma}(\Delta \mathbf{F}_{m+1} \bar{\mathbf{F}}_m) + \Delta f_{m+1} \boldsymbol{\sigma}(\Delta \mathbf{F}_{m+1}) \tag{3-19}$$

If we write the stress with the effective crosslink fraction and effective deformation gradient using similar formula in Eq. (3-18), we have:

$$\boldsymbol{\sigma}_{m+1}^{total} = \bar{f}_{m+1} \boldsymbol{\sigma}(\bar{\mathbf{F}}_{m+1}) = \bar{f}_{m+1} \boldsymbol{\sigma}(\Delta \bar{\mathbf{F}}_{m+1} \bar{\mathbf{F}}_m) \tag{3-20}$$

Since the total stress of Eq. (3-19) and Eq. (3-20) should be equal, we can obtain:

$$\bar{f}_{m+1} \boldsymbol{\sigma}(\Delta \bar{\mathbf{F}}_{m+1} \bar{\mathbf{F}}_m) = \bar{f}_m \boldsymbol{\sigma}(\Delta \mathbf{F}_{m+1} \bar{\mathbf{F}}_m) + \Delta f_{m+1} \boldsymbol{\sigma}(\Delta \mathbf{F}_{m+1}) \tag{3-21}$$

Here $\bar{f}_{m+1}$, $\bar{f}_m$, Δf_{m+1}, $\Delta \mathbf{F}_{m+1}$, $\bar{\mathbf{F}}_m$ are all known and only the effective deformation increment $\Delta \bar{\mathbf{F}}_{m+1}$ is unknown. It can be solved using the Newton–Raphson scheme. Then

we only need to update and store the effective crosslink fraction $\bar{f}_{m+1}$ and effective deformation $\bar{\mathbf{F}}_{m+1} = \Delta\bar{\mathbf{F}}_{m+1}\bar{\mathbf{F}}_m$ for next time step.

3.5 Results and discussion

3.5.1 *Model results of material property evolution and volume shrinkage deformation*

Before we apply the model to the FEM simulation of the 3D printing process, we fitted the experiment results of the chemical reaction kinetics, modulus evolution, volume shrinkage to obtain the model parameters. We first fitted the reaction kinetic using the experiment DoC data and the Eqs. (3-2)-(3-8). The fitted result is shown in Figure 3.6(a). We can see that this model can capture the conversion kinetics of the printing resin. And then we fitted the Young's modulus of the material as the function of DoC using Eq. (3-9). The fitted results are shown in Figure 3.6(b). Previously we have measured the volume shrinkage of the PEGDA 250 material using the density tests[115]. And the experiment results are plotted in Figure 3.6(c). To accurately capture the change of the volume shrinkage with DoC, the volume shrinkage is modeled using the segmental linear fitting as shown in Figure 3.6(c). The fitting equations of the three lines are:

$$\Lambda = \begin{cases} 0.1183p+0.056, & 0.1 \le p \le 0.725 \\ 0.6155p-0.3045, & p \ge 0.725 \end{cases} \tag{3-22}$$

After determining these material parameters, we also obtained the absorption coefficient of the photoabosobers by using the curing depth test of the resin material. We calculated the curing depth of the resin at the same curing time 3s using different absorption coefficients and the determined reaction kinetics parameters and then compared with the

experiment result. The results are plotted in Figure 3.6(d). Then the absorption coefficient can be determined. Table 3-1 summarized the parameters we used for the modeling.

Table 3-1 Parameters used in the modeling and simulation of DLP printing

Parameters for reaction kinetics					
α (m^2/mol)	0	$A_{absorber}$ (m^{-1})	123333.3		
C_{O20} (mol/m^3)	1.05	β (s^2/kg)	3.4466E-4	k_{p0} (m^3/mol/s)	610.3307
kp_{D0}(m^3/mol/s)	1.4955E+9	k_{SD} (m^3/mol/s)	4.3666E+03	c	29.89681
k_{TD0} (m^3/mol/s)	657206.31	C_{RD}	1.03829	K_O (m^3/mol/s)	2644.1
Parameters for modulus evolution					
E_c (MPa)	0.08833	E_d (MPa)	0	b	10.45

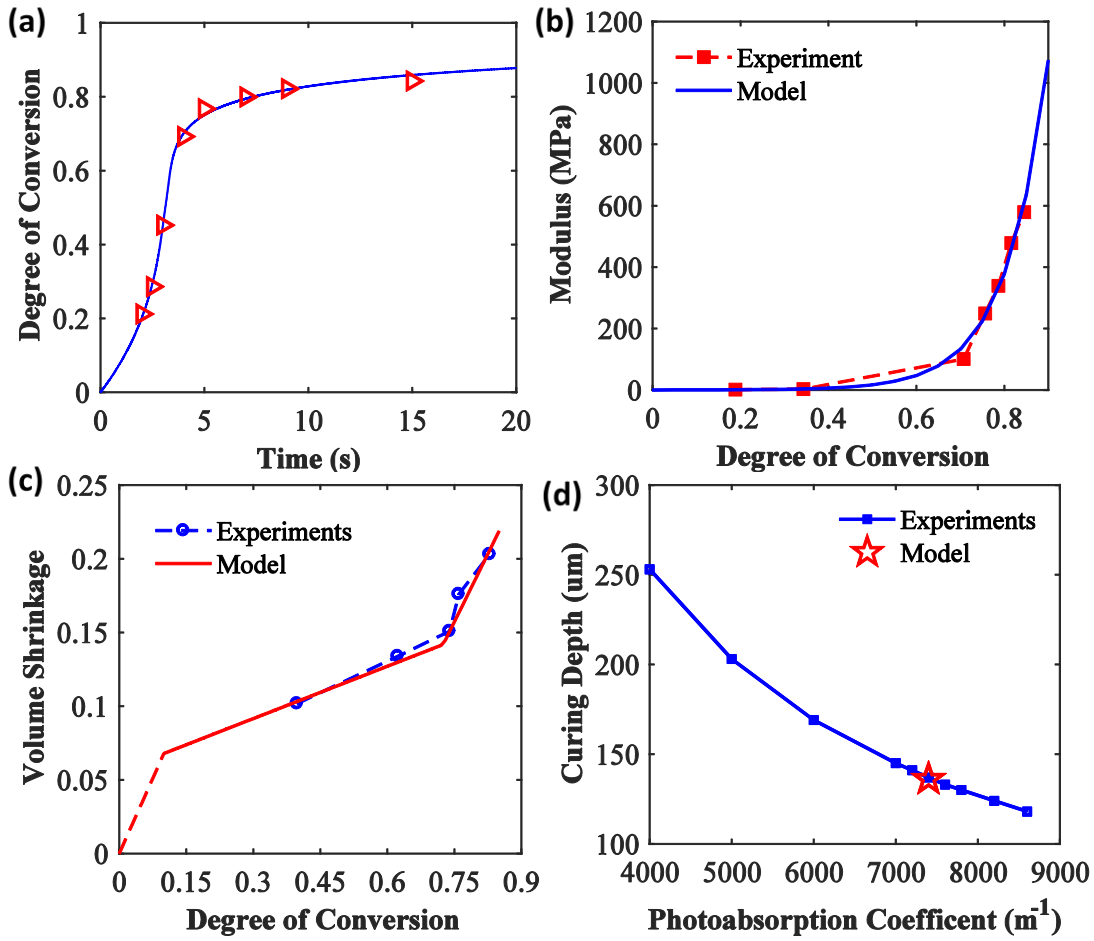

Figure 3.6 The modeling results for the chemical reaction, material property evolution volume shrinkage and the photo absorption coefficient.

3.5.2 *FEM simulation of printing a cuboid*

After obtaining these model parameters, we can apply this model to the FEM simulation of the layer-by-layer 3D printing process. As described in previous section, the layer-by-layer printing is modeled by the inactive element method. All the elements other than those of the first layer are first deactivated when we print the first layer. After the first layer is cured, the elements in the second layer will be activated in the second simulation step. When the elements are activated, the concentrations of each species (photoinitiator, radicals, functional group, and oxygen) are first set to be concentrations of those of the resin material and then the chemical reaction equations will be solved at each time increment. The modulus change, the crosslink fraction, the volume shrinkage induced deformation can be calculated. Then the stress will be calculated and updated.

We first simulated the printing process of a simple cuboid structure. The structure has a designed dimension of 5 mm in width and 10 mm in height, and the printing is along the height direction. The layer thickness is set to be 100 μm, therefore we need to partition the structure into 100 layers, which means we need 100 simulation steps for the printing process. To validate the printing dimension using our simulation, the extra liquid elements were added around the width boundary of the structure. Each layer has 4 elements along the layer thickness direction and 4-node plane strain element (CPE4I) with incompatible modes were used. Obviously with the increase of the layers, the number of elements will increase proportionally and the computational time will also increase. The simulated results are shown in Figure 3.7(a). And the experiment printing structure are shown in Figure 3.7(b). The measured width dimension of the printed structure is about 4.96 mm in simulation and 4.86 ± 0.028 mm, which are very close. Then we measured the light distribution of the light pattern projected by taking a picture of it

and analyzed the color intensity using Matlab as shown in Figure 3.7(c). We found that the light intensity around the pattern edges is much lower than the center part which is caused by the optical aberrations of the image lens and the power distribution of the light beam of the projector. This phenomenon has been investigated by Jariwala et al. [52], which causes the size error of the experiment results.

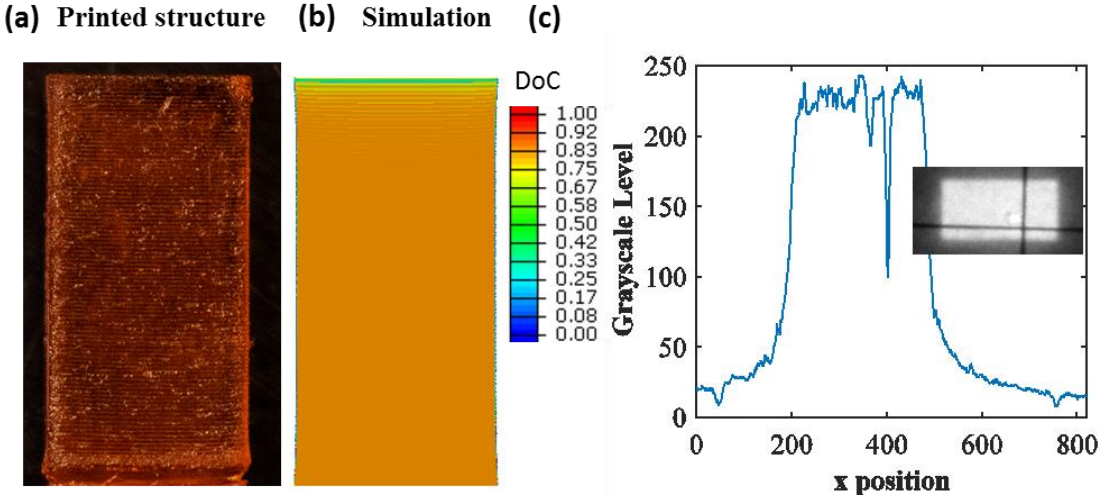

Figure 3.7 FEM simulation of printing a 100-layer cuboid. (a)The experiment result. (b) The simulation result. (c) The relative light intensity distribution of the printing pattern.

3.5.3 *Application of the FEM simulation*

3.5.3.1 Printing of microfluidic channels: the print through error

The microfluidics which utilizes the small fluidic channel to control the flow of liquids has been widely used in drug delivery device, biotechnology, tissue engineering and biomedical engineering[167-169]. DLP printing has been applied to the fabrication of the microfluidic devices[170,171]. During the DLP printing of the microfluidic, the designed flow channels will be filled with the liquid resin. And the light penetration caused by the printing of layers on top of the channels can reduce the printed height of the flow channel,

which is the so-called print through error. If the light penetration is very high and the designed height of the channel is small, the printed channel will be clogged by the light penetration cured material. Therefore, it is important to have a method to estimate the dimension of the printed microfluidics and find proper way to improve the printing quality.

To investigate the print through error of the printing of microfluidic channels, we designed the square channels with different channel sizes and printed with our DLP printer. The light intensity of 5.1 mW/cm^2 is used and the layer curing time is 3 s. The printed results are shown in Figure 3.8(a) - (d). We can see that the printed channel is not in square shape and the height is smaller than the width due to the print through error. Then we did FEM simulations using the same printing condition. We measured the height of the printed channels and compared with the FEM simulation. The results are shown in Figure 3.8(e).

The reduced size of the printed channels will influence its effectiveness. Applying our simulation method, we found that we can improve the accuracy of the printed channel height by delaying the printing of the top cover layers of the channel. Figure 3.9(a) shows the design method. We designed a square channel with height 640 μm and the layer thickness of the printing is set to be 80 μm. And the designed total number of printing layers for the channel is 8. For general printing, we will print the top cover layers for the channel after 8 layers of printing of the channel. Instead, we can print a few more layers of the channel pattern. By using this way, the channel size will increase and we can get the desired channel size. Figure 3.9(b) shows the simulation results. We can see that by printing two more layers of the channel, the channel height will be close to the designed

size. We printed the channels and compared with simulations, as shown in Figure 3.9(b)-(c).

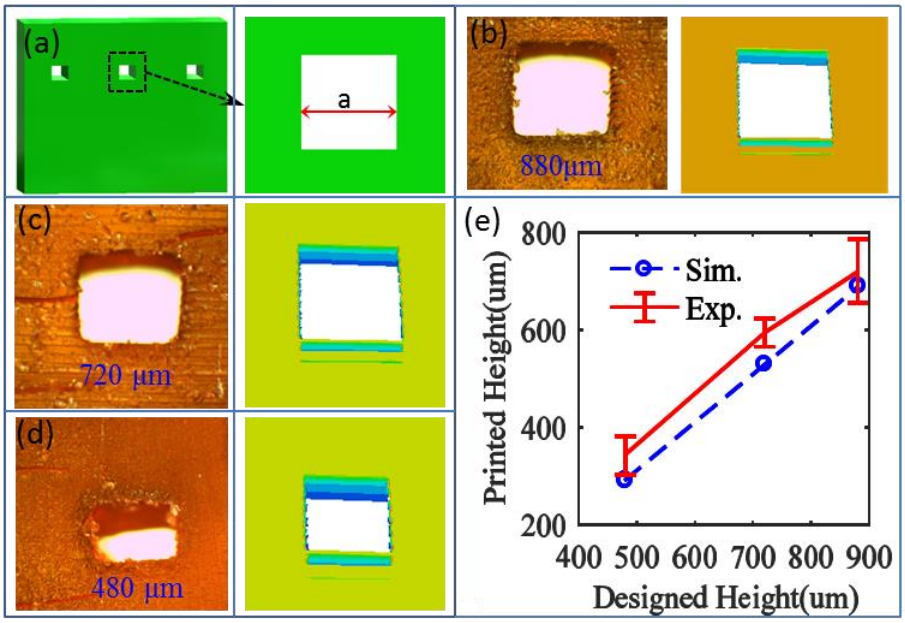

Figure 3.8 Printing of microfluidic channels. (a) The printing model. (b) - (d) The experiment and simulation results of the microfluidic channels with different channel size. (e) Comparison of the channel height of the experiment and simulation result.

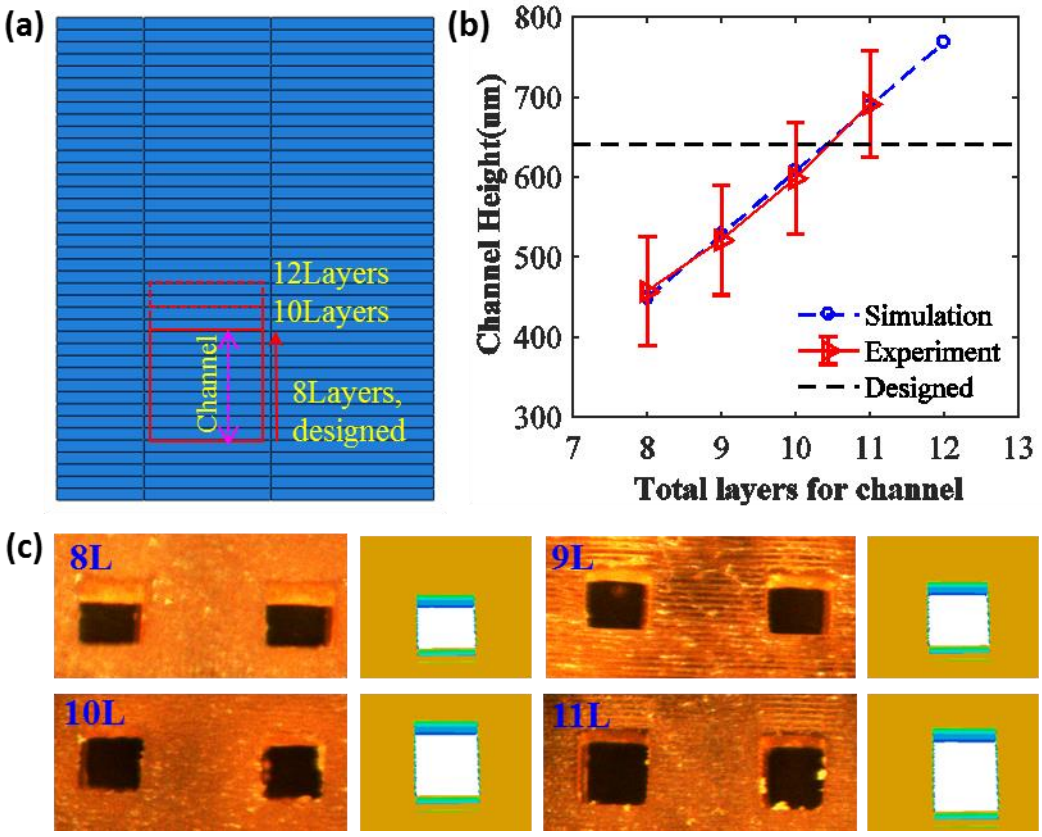

Figure 3.9 Improving the channel size of microfluidic channels by delaying the printing of top cover layers. (a) The design of the printing. The channel height of the designed structure is 640 μm and total designed printing layers for the channel is 8 (layer thickness 80 μm). (b) Channel height as the function of total printing layers for channels. (c) Comparison of experiment and simulation results.

3.5.3.2 Distortion of the printed long bars

Distortion of printed structure will influence the product dimension accuracy and function. Photocuing reaction induced volume shrinkage can cause the warpage of the printed structure [54,170,172]. Here we will show that we can use our simulation to predict the distortion induced printing error of the printed long bars. We printed a long bar structure with dimension 45mm×1.5mm as shown in Figure 3.10(a). The layer thickness of the printing is 60 μm and layer curing time is 3s. The FEM simulation result is shown in Figure 3.10(b). We define the position error of the tip as the printing error. And the experiment result is shown in Figure 3.10(c). We can see that the simulation can capture the deformation of the printed long bar structure. Then we investigated the effect of the layer curing time on the printing error. The experiment result in Figure 3.10(c) shows that the printing error will decrease as the layer curing time increases. The comparison between FEM simulations and experiments is plotted in Figure 3.10(d). The reason of the printing error decreasing with layer curing time is that with increase of the layer curing time, the conversion of the material will be relatively high and uniform and the stiffness of the structure will be higher. The results indicate that for the printing of long solid structure, longer curing time can reduce the printing error.

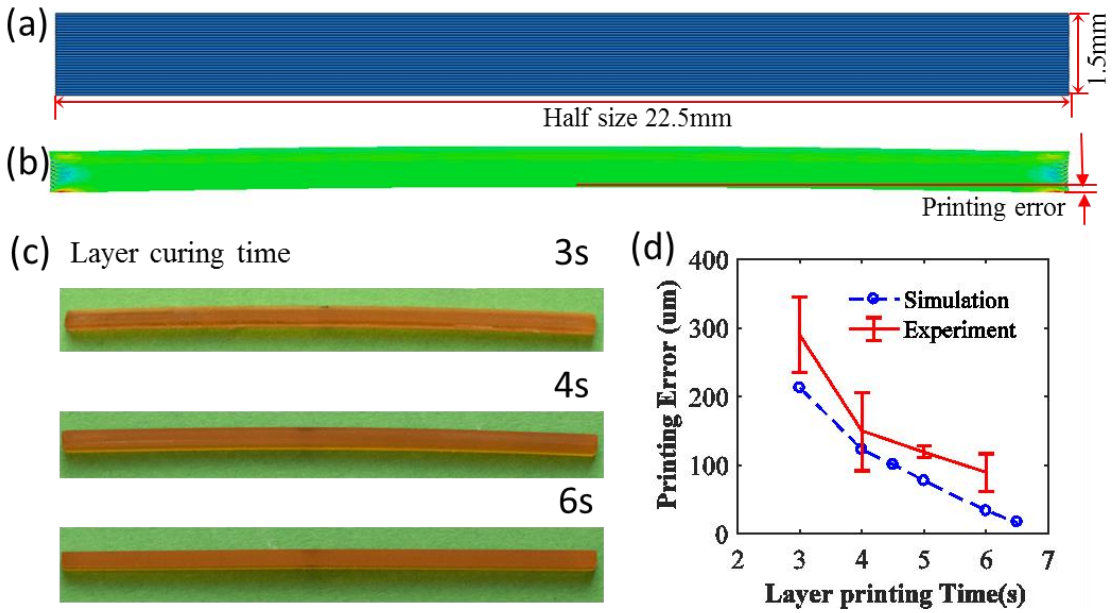

Figure 3.10 Distortion of the printed long bars. (a) The model structure used for the simulations and experiments. (b) The simulation result and printing error. (c) The experiment results of printed structure with different layer curing time. (d) Comparison of experiment and simulation results of printed structure with different layer curing time.

3.5.3.3 The distortion of the printed structure with hanging features

One of the advantages of the DLP printing is that it can print the structure with hanging features such as 3D lattice structure and bridge like structure without supporting material. However the shrinkage induced bending distortion is a severe problem for these structures, especially when the hanging feature is relatively thin or low in bending stiffness. The reason is that some parts of the structure have large-area free surface. Here we demonstrate an example of printing the bridge-like structure as shown in Figure 3.11(a). We used 80 μm layer thickness and 5s for each layer. The simulation and experiment results are also shown in Figure 3.11(a). We can see that the simulation can

match the bending deformation of this hanging structure. We measured the bending angle of the structure at two feature positions, position 1 and 2 in Figure 3.11(a) and compared with the simulation results. The comparison result is shown in Figure 3.11(b). The large bending deformation is harmful for the application of the structure with hanging features. Here we apply our simulation to optimizing the two important printing parameters: the photoabsorber percentage and layer curing time, to reduce the bending deformation. We run a series of simulations with different photoabsorber percentage and layer curing time and calculated their bending angle at position 2 and draw them as a map. The results are shown in Figure 3.11(c). We found that the minimum of the bending angle occurs at lower curing time 3s and photoabsorber percentage around 0.06%. The reason for this is that at lower curing time, the volume shrinkage of the cured material is relatively low and the relatively high photoabsorber percentage can reduce the over cure of the material. It should be noted that at high layer curing time, the print through error will be higher which can reduce the bending deformation due to the increase of the thickness of hanging features but affect the printing accuracy. The optimized results are shown in Figure 3.11(d). We also printed the structures using the calculated parameters and compared with the simulation results in Figure 3.11(d). We can see that with proper photoabsorber percentage and layer curing time the bending deformation of hanging structures can be reduced and the FEM simulation can be a good tool to optimize the printing conditions.

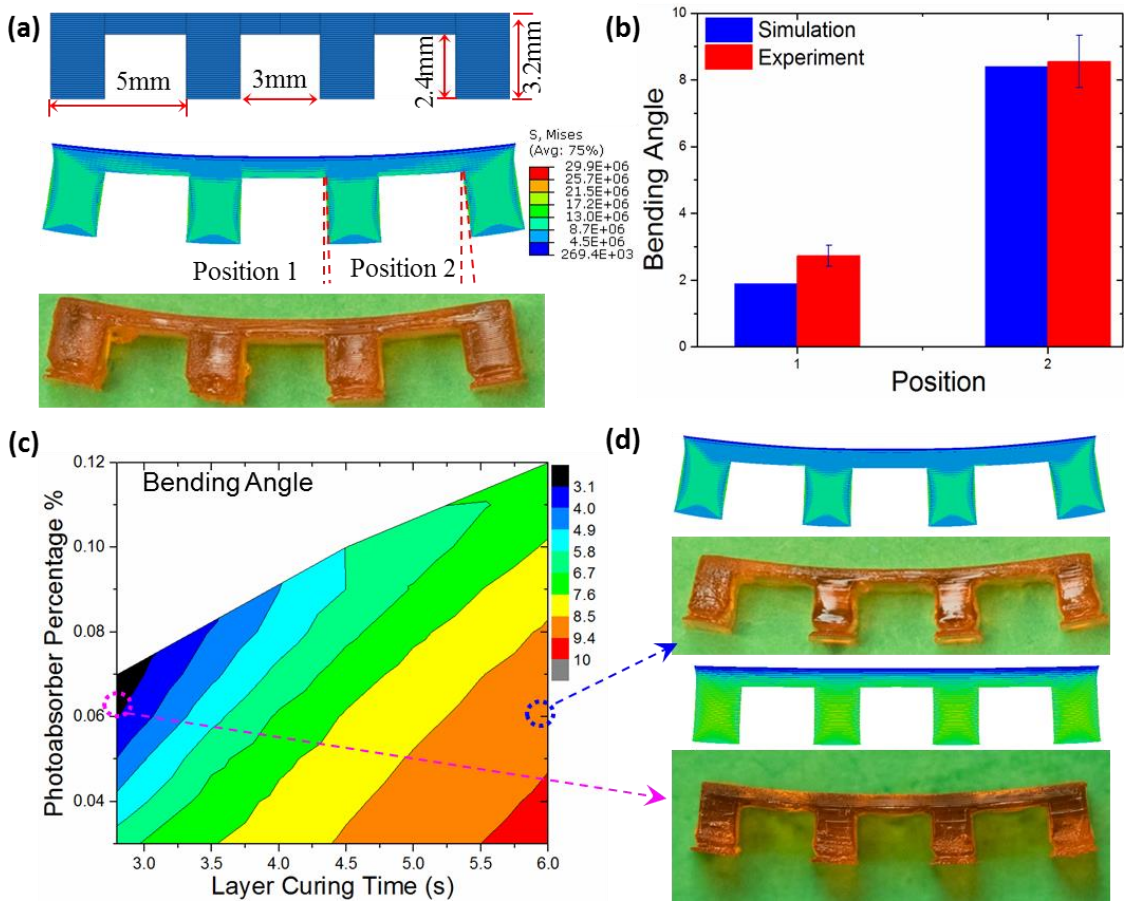

Figure 3.11 Distortion of the printed structure with hanging features. (a) The model structure used for the printing and the simulation and experiment result. (b) The comparison of the bending angle between FEM simulation and experiment result. (c) The map of simulation results of bending angle at position 2 with different photo absorber percentage and layer curing time. (d) The comparison of the simulation and experiment results.

3.6 Conclusions

In this chapter, the volume shrinkage induced distortion of the DLP printed polymer structures was investigated by experiments, theoretic modeling and FEM simulations. FTIR tests and mechanical tests were performed to investigate the chemical reaction kinetics and the material property evolution process during the curing process. And the DoC of the resin material is used as internal variable to characterize the material property

and volume shrinkage. A theoretical model is built to describe the light intensity attenuation, chemical reaction kinetics, DoC of reaction functional group, volume shrinkage deformation and the mechanics during photocuring process. The phase evolution model is used to decouple the material evolution and volume shrinkage deformation and calculate the stress development during photocuring. Then the theoretic model is applied to the FEM simulation to simulate the layer-by-layer DLP 3D printing process. The printing distortions caused by the volume shrinkage of the typical DLP 3D printing structures were investigated by the FEM simulations. The comparison between the experiments and simulations indicate that the theoretical model can capture the distortion behavior of the printed structure. By utilizing the FEM simulation tool we can optimize the printing parameters to reduce the printing distortion.

CHAPTER 4. REVERSIBLE SHAPE CHANGE STRUCTURES BY GRAYSCALE PATTERN 4D PRINTING

4.1 Introduction

Reversible shape change (RSC) structures and devices are highly desirable in many science and engineering applications such as mechanical actuators [173-175], soft robotics [174,176], and artificial muscles [177]. To achieve an RSC structure, active materials that can respond to external stimuli such as heat, light or electric field are used together with the other non-active materials. Traditional active materials such as water responsive hydrogel[178] and liquid-crystal elastomer [176,179] have been widely investigated. Recently, Han et al. utilized the thermo-responsive Poly(N-isopropylacrylamide) (PNIPAAm) hydrogel to create active micro-structures by 3D printing[8]. However, many RSC materials, such as liquid crystal elastomers, require tedious preparation procedures. In addition, assembling them into a 3D complex object requires the accurately placing the RSC material, which usually is a significant challenging job (if not impossible). Advanced 3D printing technologies, especially multi-material 3D printing, provide the possibility to design and fabricate RSC structures[178]. However current multi-material printing depends on expensive commercial 3D printers and the materials are limited by the printer. Recently, Zhao et. al [9] provided a simple way to introduce material property gradient in the light cured polymer sheet and achieved reversible self-folding and unfolding origami structures. In this method, the material property difference was created by the grayscale light pattern. The grayscale light pattern is used to control the light intensity distribution of the projected light pattern. The different light intensity resulted in

the different crosslinking densities in the photocured polymer sheet. The uncured oligomers in the loose crosslinked polymer network could be washed out in water, which induced the volume shrinkage of the less cured part and the bending deformation of the photocured polymer sheet. The bent structure could recover its initial flat shape when immersed in acetone. However, the two drawbacks of this method were that the initial 2D shape has to be a thin film and bending only occurs toward one side of the thin film. If one would like to have bending deformation toward both sides, the sample needs to be irradiated twice from both the top and bottom surfaces. To overcome this drawback, in this paper, we proposed a 3D printing method by utilizing the grayscale pattern to control the light intensity distribution of a digital light processing (DLP) printer to achieve the different crosslink density inside the printed parts and apply this method to create the RSC structures. Previously, Huang et al.[180] used the different light exposure time to create conversion gradient in the digital light printed 2D sheet and the swelling ratio difference in water was utilized to created active structures. Here in our paper, light irradiation time in each layer was the same; we used the designed digital mask patterns with prescribed grayscale distribution to control the light intensity distribution during printing and thus the different crosslink density distribution in the printed part. In addition, in the previous works, including the work by Huang et al.[180] and our work[9], light was irradiated on one layer only, therefore only a 2D thin sheet was printed. These approaches are not 3D printing. In this chapter, 3D structure with different crosslink density in different part was created by DLP 3D printing in a layer-by-layer manner. Therefore the printed structure was not limited to the 2D sheet and complex 3D structures with reversible shape change ability could be printed. In the layer-by-layer printing

process, each layer would receive multiple light exposure because light penetration. To address this challenge, a theoretical model was developed to describe the conversion of the material during the 3D printing. The research work presented in this chapter has been accepted for publication in *Multifunctional Materials* in 2018 [181].

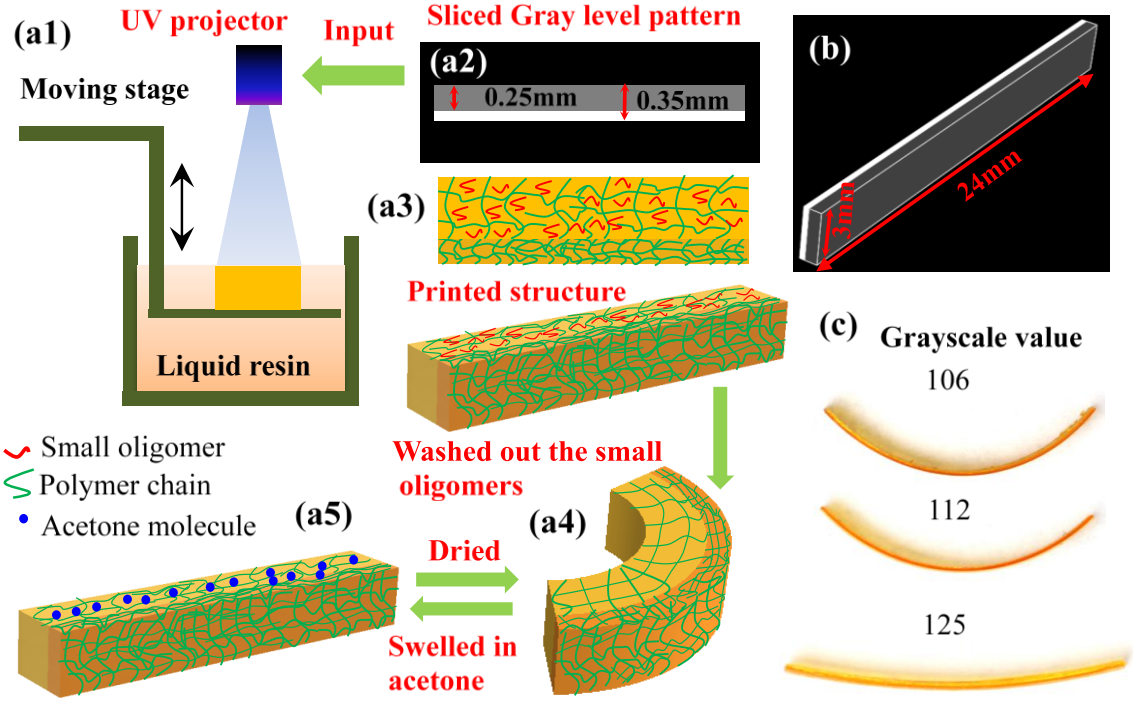

Figure 4.1 The grayscale 4D printing method. (a) Schematics to show the grayscale 4D printing method. (a1) The DLP printing method. a2) A representative grayscale pattern for printing. a3) The printed structure with different crosslink density. a4) The bent structure after desolvated in water. a5) The recovered structure in acetone. The shape change from a4) to a5) is reversible. (b) A designed grayscale printing structure. (c) The bending deformation of the printed structure after desolvation with different grayscale value in the gray part shown in (c).

Figure 4.1(a) illustrates the grayscale 4D printing method. A DLP printer which utilized a UV projector as the light source and a linear motor stage as the motion driver of the printing stage was built for printing photocurable liquid resin (Figure 4.1(a1)). The resin consists of poly(ethylene glycol)diacrylate (PEGDA, Mn 250) oligomers, butyl methacrylate (BMA), Butyl acrylate (BA), photoinitiators (Irgacure 819), and

photoabsorbers (Sudan I). The designed structure was first sliced into pictures corresponding to each printing layer. The designed grayscale of each picture at the different spatial position was processed by Matlab (The MathWorks Inc., Natick, MA, USA) code. The grayscale pictures were then passed to the UV projector for printing (Figure 4.1(a2)). Here, the central idea was that darker light meant lower light intensity and thus produced the material with a lower crosslink density. By this way, we could create a structure with different crosslink densities at different spatial positions (Figure 4.1(a3)). After printing, we immersed the structure into a water bath to let the small oligomers inside the less crosslinked part diffuse out of the structure, or the "desolvation" process[9,182,183]. After desolvation, we removed the structure from the water bath and let it dry in the air. The less crosslinked part shrunk due to the loss of oligomers while the highly crosslinked part did not change. Thus the printed structure could deform towards the less cured part (Figure 4.1(a4)). If the grayscale patterns could be well designed, we could print a variety of self-folding structures using the desolvation induced bending deformation. If we put the bent structure into the solution with proper solubility parameter and the less cross-linked part could absorb the solution (here we use acetone) and swell, which forced the bent structure to recover. Acetone was used as the swelling medium because the less-cross-linked PEGDA network had good swelling ability in acetone and due to the similar solubility parameters the swelling response was rapid. In addition, acetone could easily evaporate from the swelled structure due to its relatively fast volatile property. Therefore the swelling and recovery process could be relatively fast. If we removed it from acetone solution, the acetone molecules would volatile out of the

structure and the recovered structure would bend again. Therefore the shape change was reversible (Figure 4.1(a5)).

4.2 Materials and Methods

4.2.1 *Materials and Printing method*

A DLP printer which utilized a UV projector (light weave length 385nm, PRO4500, Wintech Digital Systems Technology Corp., California, USA) as the light source and linear motor stage as the motion driver of the printing stage was built for the printing of photocurable liquid resin. The materials of the resin consisted of poly(ethylene glycol)diacrylate (PEGDA, Mn 250) oligomers, butyl methacrylate (BMA), Butyl acrylate (BA) and the weight ratio of three materials is 3:0.67:0.33. 0.7% photoinitiators (Irgacure 819), and 0.07% photoabsorbers (Sudan I) are added to the resin. PEGDA material was used as the base material of the resin because previous research had shown that it had good desolvation ability[9]. But if the pure PEGDA material was cured to high conversion, the modulus of the printed material was very high which would increase the bending stiffness and reduce the bending curvature. To solve this problem, we added the small monomers BMA and BA to soften the printed material.

Here we used the grayscale value of each pixel of the sliced printing image to control the light intensity. Here, we digitize the process and use software to precisely control the grayscale. The printing images used in this paper were stored as 8 bits per sampled pixel. Therefore the grayscale value ranges from 0 to 255, which represents pure black color to pure white. The grayscale pattern was then projected on to the liquid resin by using a digital micromirror device (DMD) projector, which convert the grayscale pattern into

light intensity: a 0 gray (black color) corresponds to 0% light intensity (no light), and the 255 corresponds to 100% light intensity (full light). The Stl file of the designed structure was first sliced into grayscale images corresponding to each printing layer by using the slicer software Creation Workshop (DataTree3D, Dallas, Texas, USA). The sliced structure is in white color (grayscale 255). To produce grayscale image, the darker color part of the structure was cut out from the whole structure in Solidworks software and the remaining white color part was also sliced into images using the same method. By comparing the sliced image of each layer of the whole structure with the white color part using the Matlab (The MathWorks Inc., Natick, MA, USA) code, the grayscale value of the darker color part and white color part can be set. Since the light intensity of the grayscale pattern at different parts is different, the conversion of material at different parts is different under the same layer curing time. During printing, layer printing time was 9.8s and the layer thickness was 50 μm.

4.2.2 *Desolvation and swelling test*

The printed structure was put into a glass beaker with a water-based solution (Volume ratio water: acetone=15:1). To accelerate the desolvation process, the beaker was put into a digital ultrasonic cleaner (Vevor Machinery Equipment co., Los Angeles, USA) to wash out the uncured monomers. The temperature of the ultrasonic cleaner was controlled to be around 45^{o}C and the total desolvation time was about 1.5 hour. Here we used the shape change to determine the desolvation extent of the uncrosslinked oligomers. The structure was immersed in the water solution and the shape change continued with the desolvation process. When the shape became stable, we assumed that the desolvation process stopped. After the washing step, the water solution was taken out and the sample

was put into the fume hood to dry for about 3 hours. The dried structure was then immersed in pure acetone for about 10min to let the bent structure to recover its shape.

4.2.3 *Material characterization*

FTIR tests were used to characterize the degree of cure (DoC) of the cured sample. To avoid large DoC gradient in the cured material, we made new resin with the same molecular weight ratio as the printing resin but without photoabsorbers. A mold was made by using two glass slides and 0.11mm thick shims. The resin was then injected into space between the two glass slides. By controlling the curing time, we created samples with different DoCs. An FTIR (Nicolet iS50, Thermo Fisher Scientific, Waltham, Massachusetts, USA) with the attenuated total reflection (ATR) accessory was used to measure the DoC. The DoC of the C=C bonds was characterized by the decrease of the infrared (IR) absorbance of the C=C bonds. We used the peak area of the absorbance spectra at the frequency 1635 cm^{-1} and 1620 cm^{-1} to calculate the conversion of the C=C bonds. To avoid the sample difference, the C=O stretching vibration peak at frequency 1725 cm^{-1} was used as the internal standard. The DoC φ was calculated as[184]:

$$\varphi = 1 - \frac{(A_{1635cm^{-1}} + A_{1620cm^{-1}}) / A_{1725cm^{-1}}}{[(A_{1635cm^{-1}} + A_{1620cm^{-1}}) / A_{1725cm^{-1}}]_{t=0}} \tag{4-1}$$

where $A_{1635cm^{-1}}$, $A_{1620cm^{-1}}$, $A_{1725cm^{-1}}$ are the absorbance peak area at 1635 cm^{-1}, 1620 cm^{-1}, and 1725 cm^{-1} respectively, and $[(A_{1635cm^{-1}} + A_{1620cm^{-1}}) / A_{1725cm^{-1}}]_{t=0}$ is the peak area ratio of the unreacted solution. The conversion of the resin has a maximum value $\varphi_{\max}$. To simplify the modeling of the conversion kinetics, we used the normalized conversion to

describe the reaction kinetics and the material properties. The normalized conversion is defined as $p = \varphi / \varphi_{\max}$.

The uniaxial tests were also performed using the dynamic mechanical analysis (DMA) tester (model Q800, TA Instruments, New Castle, DE, USA) to measure Young's moduli of the samples with different DoCs. The thin film sample (10mm×3mm×0.11mm) was stretched using a constant stress rate 1 MPa/min at the room temperature. The stress-strain curves were used to calculate the moduli of samples with different DoCs.

4.3 Results and discussion

4.3.1 *Experiment Results*

Figure 4.1(b) illustrates the 3D printed strip structure. The white part of the model had the gray level of 255 and the dark part was assigned with different grayscale. We used the same printing time 9.8s for each layer and 40 layers are printed. After desolvation, the sample bent with different bending curvatures (Figure 4.1(c)). We can see that the bending curvature decreased with the grayscale value. The reason was that under the same printing time low grayscale value or low light intensity produced less crosslinked polymer network and thus more uncured oligomers could be washed out to induce larger bending deformation. To help the design of the self-folding and unfolding structures, we conducted experiments to characterize the photocuring reaction kinetics, material property and final bending curvature and developed corresponding theoretical models. Figure 4.2(a) shows Young's modulus as a function of normalized conversion. We can see that the modulus changed dramatically with the increase of the material conversion. We also measured the volume change of the cured samples with different

conversions after desolvation and swelling process shown in Figure 4.2(b). The volume ratio between the desolvated and printed original structure increases with increase of the conversion, which means that the desolvation induced volume shrinkage deformation decreases with the conversion. At high conversion, volume ratio will approach 1.0 and no volume shrinkge will happen. The reason is that the material is highly crosslinked at high conversion. Therefore the ratio of less-crosslinked oligmer is low and cannot be washed away. The swelling induced volume expansion deformation decreases with the conversion. Therefore the bending curvature after desolvation will decrease with the increase of the conversion. Figure 4.2(c) shows the experiment result of the bending curvature of the printed strip created by different grayscale. With increase of grayscale value, the light intensity will be higher and the printed material will have high conversion. As expected the bending curvature after both desolvation and swelling will decrease with increase of grayscale value. To quantitatively describe the deformation behavior of the printed material, a theoretical model was built and described in the following section.

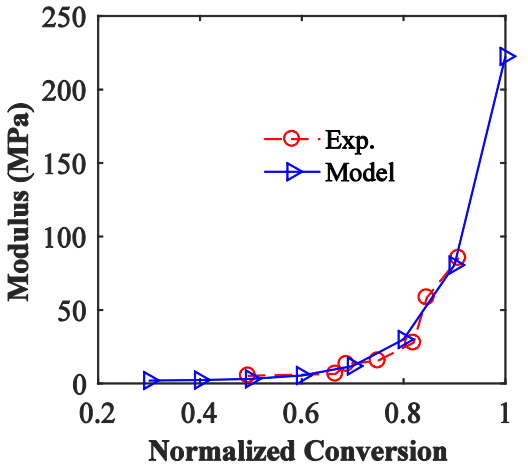

(a)

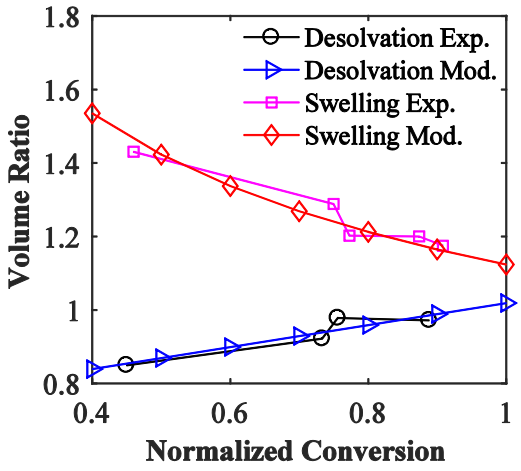

(b)

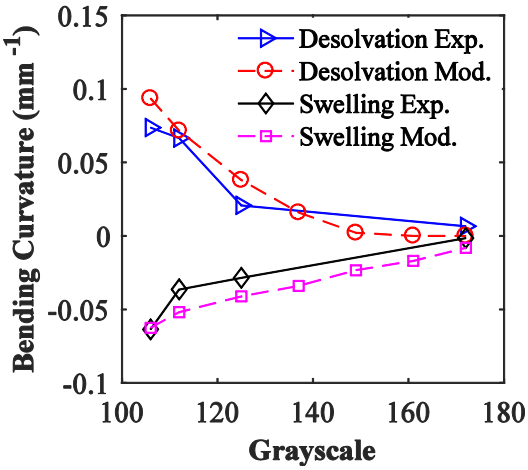

(c)

Figure 4.2 Material property characterization and bending curvature of the printed strip with different gray level. (a) The elastic modulus of the cured material with the different normalized degrees of conversion. (b) Experiments and modeling results of volume ratio after desolvation process and swelling process in acetone. (c) Experiments and modeling results of the bending curvature of the printed sample after desolvation process and swelling process.

4.3.2 *Theoretical model for the desolvation and swelling behavior*

4.3.2.1 The effect of grayscale on light intensity

We measured the light intensity of the projected light pattern with different grayscale. Figure 4.3(a) shows the results of the measurements. We found that the correlation between the light intensity I and grayscale value gr can be well fitted by the Gaussian function.

$$I = \mathrm{I}_M \exp(-(\frac{g_r - C_1}{C_2})^2), g_r \in [0,255] \tag{4-2}$$

where IM, C1, C2 are fitting parameters. For our projector, I_M=18.59 mW/cm2, C_1=269, C_2=118.9.

4.3.2.2 The conversion kinetics of the material by different light intensity

The chemical reaction process can be described as the conversion of the functional groups to polymer structure. The degree of conversion (DoC) is a good estimation of the reaction extent[115]. Vitale et al. [123] developed a simple model to describe the reaction kinetics. Here we use this model to calculate the evolution of the DoC. The light intensity attenuation across the thickness direction of the sample can be described by the Beer−Lambert law[185]:

$$\frac{\partial I(z,t)}{\partial z} = -a(z,t)I(z,t) \tag{4-3}$$

I is the light intensity, *z* is the coordinate of the material in the thickness direction, *a* is the attenuation coefficient, and *t* is irradiation time. Here we take the origin of z-axis at the printing stage. If the attenuation coefficient doesn't change during the photocuring process, then the light intensity at position *z* can be calculated by integral of Eq. (4-3)*:*

$$I(z,t) = I_0 \exp(-a(z_h - z)) \tag{4-4}$$

where I_0 is the light intensity at the outside surface of the liquid resin and z_h is the distance between the resin surface and the origin of z-axis. We consider the 3D printing process as the discrete light radiations and assume that the layer thickness of each printing layer is *h*. During the first exposure, the light intensity distribution in the first layer is:

$$I_1(z,t) = I_0 \exp(-a(h-z)) \tag{4-5}$$

where I_1 is the intensity of the first exposure. After each layer is printed, the printing stage will be lowered *h* distance for next layer. Therefore the distance between the cured material in the first layer and the current resin outside surface has changed. During the n^{th} layer printing process, the light intensity distribution inside the first layer is:

$$I_n(z,t) = I_0 \exp(-a(nh-z)) \tag{4-6}$$

The conversion rate is taken to be proportional to both intensity and the amount of unreacted materials [186]:

$$\frac{\partial p(z,t)}{\partial t} = K[1-p(z,t)]I(z,t) \tag{4-7}$$

where *K* is the photochemical reaction rate. Here in this model, the conversion is normalized by the maximum conversion of the cured polymer. We determined that the maximum conversion for our material is around 0.78.

The 3D printing is a layer-by-layer curing process and the light can penetrate several layers. Therefore each layer will not only subject to the first direct curing exposure but also the penetrated light exposure from succeeding printing layers. In the theoretical

modeling, we considered the effect of the penetrated light exposure. By solving Eq. (4-7), we can get the conversion of the material during nth light radiation:

$$p_n = 1 + (p_{f,n-1} - 1)\exp(-KI_n(z,t)t) \tag{4-8}$$

where $p_{f,n-1}$ is the final conversion after (n-1)th light radiation and $p_{f,0}$=0. If the printing time of each layer is Δt, we can calculate the conversion of the material after nth light radiation by Eq. (4-8):

$$\begin{aligned} p_n(z) &= 1 - \exp[-KI_1(z)\Delta t - KI_2(z)\Delta t \cdots\cdots - KI_n(z)\Delta t] \\ &= 1 - \exp[-K\sum_{m=1}^{n} I_m(z)\Delta t] \\ &= 1 - \exp[-KD(z,n)] \end{aligned} \tag{4-9}$$

From Eq. (4-9) we can see that the total conversion is the function of the total light dose $D(z,n) = \sum_{m=1}^{n} I_m(z)\Delta t$.

According to Vitale's method [187], the reaction constants K, a can be determined by measuring the position of the photocuring front at different curing times. The material needs to be cured to the critical conversion p_c to be a solid front. The curing depth $\tilde{z}$ or the position of the curing front can be calculated by [187]:

$$\tilde{z} = \frac{\ln[\dfrac{KI_0 t}{-\ln(1-p_c)}]}{a} \tag{4-10}$$

To determine the reaction constants K and a, Eq. (4-10) is used. We built a reaction cell by using two glass slides. Two glass slides were clamped together by two binder clips and two shim sheets with a thickness of 0.6 mm were put in between two glass slides to make space for the liquid resin. Liquid resin was injected into the reaction cell,

and then the rectangle pattern was projected using the UV projector to the surface of the curing cell for different curing times. After cured, the thickness of the samples with different curing times is measured. Then we obtain the relation between the curing time and curing front position. The value of p_c in Eq. (4-10) was measured to be around 0.15 by attenuated total reflection (ATR) FT-IR spectrum. By fitting the curing depth curve in Figure 4.3(b), the parameters K and a are determined: K = 0.01716 $cm^2mW^{-1}s^{-1}$, a = 7.866 mm^{-1}.

Using the determined reaction kinetics parameters, we can calculate the correlation between DoC and total light dose using Eq. (4-9). The calculation result is shown in Figure 4.3(c).

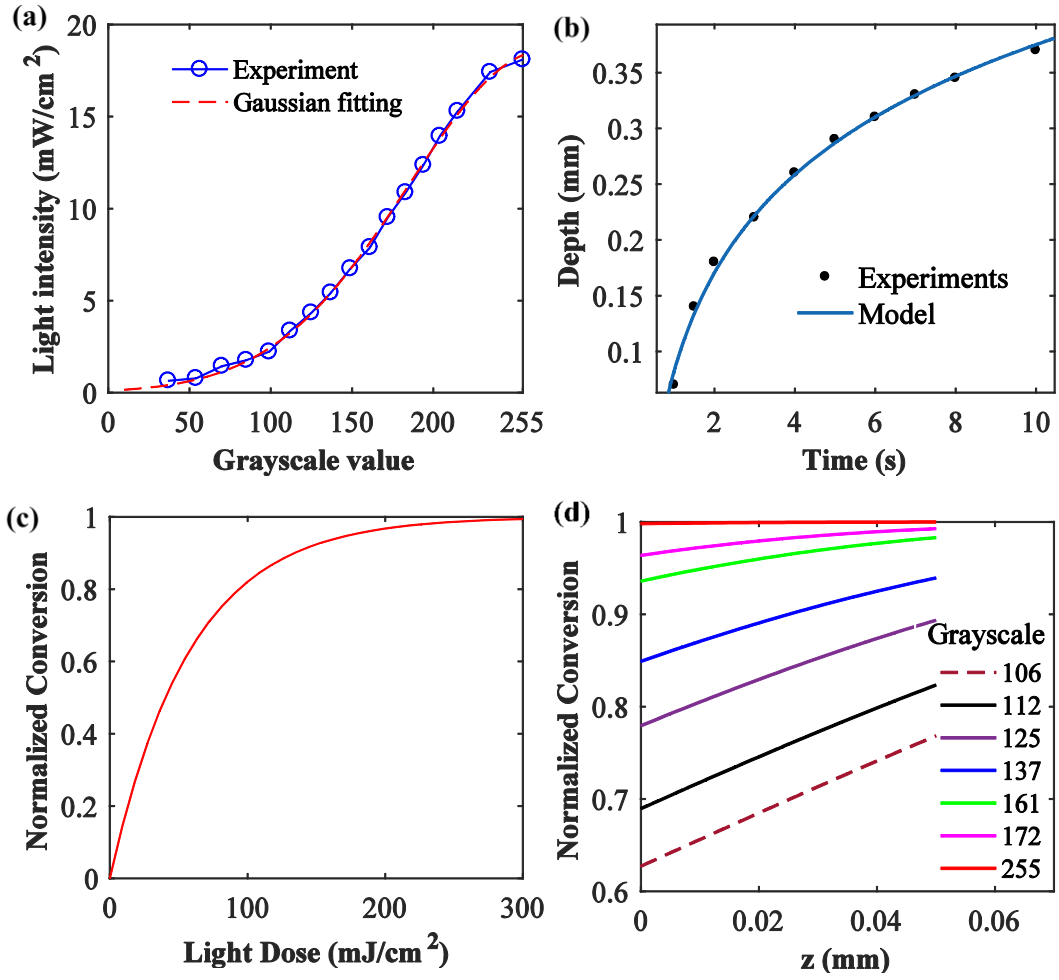

Figure 4.3 The effect of grayscale on light intensity. (a)The curing depth as a function of curing time. (b) Correlation between light dose and the DoC. (c) The conversion as a function of light dose. (d) The conversion of printed material by different grayscale light.

4.3.2.3 Grayscale effect on conversion

The grayscale value influences the light intensity. The final conversion of material under different light intensity can be calculated by Eq. (4-9) and it depends on the total light dose. Figure 4.3(d) shows the normalized conversion in one layer of the printed material by different grayscale. With the increase of the grayscale value, the conversion

increases. Therefore it can be utilized to control the crosslink density or cure conversion distribution in the printed material.

4.3.2.4 Material properties evolution

With the increase of the DoC, the modulus of the material increases. Previous research showed the modulus evolution during photocuring can be described as an exponential function of DoC [9,132,133]. Here we use the following equation to describe the modulus evolution:

$$E(p) = E_0 \exp(b(p - p_c)) \tag{4-11}$$

where E is Young's Modulus of the cured material, p_c is DoC at the gel point, E_0 and b are the fitting parameters respectively. The results are shown in Figure 4.2(a).

4.3.2.5 Desolvation induced shrinkage and swelling expansion in acetone

After desolvation in the water solution, the loss of the small oligomers induces the volume shrinkage of the printed material. And the volume shrinkage decreases as the DoC increases. The volume shrinkage during the desolvation is a linear function of the DoC. That is:

$$\alpha_d = \frac{V_d}{V_0} = \frac{m_d}{m_0} = c + bp \tag{4-12}$$

where V_0, V_d are the volume of the cured material after printing and desolvation respectively, m_0, m_d are the mass of the cured material after printing and desolvation respectively, c and b are fitting parameters for the linear relationship. Figure 4.2(b) shows the experimental results and fitting results. And the values of two parameters are: c= 0.7194, b= 0.2994.

If we need to let the deformed structure recover back its shape, we can immerse the structure into swelling medium acetone. After absorbing the small acetone molecules, the sample after desolvation will swell. The volume ratio of the cured sample can be calculated as:

$$\alpha_s = \frac{V_s}{V_d} = \frac{m_d / \rho_M + (m_s - m_d) / \rho_{acetone}}{m_d / \rho_M} \tag{4-13}$$

where V_d, V_s are the volume of the cured material after desolvation and swelling respectively, m_d and m_s are the mass of the cured material after desolvation and swelling respectively, ρ_M and $\rho_{acetone}$ are the density of the crosslinked network and acetone. To model the relation between the swelling ratio and the conversion, an empiric model is used.

$$\alpha_s = \frac{1}{\alpha_0 p^{\phi}} \tag{4-14}$$

where α_0, ϕ are fitting parameters. For our material, α_0 =0.89 and ϕ= 0.3404. The fitting results are also shown in Figure 4.2(b).

4.3.2.6 Mechanics of the desolvation and recovery process

The deformation of the sample after desolvation and recovery process are simulated using finite element analysis (FEA). The total deformation gradient $\mathbf{F}$ can be decomposed into elastic deformation part $\mathbf{F}^e$ and unconstrained volume change deformation $\mathbf{F}^V$.

$$\mathbf{F} = \mathbf{F}^e \mathbf{F}^V \tag{4-15}$$

In the desolvation process, the volume change deformation gradient is $\mathbf{F}^V = \alpha_d^{1/3}\mathbf{I}$. In the swelling recovery process, the volume change deformation gradient is $\mathbf{F}^V = \alpha_s^{1/3}\alpha_d^{1/3}\mathbf{I}$.

The stress-strain behavior of the polymeric material can be modeled using the Neo-Hookean model. The Cauchy stress can be calculated as:

$$\boldsymbol{\sigma} = \frac{1}{J}[(\lambda \ln J^e - \mu)\mathbf{I} + \mu\mathbf{b}], \mathbf{b} = \mathbf{F}^e\mathbf{F}^{eT} \tag{4-16}$$

where Lam$\hat{e}$s first parameter $\lambda = \frac{3K(3K-E)}{9K-E}$, shear modulus $\mu = \frac{3K-E}{6K}$ and J is the determinant of the deformation gradient.

The finite deformation model was implemented as a user material subroutine (UMAT) in the finite element analysis (FEA) software ABAQUS (Simulia, Providence, RI). The DoC of material inside each layer is calculated using Eq. (4-9). Due to the light intensity difference, the DoC will be different in different part, which will influence the volume shrinkage and swelling ratio.

Using these characterized material properties and theoretical model, we conducted FEA simulations to predict the bending curvature of the printed samples after desolvation and swelling. The comparison between experiments and FEA simulations are plotted in Figure 4.2(c). We can see that the model can capture the desolvation induced bending and swelling induced recovery behavior of the printed strip with gray scale light pattern.

4.3.3 *Reversible pattern transformation*

Applying the grayscale printing method and theoretical model, we designed and created reversible pattern transformation. Figure 4.4 shows three examples of the pattern transformation. For these patterns, we used the same grayscale picture for every printing

layer and they are shown in the first column of Figure 4.4. Each layer had a thickness of 50 μm and 60 layers were printed. In Figure 4.4(a) we demonstrated a printed square that transforms between the square and the parallelogram shape. The gray scale pattern used is also shown in Figure 4.4(a). After printing and being washed in water solution, the less cross-linked part under the gray portion of the picture shrank and pushed the corner to increase or decrease the angle, leading the square to transform into a parallelogram. The parallelogram structure can be recovered to the square shape by swelling in acetone for 7min. And if we take it out of acetone and let it dry in the air for about 30min, the structure can transform to the parallelogram shape. The Previous research [188] on this kind of transformation required complex programming steps such as heating, mechanical loading and unloading process and the transformation was usually one-way. Here our method provides a simple way to achieve reversible pattern transformation. Pattern transformation of periodic lattice structure by buckling is of great interest[189,190] in the application of aerospace engineering [191] and energy absorption and has been widely investigated. Using our printing method, we created the square lattice structure as an example shown in Figure 4.4(b) and the structure can transform to the buckled shape (Figure 4.4(b)) after desolvated. In addition, a circle to pentagon structure was created and shown in Figure 4.4(c). The recovery time in acetone for structures in Figure 4.4(b) and Figure 4.4(c) is 10 min and 3.5min respectively, and drying time in air is 40min and 20 min. We also used FEA simulation to simulate the shape transformation behavior. And the simulation details and result are included in the Supplementary Material.

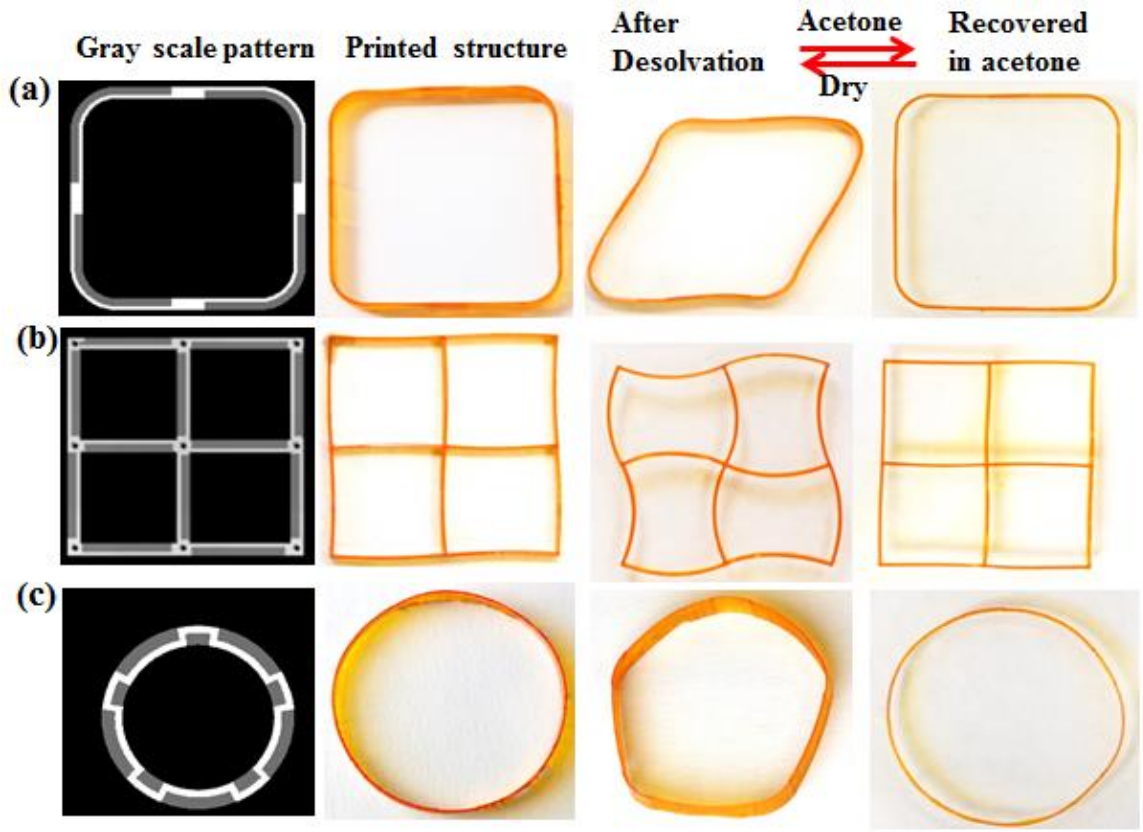

Figure 4.4 Reversible pattern transformation created by gray level 3D printing. The dimension and grayscale value of the pattern can be found in the Supplementary Material.

4.3.4 *Applications of the grayscale printing method - smart structures*

Active structures that can change their shape or function in response to external stimuli are highly desirable in aerospace engineering [192,193], medical devices [194,195] and flexible electronics [196,197]. Recently 3D printing has been used to design and fabricate active structures, which is also termed as 4D printing [80,82,178,198,199]. Hereby applying the grayscale printing, we demonstrated that our approach can be easily used as a 4D printing method.

4.3.4.1 Self- expanding /shrinking structure

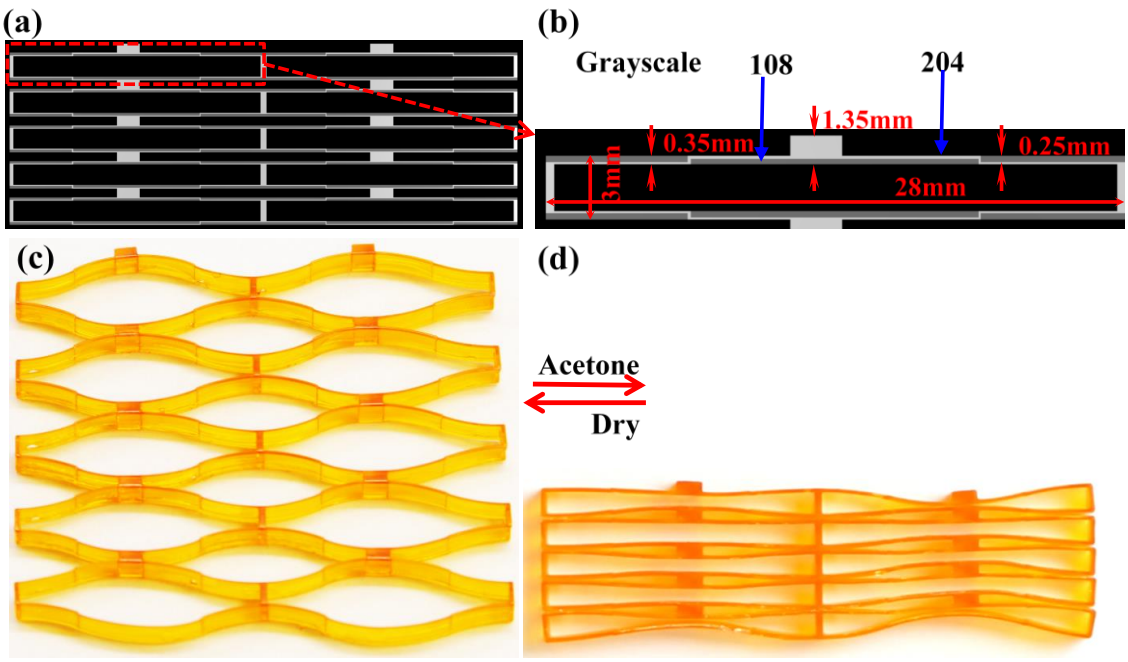

Figure 4.5 Self-expansion/shrinkage structure. (a) The printing pattern with different light intensity in each part. (b)The amplified figure to show the gray scale distribution. (c) The deformed structure after desolvation. (d) The structure after swelling process.

Self-expanding/shrinking structures are useful in the light actuator [200] and endovascular stent applications [201]. Here we showed a self-expanding/shrinking structure created by the grayscale 4D printing method. The design of the structure is shown in Figure 4.5(a) and the sliced grayscale figure is shown in Figure 4.5(b). After being washed in the water solution, the unit structure bent due to the shrinkage deformation induced by desolvation, which caused the unit structure to increase its dimension in the bending direction. The printed structure (Figure 4.5(c)) could expand to two times of its original shape in the vertical direction as shown in Figure 4.5(d). The recovery time in acetone and drying time in air for this transformation is about 6min and 25 min respectively. In addition, by combining four in-plane self-expanding units, we designed a 3D self-expanding/shrinking structure shown in Figure 4.6(a). The 4 side faces of the structure have the same grayscale distribution and the amplified diagram of the grayscale

distribution is shown in Figure 4.6(b). After desolvation process, the printed structure (Figure 4.6(c)) units expand in their own designed axial directions which results in expansion of whole structure. If we immerse the expanded structure into the acetone, the structure can shrink to recover its shape shown in Figure 4.6(d). The recovery time in acetone and drying time in air for the transformation between Figure 4.6(d) and Figure 4.6(e) is about 4min and 8 min respectively. Two videos (Movie S2 and Movie S3, Supplementary Material) showing the transformation of the structures in Figure 4 and Figure 5 can be found in the Supplementary Material.

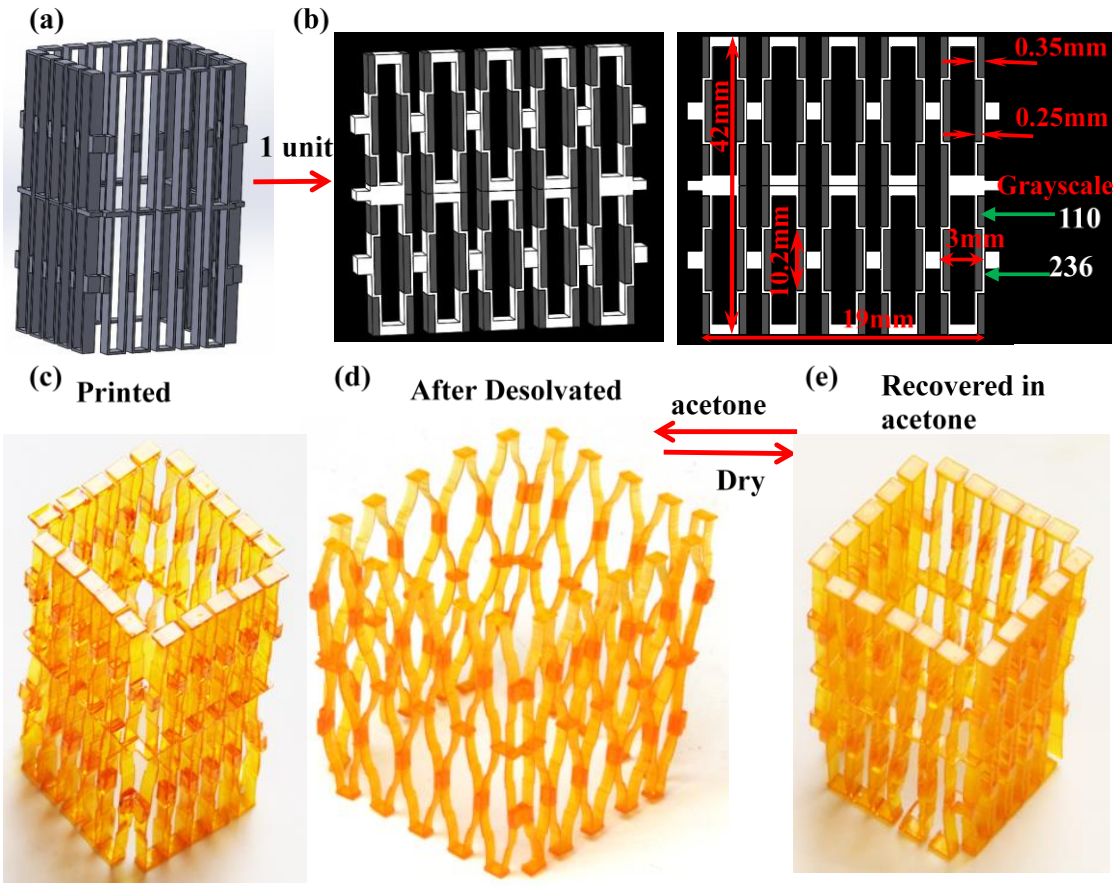

Figure 4.6 3D Self-expansion/shrinkage structure. (a) The actual design of the structure. (b) 1 unit cell of the structure with different gray scale level at the different location. The thickness of the unit cell is 2mm. (c) The printed structure. (d) The expanded structure after desolvation. (e) The recovered structure.

4.3.4.2 Transformation between normal and auxetic structures

Auxetic structure [202,203] which has negative Poisson's ratio, is an important type of metamaterials. Employing the grayscale printing method, we created metamaterials which can reversibly change between the normal material and auxetic metamaterial. The original design of the structure is shown in Figure 4.7(a). The basic structure was a hollow rectangular parallelepiped while the four side surfaces were represented by the 'X' shape structure. After printing the structure shown in Figure 4.7(c) showed normal material property (positive Poisson's ratio) under the compression test (Figure 4.7(d)). It should be noted that due to the buckling instability, it is possible that the structure can buckle towards the inner direction in theory. But if the uncured monomers were washed out from the low light intensity part, the desolvation induced bending caused the 'X' shape bending slightly towards the center of the rectangular parallelepiped (Figure 4.7(c)) and the auxetic metamaterial was produced. Then when we compressed the structure from the top surface (Figure 4.7(e)), its cross-section shrunk and showed the negative Poisson's ratio effect instead of expanding as the normal material.

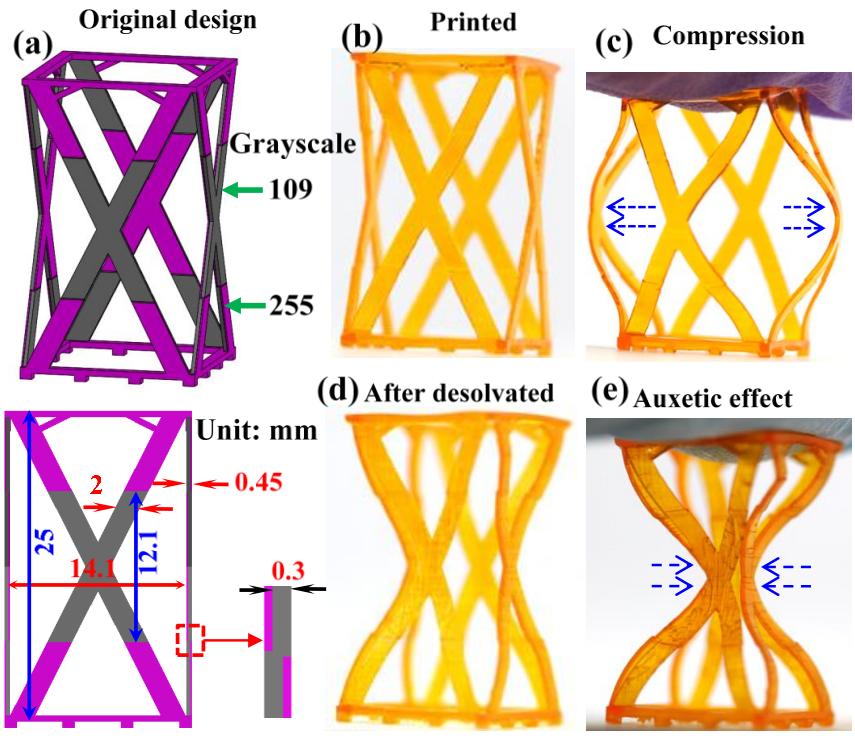

Figure 4.7 The transformation between normal and auxetic structures. (a)The design concept of the auxetic structure. The purple color represents the white color in grayscale. (b)The printed structure. (c)The deformed structure after desolvation. (d) The deformation of the printed structure without desolvation process under compression. (e) The auxetic effect of the structure after desolvation process.

4.3.4.3 Mimic the nature - blossom of a flower

Active structures have been widely used to mimic the behavior of different lives in nature [198,204-206]. Here we can also apply the method to create a flower like structure to mimic the blossom behavior of flowers. The flower had 3 layers of petal and different initial curvature (Figure 4.8(a)). The darker grayscale patterns redesigned on the outside surface of each petal. After desolvation process, the printed compact flower in Figure 4.8(b) would turn to a blossomed flower shown in Figure 4.8(c) due to the shrinkage deformation of the outside layer of each petal. When we put the blossomed flower into acetone, the darker grayscale part with low crosslink density absorbed small acetone molecules and swelled, which resulted in the recovery of the flower from the blossom to

the unblossomed one (Figure 4.8(d)). When we removed it from acetone, the blossoming process happened again due to the volatilization of acetone. The recovery time in acetone and drying time in air for the transformation are about 2 min and 18 min respectively. Movie S4 in the Supplementary Material shows the transformation of this structure.

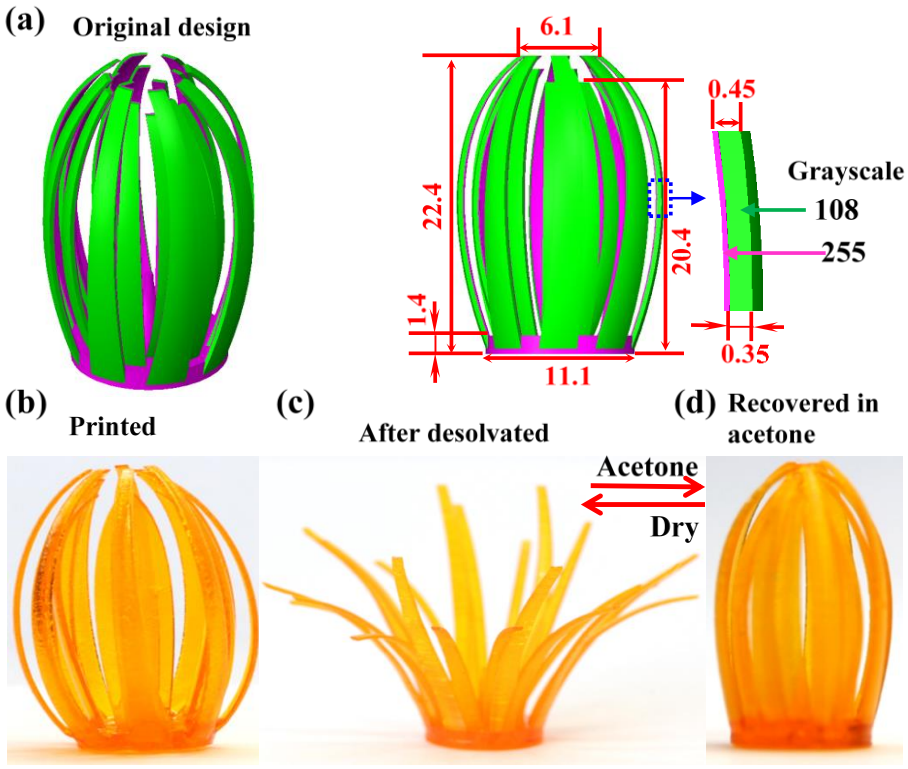

Figure 4.8 Blossom of a printed flower. (a)The design concept of the flower. The purple color represents the white color in grayscale 255. Green color represents a gray color with grayscale 108. The dimensions are in mm unit. (b)The printed structure. (c)The blossomed flower after desolvation. (d) The recovered flower after swelling in acetone.

4.4 Conclusions

A grayscale 4D printing method was proposed to create active structures. The grayscale pattern was used to control the light intensity distribution of the UV projector of the DLP 3D printer, thus different crosslink density could be created in the cured parts. After washing out the uncured oligomers inside the loosely cross-linked network,

bending deformation could be induced due to the shrinkage deformation of the loosely cross-linked part. The bending deformation was reversible when the printed structure absorbed acetone and swelled. Using this method, we designed and created RSC structures such as reversible pattern transformation, self-expanding/shrinking structure, auxetic metamaterial, a structure mimicking the blossom of a flower. The grayscale 4D printing method thus provides a simple and economical way to create active structures and has the great potential in the application of composite materials, soft robotics, and endovascular stent.

4.5 Supplementary Information

4.5.1 *Simulation of the pattern transformation*

Based on the theoretical model, we did FEA simulations for the designed reversible transformation pattern. Figure 4.9 shows the results of the shape of the designed pattern in Figure 4.4 in the main text after desolvation and recovered in acetone. We can see that the FEA simulation can predict the shape change well. It should be noted that the swelling deformation of the material after desolvation can be very large if it is immersed in the acetone for a long time. Therefore it can change to another swelled pattern after recovered the original shape.

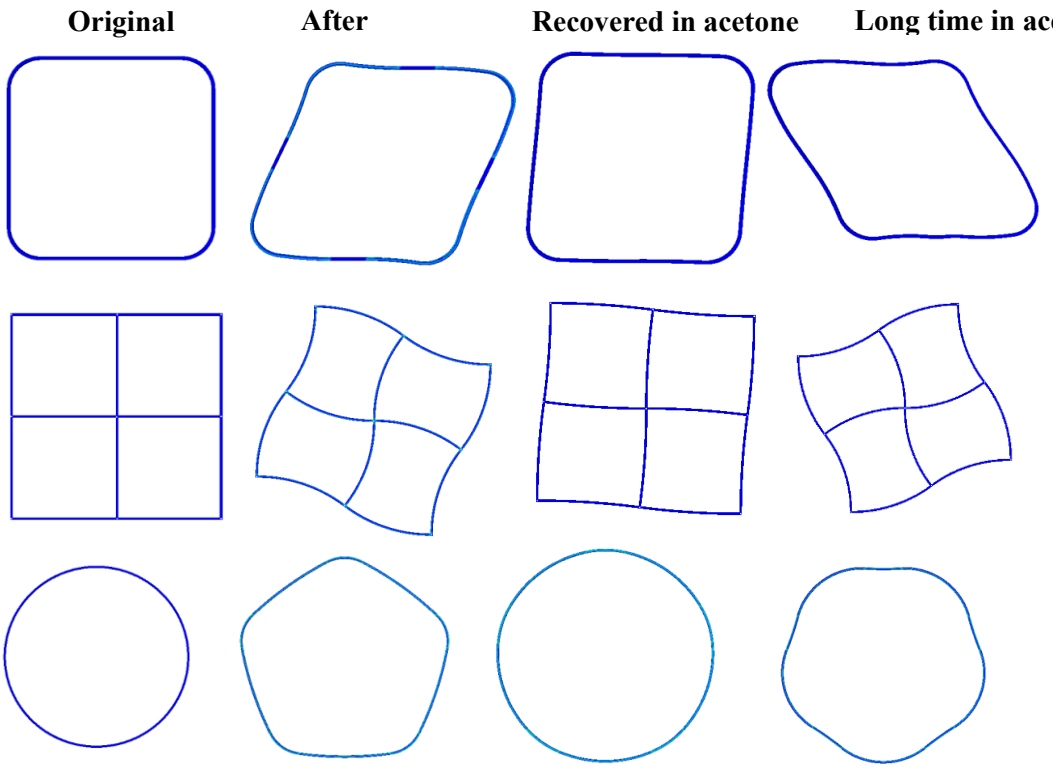

Figure 4.9 FEM simulation of reversible pattern transformation created by gray level 3D printing.

4.5.2 *Design dimensions and grayscale of the printed structure*

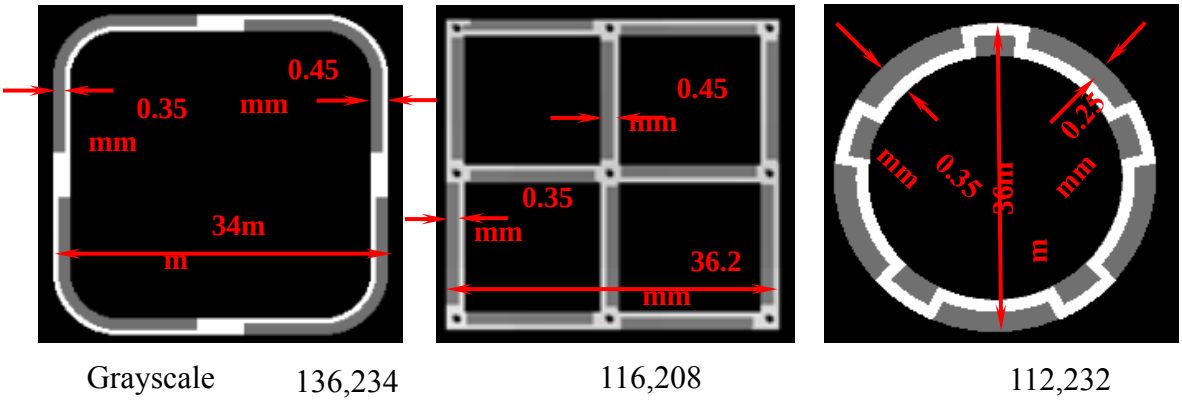

Figure 4.10 Design dimensions of the printed structure in Figure 4.3.

4.5.3 *The grayscale 3D printer setup*

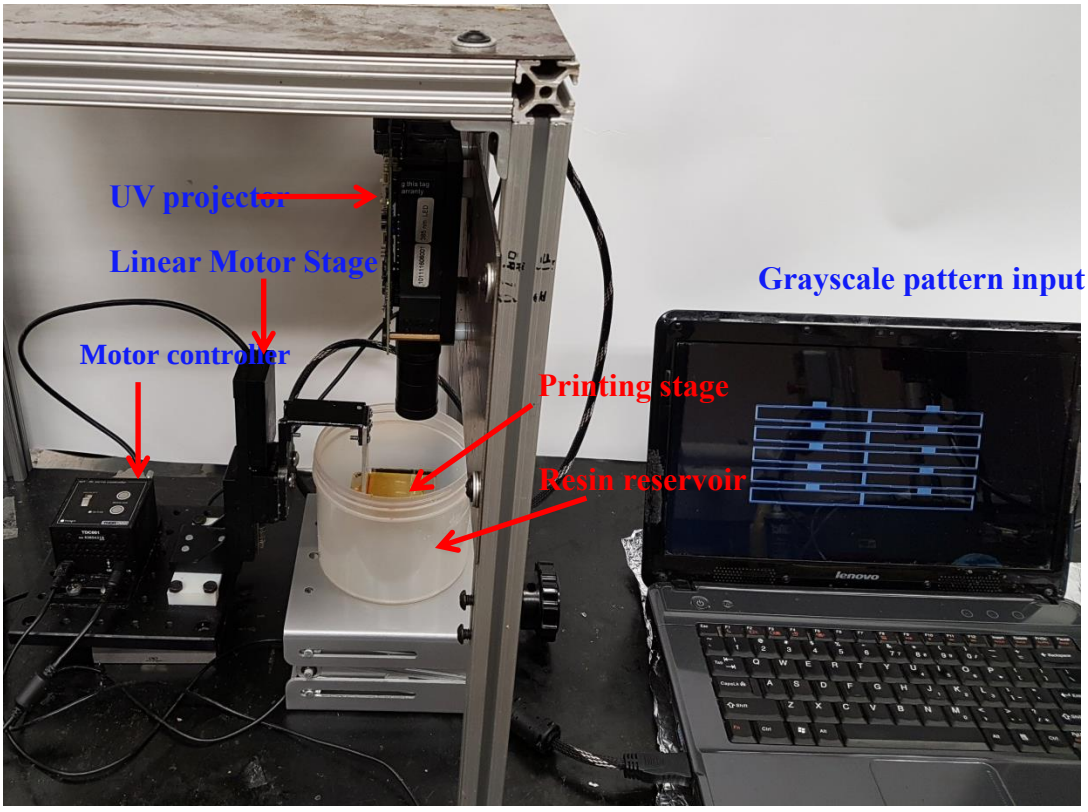

Figure 4.11 The setup of the DLP 3D printer.

CHAPTER 5. OVERALL CONCLUSIONS AND FUTURE WORK

This dissertation focuses on the constitutive modeling of photopolymerization and its applications to 3D and 4D printing. The evolution of mechanical properties of photopolymer during the photocuring process was investigated using theoretical modeling and experimentation. The photopolymerization chemical reaction kinetics was modeled using the first order reaction differential equations. The polymerization propagation rate and the termination rate were described using the diffusion controlled model. The DoC of functional group was used as the internal variable to describe the curing system. The T_g and the volume shrinkage evolution were linked with the DoC. A phase evolution model was used to decouple the mechanical deformation and material evolution. This constitutive model was able to capture the complex curing-mechanical loading coupling process. In addition, the internal stress of a thick sample caused by the volume shrinkage during photopolymerization was investigated. The variation of the internal stress in the thick sample during the photopolymerization was determined using the FEM simulation. This constitutive model was extended to investigate the DLP 3D printing process. To reduce the computational complexity, the theoretical model is simplified. Then the theoretic model is applied to the FEM simulation to simulate the layer-by-layer DLP 3D printing process. The printing distortions caused by the volume shrinkage of the typical DLP 3D printing structures were investigated by the FEM simulations. The comparison between the experiments and simulations indicates that the theoretical model can capture the distortion behavior of the printed structure. And by utilizing the FEM simulation tool we can optimize the printing parameters to reduce the

printing distortion. A grayscale 4D printing method was proposed to create active structures. We used the grayscale pattern to control the light intensity distribution of the UV projector of the DLP 3D printer, thus different crosslink density could be created in the cured parts. After washing out the uncured oligomers inside the loosely cross-linked network, bending deformation could be induced due to the shrinkage deformation of the loosely cross-linked part. The bending deformation was reversible when the printed structure absorbed acetone and swelled. Using this method, we designed and created a variety of RSC structures. A theoretical model was also proposed to investigate the material property and RSC of the printed RSC structures. The grayscale 4D printing method provides a simple and economical way to create active 3D structures. Compared to previous research on photopolymerization mechanics model, the model in this dissertation considers the detailed material property evolution process, the non-linear viscoelastic property of the material, and the coupling of the material property evolution and mechanical deformation. Therefore it can provide better understanding of the complex material property evolution and mechanical deformation coupling process.

The research in this dissertation can be further devolved in the following aspects.

1. The post-curing effect of the partially photocured material. For the applications of active structures created by the photopolymerization internal stress, the material could be further cured by ambient light although the reaction rate is relatively slow and the shape of the bent structure may not be stable. In addition, the polymer materials usually have aging effect. The material property will change over aging time. Those can influence the performance of the active structures. A detailed investigation on the influence of the low intensity ambient light and on the material property of the partially cured material will be helpful in the design of the active structures.

2. Building compensation method for the shape distortion of the 3D printed structure. Although we already used the FEM simulations to optimize the printing parameters to reduce the shape distortion of the 3D printed structure, the shape distortion cannot be fully eliminated. Another way to reduce the shape distortion is making compensation before the actual printing. We can revise the designed shape of the structure to compensate the distortion by using the FEM simulation results. Future work can be done to find algorithm for the compensation method.

3. Reduce the number of parameters of the photopolymerization and implement the full model developed in the second chapter to the 3D printing simulation. We can reduce the temperature range of the time-temperature-conversion superposition to reduce the number of parameters. And then the computational complexity and resource can be reduced and the full model can be implemented to better reflect the material property evolution during 3D printing.

REFERENCES

1 Chen, M., Zhong, M. & Johnson, J. A. Light-Controlled Radical Polymerization: Mechanisms, Methods, and Applications. *Chem Rev* **116**, 10167-10211, (2016).

2 Kaur, M. & Srivastava, A. K. Photopolymerization: A Review. *Journal of Macromolecular Science, Part C: Polymer Reviews* **42**, 481-512, (2002).

3 Andrzejewska, E. Photopolymerization kinetics of multifunctional monomers. *Progress in Polymer Science* **26**, 605-665, (2001).

4 Lee, H. & Fang, N. X. Micro 3D Printing Using a Digital Projector and its Application in the Study of Soft Materials Mechanics. e4457, (2012).

5 Check, C., Chartoff, R. & Chang, S. Inkjet printing of 3D nano-composites formed by photopolymerization of an acrylate monomer. *Reactive and Functional Polymers* **97**, 116-122, (2015).

6 Bernhard, M., Rosen, D. W. & Stucker, B. Additive Manufacturing Technologies – Rapid Prototyping to Direct Digital Manufacturing. *Assembly Automation* **32**, null, (2012).

7 Nguyen, K. T. & West, J. L. Photopolymerizable hydrogels for tissue engineering applications. *Biomaterials* **23**, 4307-4314, (2002).

8 Han, D., Lu, Z., Chester, S. A. & Lee, H. Micro 3D Printing of a Temperature-Responsive Hydrogel Using Projection Micro-Stereolithography. *Sci Rep* **8**, 1963, (2018).

9 Zhao, Z., Wu, J., Mu, X., Chen, H., Qi, H. J. & Fang, D. Desolvation Induced Origami of Photocurable Polymers by Digit Light Processing. *Macromol Rapid Commun* **38**, 1600625, (2017).

10 Zhao, Z., Wu, J., Mu, X., Chen, H., Qi, H. J. & Fang, D. Origami by frontal photopolymerization. *Sci Adv* **3**, e1602326, (2017).

11 Shankar Limaye, A. & Rosen, D. W. Compensation zone approach to avoid print‐through errors in mask projection stereolithography builds. *Rapid Prototyping Journal* **12**, 283-291, (2006).

12 Jariwala, A. S., Ding, F., Zhao, X. Y. & Rosen, D. W. A Process Planning Method for Thin Film Mask Projection Micro-Stereolithography. *Asme International Design Engineering Technical Conferences and Computers and*

Information in Engineering Conference, Proceedings, Vol 2, Pts a and B, 685-694, (2010).

13 Sager, B. & Rosen, D. W. in *Stereolithography: Materials, Processes and Applications* (ed Paulo Jorge Bártolo) 183-207 (Springer US, 2011).

14 Zhao, X. & Rosen, D. W. Process Modeling and Advanced Control Methods for Exposure Controlled Projection Lithography in *2015 American Control Conference.*

15 Zhang, Y., Jariwala, A. & Rosen, D. W. Effects of Oxygen Inhibition and Post-Processing on Exposure Controlled Projection in *The Twenty-Ninth Annual International Solid Freeform Fabrication Symposium – An Additive Manufacturing Conference*

16 Krzysztof_Matyjaszewski & Thomas_P._Davis. HANDBOOK OF RADICAL POLYMERIZATION.

17 Decker, C. Kinetic study and new applications of UV radiation curing. *Macromol Rapid Comm* **23**, 1067-1093, (2002).

18 Matyjaszewski, K. & Spanswick, J. Controlled/living radical polymerization. *Materials Today* **8**, 26-33, (2005).

19 Huang, Q., Zhang, J., Sabbaghi, A. & Dasgupta, T. Optimal offline compensation of shape shrinkage for three-dimensional printing processes. *IIE Transactions* **47**, 431-441, (2014).

20 Yang, H.-J., Hwang, P.-J. & Lee, S.-H. A study on shrinkage compensation of the SLS process by using the Taguchi method. *International Journal of Machine Tools & Manufacture* **42**, 1203-1212, (2002).

21 Karalekas, D. & Aggelopoulos, A. Study of shrinkage strains in a stereolithography cured acrylic photopolymer resin. *Journal of Materials Processing Technology* **136**, 146-150, (2003).

22 Moeck, A., Bianchi, R., Petry, V., Weder, R. & Helsby, D. in *RadTech 2014 : RadTech UV&EB Technology & Conference 2014* (Chicago/Rosemont, IL, USA, 2014).

23 Watts, D. & Silikas, N. In Situ Photo-Polymerisation and Polymerisation-Shrinkage Phenomena. 123-154, (2005).

24 Wu, T. *Theoretical modeling and experimental characterization of stress and crack development in parts manufactured through large area maskless photopolymerization* Ph.D. thesis, Georgia Institute of Technology, (2014).

25 Wiedemann, B., Dusel, K. H. & Eschl, J. Investigation into the influence of material and process on part distortion. *Rapid Prototyping Journal* **1**, 17-22, (1995).

26 Lu, B., Xiao, P., Sun, M. & Nie, J. Reducing volume shrinkage by low-temperature photopolymerization. *Journal of Applied Polymer Science* **104**, 1126-1130, (2007).

27 Dewaele, M., Truffier-Boutry, D., Devaux, J. & Leloup, G. Volume contraction in photocured dental resins: the shrinkage-conversion relationship revisited. *Dent Mater* **22**, 359-365, (2006).

28 Atai, M. & Watts, D. C. A new kinetic model for the photopolymerization shrinkage-strain of dental composites and resin-monomers. *Dent Mater* **22**, 785-791, (2006).

29 Kiasat, M. *Curing Shrinkage and Residual Stresses in Viscoelastic Thermosetting Resins and Composites*, TU Delft, Delft University of Technology, (2000).

30 Liu, N., Liu, J., Lin, J., Davies, G., Jin, P. & Zhang, D. Model of curing shrinkage and kinetic parameters of an acrylate-based ultraviolet-embossing resist based on free volume theory. *Journal of Micro/Nanolithography, MEMS, and MOEMS* **12**, 023005, (2013).

31 Kowalczyk, P. & Gambin, W. Techniques of shrinkage stress reduction in dental restorations. *Int J Mater Form* **1**, 755-758, (2008).

32 Jian, Y., He, Y., Jiang, T., Li, C., Yang, W. & Nie, J. Polymerization shrinkage of (meth)acrylate determined by reflective laser beam scanning. *Journal of Polymer Science Part B: Polymer Physics* **50**, 923-928, (2012).

33 Stansbury, J. W., Trujillo-Lemon, M., Lu, H., Ding, X., Lin, Y. & Ge, J. Conversion-dependent shrinkage stress and strain in dental resins and composites. *Dent Mater* **21**, 56-67, (2005).

34 Petrovic, L. M. & Atanackovic, T. M. A model for shrinkage strain in photo polymerization of dental composites. *Dent Mater* **24**, 556-560, (2008).

35 Schneider, L. F., Cavalcante, L. M. & Silikas, N. Shrinkage Stresses Generated during Resin-Composite Applications: A Review. *J Dent Biomech* **2010**, (2010).

36 Odian, G. *Principles of polymerization*. Fourth Edition edn, (John Wiley & Sons, Inc., 2004).

37 Braun, D. Origins and Development of Initiation of Free Radical Polymerization Processes. *International Journal of Polymer Science* **2009**, 1-10, (2009).

38 Tehfe, M., Louradour, F., Lalevée, J. & Fouassier, J.-P. Photopolymerization Reactions: On the Way to a Green and Sustainable Chemistry. *Applied Sciences* **3**, 490-514, (2013).

39 Zheng, X., Lee, H., Weisgraber, T. H., Shusteff, M., DeOtte, J., Duoss, E. B., Kuntz, J. D., Biener, M. M., Ge, Q., Jackson, J. A., Kucheyev, S. O., Fang, N. X. & Spadaccini, C. M. Ultralight, ultrastiff mechanical metamaterials. *Science* **344**, 1373-1377, (2014).

40 Sager, B. & Rosen, D. W. Use of parameter estimation for stereolithography surface finish improvement. *Rapid Prototyping Journal* **14**, 213-220, (2008).

41 Jariwala, A. S., Bourell, D., Ding, F., Boddapati, A., Breedveld, V., Grover, M. A., Henderson, C. L. & Rosen, D. W. Modeling effects of oxygen inhibition in mask‐based stereolithography. *Rapid Prototyping Journal* **17**, 168-175, (2011).

42 Gibson, I., Rosen, D. W. & Stucker, B. *Additive Manufacturing Technologies*. (Springer Science, 2010).

43 Fuchs, Y., Soppera, O. & Haupt, K. Photopolymerization and photostructuring of molecularly imprinted polymers for sensor applications--a review. *Anal Chim Acta* **717**, 7-20, (2012).

44 Wohlers, T. & Caffrey, T. 3D printing and additive manufacturing state of the industry annual worldwide progresss report. (Wohlers Associates, Inc., 2014).

45 Wohlers, T. & Caffrey, T. 3D printing and additive manufacturing state of the industry annual worldwide progresss report. (Wohlers Associates, Inc., 2015).

46 Wohlers, T. & Caffrey, T. 3D printing and additive manufacturing state of the industry annual worldwide progresss report. (Wohlers Associates, Inc., 2016).

47 Burton, J. *A Primer on UV-Curable Inkjet Inks*, <http://www.signindustry.com/flatbed_UV/articles/2008-11-17-SGIA_Primer_on_UV-Curable_Inkjet_Inks.php3> (2008).

48 Ameya, S. L. & Rosen, D. W. Compensation zone approach to avoid print‐through errors in mask projection stereolithography builds. *Rapid Prototyping Journal* **12**, 283-291, (2006).

49 Zhang, Y. *EMPIRICAL PROCESS PLANNING FOR EXPOSRE CONTROLLED PROJECTION LITHOGRAPHY* Master of Science thesis, (2016).

50 Pan, Y. & Chen, Y. Meniscus process optimization for smooth surface fabrication in Stereolithography. *Additive Manufacturing* **12**, 321-333, (2016).

51 Sun, C., Fang, N., Wu, D. M. & Zhang, X. Projection micro-stereolithography using digital micro-mirror dynamic mask. *Sensors and Actuators A: Physical* **121**, 113-120, (2005).

52 Jariwala, A. S., Jones, H., Kwatra, A. & Rosen, D. W. PROCESS PLANNING METHOD FOR EXPOSURE CONTROLLED PROJECTION LITHOGRAPHY in *Proceedings of the 24th Solid Freeform Fabrication Symposium*.

53 Zhou, C. & Chen, Y. Additive manufacturing based on optimized mask video projection for improved accuracy and resolution. *Journal of Manufacturing Processes* **14**, 107-118, (2012).

54 Huang, Y. M. & Jiang, C. P. Curl distortion analysis during photopolymerisation of stereolithography using dynamic finite element method. *International Journal of Advanced Manufacturing Technology* **21**, 586-595, (2003).

55 Huang, Y. M. & Jiang, C. P. Numerical analysis of a mask type stereolithography process using a dynamic finite-element method. *International Journal of Advanced Manufacturing Technology* **21**, 649-655, (2003).

56 Wang, W. L., Cheah, C. M., Fuh, J. Y. H. & Lu, L. Influence of process parameters on stereolithography part shrinkage. *Materials & Design* **17**, 205-213, (1996).

57 Tibbits, S. *The emergence of "4D printing"*, <http://www.ted.com/talks/skylar_tibbits_the_emergence_of_4d_printing?language=en> (2013).

58 Ge, Q., Qi, H. J. & Dunn, M. L. Active materials by four-dimension printing. *Applied Physics Letters* **103**, 131901, (2013).

59 Zhang, Q., Yan, D., Zhang, K. & Hu, G. Pattern transformation of heat-shrinkable polymer by three-dimensional (3D) printing technique. *Sci Rep* **5**, 8936, (2015).

60 Yu, K., Ritchie, A., Mao, Y., Dunn, M. L. & Qi, H. J. Controlled Sequential Shape Changing Components by 3D Printing of Shape Memory Polymer Multimaterials. *Procedia IUTAM* **12**, 193-203, (2015).

61 Mao, Y., Yu, K., Isakov, M. S., Wu, J., Dunn, M. L. & Jerry Qi, H. Sequential Self-Folding Structures by 3D Printed Digital Shape Memory Polymers. *Sci Rep* **5**, 13616, (2015).

62 Liu, Y., Boyles, J. K., Genzer, J. & Dickey, M. D. Self-folding of polymer sheets using local light absorption. *Soft Matter* **8**, 1764-1769, (2012).

63 Xie, T. Recent advances in polymer shape memory. *Polymer* **52**, 4985-5000, (2011).

64 Zheng, X., Zhou, S., Li, X. & Weng, J. Shape memory properties of poly(D,L-lactide)/hydroxyapatite composites. *Biomaterials* **27**, 4288-4295, (2006).

65 Zhou, Y. & Huang, W. M. Shape Memory Effect in Polymeric Materials: Mechanisms and Optimization. *Procedia IUTAM* **12**, 83-92, (2015).

66 Liu, C., Qin, H. & Mather, P. T. Review of progress in shape-memory polymers. *Journal of Materials Chemistry* **17**, 1543, (2007).

67 Jiang, H. Y., Kelch, S. & Lendlein, A. Polymers Move in Response to Light. *Advanced Materials* **18**, 1471-1475, (2006).

68 Koerner, H., Price, G., Pearce, N. A., Alexander, M. & Vaia, R. A. Remotely actuated polymer nanocomposites--stress-recovery of carbon-nanotube-filled thermoplastic elastomers. *Nat Mater* **3**, 115-120, (2004).

69 Lendlein, A., Jiang, H., Junger, O. & Langer, R. Light-induced shape-memory polymers. *Nature* **434**, 879-882, (2005).

70 Xiao, Y., Zhou, S., Wang, L. & Gong, T. Electro-active shape memory properties of poly(epsilon-caprolactone)/functionalized multiwalled carbon nanotube nanocomposite. *ACS Appl Mater Interfaces* **2**, 3506-3514, (2010).

71 Luo, X. & Mather, P. T. Conductive shape memory nanocomposites for high speed electrical actuation. *Soft Matter* **6**, 2146, (2010).

72 Liu, Y., Lv, H., Lan, X., Leng, J. & Du, S. Review of electro-active shape-memory polymer composite. *Composites Science and Technology* **69**, 2064-2068, (2009).

73 Schmidt, A. M. Electromagnetic Activation of Shape Memory Polymer Networks Containing Magnetic Nanoparticles. *Macromol Rapid Comm* **27**, 1168-1172, (2006).

74 Mohr, R., Kratz, K., Weigel, T., Lucka-Gabor, M., Moneke, M. & Lendlein, A. Initiation of shape-memory effect by inductive heating of magnetic nanoparticles in thermoplastic polymers. *Proc Natl Acad Sci U S A* **103**, 3540-3545, (2006).

75 Buckley, P. R., McKinley, G. H., Wilson, T. S., Small, W., Benett, W. J., Bearinger, J. P., McElfresh, M. W. & Maitland, D. J. Inductively heated shape memory polymer for the magnetic actuation of medical devices. *IEEE Trans Biomed Eng* **53**, 2075-2083, (2006).

76 Leng, J., Lan, X., Liu, Y. & Du, S. Shape-memory polymers and their composites: Stimulus methods and applications. *Progress in Materials Science* **56**, 1077-1135, (2011).

77 Childers, E. P., Wang, M. O., Becker, M. L., Fisher, J. P. & Dean, D. 3D printing of resorbable poly(propylene fumarate) tissue engineering scaffolds. *MRS Bulletin* **40**, 119-126, (2015).

78 Mano, J. F. Stimuli-Responsive Polymeric Systems for Biomedical Applications. *Advanced Engineering Materials* **10**, 515-527, (2008).

79 Singh, M., Haverinen, H. M., Dhagat, P. & Jabbour, G. E. Inkjet printing-process and its applications. *Adv Mater* **22**, 673-685, (2010).

80 Wu, J., Yuan, C., Ding, Z., Isakov, M., Mao, Y., Wang, T., Dunn, M. L. & Qi, H. J. Multi-shape active composites by 3D printing of digital shape memory polymers. *Sci Rep* **6**, 24224, (2016).

81 Ge, Q., Dunn, C. K., Qi, H. J. & Dunn, M. L. Active origami by 4D printing. *Smart Materials and Structures* **23**, 094007, (2014).

82 Raviv, D., Zhao, W., McKnelly, C., Papadopoulou, A., Kadambi, A., Shi, B., Hirsch, S., Dikovsky, D., Zyracki, M., Olguin, C., Raskar, R. & Tibbits, S. Active printed materials for complex self-evolving deformations. *Sci Rep* **4**, 7422, (2014).

83 Bakarich, S. E., Gorkin, R., 3rd, Panhuis, M. I. & Spinks, G. M. 4D Printing with Mechanically Robust, Thermally Actuating Hydrogels. *Macromol Rapid Commun*, (2015).

84 Bugeda, G., Cervera, M., Lombera, G. & Onate, E. Numerical analysis of stereolithography processes using the finite element method. *Rapid Prototyping Journal* **1**, 13-23, (1995).

85 Carver, M. T., Dreyer, U., Knoesel, R., Candau, F. & Fitch, R. M. Kinetics of Photopolymerization of Acrylamide in Aot Reverse Micelles. *Journal of Polymer Science Part a-Polymer Chemistry* **27**, 2161-2177, (1989).

86 Ma, J., Mu, X., Bowman, C. N., Sun, Y., Dunn, M. L., Qi, H. J. & Fang, D. A photoviscoplastic model for photoactivated covalent adaptive networks. *Journal of the Mechanics and Physics of Solids* **70**, 84-103, (2014).

87 Scherzer, T. & Decker, U. Real-time FTIR–ATR spectroscopy to study the kinetics of ultrafast photopolymerization reactions induced by monochromatic UV light. *Vibrational Spectroscopy* **19**, 385-398, (1999).

88 Zhao, Z., Mu, X., Sowan, N., Pei, Y., Bowman, C. N., Jerry Qi, H. & Fang, D. Effects of oxygen on light activation in covalent adaptable network polymers. *Soft Matter* **11**, 6134-6144, (2015).

89 Kambly, K. *Characterization of curing kinetics and polymerization shrinkage in ceramic-loaded photocurable resins for large area maskless photopolymerization (LAMP)* M.S. thesis, Georgia Institute of Technology, (2009).

90 Agarwal, S. *In Situ Monitoring of UV-Curing Kinetics of Acrylate Coatings by Combined Ultrasound Reflectometry and Near-Infrared Spectroscopy* PhD thesis, Technische Universität Darmstadt, (2011).

91 Buback, M., Huckestein, B. & Russell, G. T. Modeling of Termination in Intermediate and High Conversion Free-Radical Polymerizations. *Macromolecular Chemistry and Physics* **195**, 539-554, (1994).

92 Dickey, M. D. & Willson, C. G. Kinetic parameters for step and flash imprint lithography photopolymerization. *AIChE Journal* **52**, 777-784, (2006).

93 Long, K. N., Scott, T. F., Jerry Qi, H., Bowman, C. N. & Dunn, M. L. Photomechanics of light-activated polymers. *Journal of the Mechanics and Physics of Solids* **57**, 1103-1121, (2009).

94 Lee, J. H., Prud'homme, R. K. & Aksaya1, I. A. Cure depth in photopolymerization: Experiments and theory. *Journal of Materials Research* **16**, 3536-3544, (2011).

95 Qin, J. G., Guo, W. P. & Zhang, Z. Modeling of the bulk free radical polymerization up to high conversion - three stage polymerization model. II. Number-average molecular weight and apparent initiator efficiency. *Polymer* **43**, 4859-4867, (2002).

96 Zhen, Y., Bogeng, L., Kun, C., Yuan, H. & Zu-ren, P. Modeling for the diffusion limitation of free radical polymerization. *Journal of Zhejiang University-SCIENCE A* **1**, 148- 156, (2000).

97 Gleeson, M. R. & Sheridan, J. T. Nonlocal photopolymerization kinetics including multiple termination mechanisms and dark reactions. Part I. Modeling. *J Opt Soc Am B* **26**, 1736-1745, (2009).

98 O'Shaughnessy, B. & Yu, J. Autoacceleration in free radical polymerization. *Phys Rev Lett* **73**, 1723-1726, (1994).

99 Van Gurp, M. & Palmen, J. Time-temperature superposition for polymeric blends. *Rheol. Bull* **67**, (1998).

100 Colby, R. & Rubinstein, M. Polymer physics. *New-York: Oxford University*, 274-281, (2003).

101 Simon, S. L., McKenna, G. B. & Sindt, O. Modeling the evolution of the dynamic mechanical properties of a commercial epoxy during cure after gelation. *Journal of Applied Polymer Science* **76**, 495-508, (2000).

102 Gillen, K. T. Effect of Cross-Links Which Occur during Continuous Chemical Stress-Relaxation. *Macromolecules* **21**, 442-446, (1988).

103 Negahban, M. & Wineman, A. S. Modeling the Mechanical Response of a Material Undergoing Continuous Isothermal Crystallization. *Int J Eng Sci* **30**, 953-962, (1992).

104 Rajagopal, K. R. & Wineman, A. S. A Constitutive Equation for Nonlinear Solids Which Undergo Deformation Induced Microstructural Changes. *Int J Plasticity* **8**, 385-395, (1992).

105 Rajagopal, K. R. & Srinivasa, A. R. Mechanics of the inelastic behavior of materials - Part 1, theoretical underpinnings. *Int J Plasticity* **14**, 945-967, (1998).

106 Srinivasa, A. R., Rajagopal, K. R. & Armstrong, R. W. A phenomenological model of twinning based on dual reference structures. *Acta Mater* **46**, 1235-1248, (1998).

107 Wineman, A. & Shaw, J. A correspondence principle for scission-induced stress relaxation in elastomeric components. *J Appl Mech-T Asme* **71**, 769-773, (2004).

108 Lakes, R. S. & Wineman, A. On Poisson's ratio in linearly viscoelastic solids. *J Elasticity* **85**, 45-63, (2006).

109 Long, K. N., Dunn, M. L. & Jerry Qi, H. Mechanics of soft active materials with phase evolution. *International Journal of Plasticity* **26**, 603-616, (2010).

110 Hossain, M., Possart, G. & Steinmann, P. A finite strain framework for the simulation of polymer curing. Part I: elasticity. *Comput Mech* **44**, 621-630, (2009).

111 Hossain, M. & Steinmann, P. Degree of cure-dependent modelling for polymer curing processes at small-strain. Part I: consistent reformulation. *Comput Mech* **53**, 777-787, (2013).

112 Westbrook, K. K., Parakh, V., Chung, T., Mather, P. T., Wan, L. C., Dunn, M. L. & Qi, H. J. Constitutive Modeling of Shape Memory Effects in Semicrystalline Polymers With Stretch Induced Crystallization. *Journal of Engineering Materials and Technology* **132**, 041010, (2010).

113 Ge, Q., Luo, X., Rodriguez, E. D., Zhang, X., Mather, P. T., Dunn, M. L. & Qi, H. J. Thermomechanical behavior of shape memory elastomeric composites. *Journal of the Mechanics and Physics of Solids* **60**, 67-83, (2012).

114 Ge, Q., Luo, X., Iversen, C. B., Nejad, H. B., Mather, P. T., Dunn, M. L. & Jerry Qi, H. A finite deformation thermomechanical constitutive model for triple shape polymeric composites based on dual thermal transitions. *International Journal of Solids and Structures* **51**, 2777-2790, (2014).

115 Wu, J. T., Zhao, Z., Hamel, C. M., Mu, X. M., Kuang, X., Guo, Z. Y. & Qi, H. J. Evolution of material properties during free radical photopolymerization. *Journal of the Mechanics and Physics of Solids* **112**, 25-49, (2018).

116 Dendukuri, D., Panda, P., Haghgooie, R., Kim, J. M., Hatton, T. A. & Doyle, P. S. Modeling of Oxygen-Inhibited Free Radical Photopolymerization in a PDMS Microfluidic Device. *Macromolecules* **41**, 8547-8556, (2008).

117 Mu, Q., Dunn, C. K., Wang, L., Dunn, M. L., Qi, H. J. & Wang, T. Thermal cure effects on electromechanical properties of conductive wires by direct ink write for 4D printing and soft machines. *Smart Materials and Structures* **26**, (2017).

118 Nawab, Y., Shahid, S., Boyard, N. & Jacquemin, F. Chemical shrinkage characterization techniques for thermoset resins and associated composites. *Journal of Materials Science* **48**, 5387-5409, (2013).

119 Yoshida, S., Takahata, Y., Horiuchi, S., Kurata, H. & Yamamoto, M. Numerical Model of Radical Photopolymerization Based on Interdiffusion. *International Journal of Polymer Science* **2014**, 1-8, (2014).

120 Goodner, M. D. & Bowman, C. N. Modeling primary radical termination and its effects on autoacceleration in photopolymerization kinetics. *Macromolecules* **32**, 6552-6559, (1999).

121 Davis, A. B. & Marshak, A. Photon propagation in heterogeneous optical media with spatial correlations: enhanced mean-free-paths and wider-than-exponential free-path distributions. *Journal of Quantitative Spectroscopy and Radiative Transfer* **84**, 3-34, (2004).

122 Long, K. N., Dunn, M. L., Scott, T. F. & Qi, H. J. Photo-Induced Creep of Network Polymers. *INTERNATIONAL JOURNAL OF STRUCTURAL CHANGES IN SOLIDS – Mechanics and Applications* **1**, 41-52, (2010).

123 Vitale, A., Hennessy, M. G., Matar, O. K. & Cabral, J. T. Interfacial Profile and Propagation of Frontal Photopolymerization Waves. *Macromolecules* **48**, 198-205, (2015).

124 Buback, M., Huckestein, B. & Russell, G. T. Modeling of termination in intermediate and high conversion free radical polymerizations. (1994).

125 Buback, M., Hesse, P., Hutchinson, R. A., Kasak, P., Lacik, I., Stach, M. & Utz, I. Kinetics and Modeling of Free-Radical Batch Polymerization of Nonionized Methacrylic Acid in Aqueous Solution. *Industrial & Engineering Chemistry Research* **47**, 8197-8204, (2008).

126 Buback, M. Free-Radical Polymerization up to High Conversion - a General Kinetic Treatment. *Makromolekulare Chemie-Macromolecular Chemistry and Physics* **191**, 1575-1587, (1990).

127 Dibenedetto, A. T. Prediction of the Glass-Transition Temperature of Polymers - a Model Based on the Principle of Corresponding States. *J Polym Sci Pol Phys* **25**, 1949-1969, (1987).

128 Nielsen, L. E. Cross-Linking–Effect on Physical Properties of Polymers. *Journal of Macromolecular Science, Part C: Polymer Reviews* **3**, 69-103, (1969).

129 Gan, S., Seferis, J. C. & Prime, R. B. A Viscoelastic Description of the Glass Transition-Conversion Relationship for Reactive Polymers. *J Therm Anal* **37**, 463-478, (1991).

130 Lion, A. & Hofer, P. On the phenomenological representation of curing phenomena in continuum mechanics. *Arch Mech* **59**, 59-89, (2007).

131 Hossain, M. & Steinmann, P. Continuum Physics of Materials with Time-Dependent Properties. *Advances in Applied Mechanics* **48**, 141-259, (2015).

132 O'Brien, D. J., Mather, P. T. & White, S. R. Viscoelastic Properties of an Epoxy Resin during Cure. *Journal of Composite Materials* **35**, 883-904, (2001).

133 Zarrelli, M., Skordos, A. A. & Partridge, I. K. Toward a constitutive model for cure-dependent modulus of a high temperature epoxy during the cure. *European Polymer Journal* **46**, 1705-1712, (2010).

134 Westbrook, K. K., Kao, P. H., Castro, F., Ding, Y. & Jerry Qi, H. A 3D finite deformation constitutive model for amorphous shape memory polymers: A multi-branch modeling approach for nonequilibrium relaxation processes. *Mechanics of Materials* **43**, 853-869, (2011).

135 Yu, K., Ge, Q. & Qi, H. J. Reduced time as a unified parameter determining fixity and free recovery of shape memory polymers. *Nat Commun* **5**, 3066, (2014).

136 Chester, S. A., Srivastava, V., Di Leo, C. V. & Anand, L. A Large-Deformation Theory for Thermally-Actuated Shape-Memory Polymers and Its Application. *Proceedings of the Asme International Mechanical Engineering Congress and Exposition (Imece 2010)* **9**, 677-683, (2012).

137 Losi, G. U. & Knauss, W. G. Free-Volume Theory and Nonlinear Thermoviscoelasticity. *Polym Eng Sci* **32**, 542-557, (1992).

138 Boyce, M. C., Parks, D. M. & Argon, A. S. Large inelastic deformation of glassy polymers. part I: rate dependent constitutive model. *Mechanics of Materials* **7**, 15-33, (1988).

139 Arruda, E. M. & Boyce, M. C. Evolution of plastic anisotropy in amorphous polymers during finite straining. *International Journal of Plasticity* **9**, 697-720, (1993).

140 Bergström, J. S. & Boyce, M. C. Constitutive modeling of the large strain time-dependent behavior of elastomers. *Journal of the Mechanics and Physics of Solids* **46**, 931-954, (1998).

141 Adolf, D. B., Chambers, R. S. & Caruthers, J. M. Extensive validation of a thermodynamically consistent, nonlinear viscoelastic model for glassy polymers. *Polymer* **45**, 4599-4621, (2004).

142 Arzoumanidis, G. A. & Liechti, K. M. Linear Viscoelastic Property Measurement and Its Significance for Some Nonlinear Viscoelasticity Models. *Mechanics of Time-Dependent Materials* **7**, 209-250, (2003).

143 Mao, Y., Robertson, J. M., Mu, X., Mather, P. T. & Jerry Qi, H. Thermoviscoplastic behaviors of anisotropic shape memory elastomeric composites for cold programmed non-affine shape change. *Journal of the Mechanics and Physics of Solids* **85**, 219-244, (2015).

144 Boyce, M. C., PARKS, D. M. & ARGON, A. S. Large inelastic deformation of glassy polymers. part I: rate dependent constitutive model. *Mechanics of Materials* **7**, 15-33, (1988).

145 Porter, R. S., Knox, J. P. & Johnson, J. F. On the Flow and Activation Energy of Branched Polyethylene Melts. *Transactions of the Society of Rheology* **12**, 409-419, (1968).

146 Diani, J., Gilormini, P., Frédy, C. & Rousseau, I. Predicting thermal shape memory of crosslinked polymer networks from linear viscoelasticity. *International Journal of Solids and Structures* **49**, 793-799, (2012).

147 Sherrod, P. Nonlinear Regression Analysis Program, NLREG Version 5.0. *Phillip H. Sherrod, Nashville, TN*, (2000).

148 Bourell, D., Jariwala, A. S., Ding, F., Boddapati, A., Breedveld, V., Grover, M. A., Henderson, C. L. & Rosen, D. W. Modeling effects of oxygen inhibition in mask‐based stereolithography. *Rapid Prototyping Journal* **17**, 168-175, (2011).

149 Altun-Ciftçioğlu, G. A., Ersoy-Meriçboyu, A. & Henderson, C. L. Simulation of models for multifunctional photopolymerization kinetics. *Polymer Engineering & Science* **54**, 1737-1746, (2014).

150 Zhang, A.-F., Du, X.-D., Lei, J.-H., Liu, Y. & Bi, Y. Determination of Polyethylene Glycol Monoester Acrylate and Polyethylene Glycol Diester Acrylate Using Reversed-Phase High-Performance Liquid Chromatography. *Analytical Letters* **43**, 858-866, (2010).

151 Huang, Y., Leu, M. C., Mazumder, J. & Donmez, A. Additive Manufacturing: Current State, Future Potential, Gaps and Needs, and Recommendations. *Journal of Manufacturing Science and Engineering* **137**, (2014).

152 Guo, N. & Leu, M. C. Additive manufacturing: technology, applications and research needs. *Frontiers of Mechanical Engineering* **8**, 215-243, (2013).

153 Yossef, M. & Chen, A. Applicability and Limitations of 3D Printing for Civil Structures in *Civil, Construction and Environmental Engineering Conference Presentations and Proceedings.*

154 Vatani, M., Barazandeh, F., Rahimi, A. & Sanati Nezhad, A. Distortion modeling of SL parts by classical lamination theory. *Rapid Prototyping Journal* **18**, 188-193, (2012).

155 Schmutzler, C., Zimmermann, A. & Zaeh, M. F. Compensating Warpage of 3D Printed Parts Using Free-form Deformation. *Procedia CIRP* **41**, 1017-1022, (2016).

156 Xu, Y., Imamura, M. & Nakagawa, T. MICRO-HARDNESS MEASUREMENT OF PHOTOPOLYMER IN STEREOLITHOGRAPHY. *Journal of Photopolymer Science and Technology* **10**, 181-186, (1997).

157 Jiang, C. P., Huang, Y. M. & Liu, C. H. Dynamic finite element analysis of photopolymerization in stereolithography. *Rapid Prototyping Journal* **12**, 173-180, (2006).

158 Yaghi, A. H., Tanner, D. W. J., Hyde, T. H., Becker, A. A. & Sun, W. Finite element thermal analysis of the fusion welding of a P92 steel pipe. *Mechanical Sciences* **3**, 33-42, (2012).

159 Simunovic, S., Nycz, A., Noakes, M. W., Chin, C. & Oancea, V. in *Metal Big Area Additive Manufacturing: Process Modeling and Validation* (Chicago, USA, 2017).

160 Michaleris, P. Modeling metal deposition in heat transfer analyses of additive manufacturing processes. *Finite Elements in Analysis and Design* **86**, 51-60, (2014).

161 Lundbäck, A. & Lindgren, L.-E. Modelling of metal deposition. *Finite Elements in Analysis and Design* **47**, 1169-1177, (2011).

162 Lindgren, L. E., Runnemalm, H. & Nasstrom, M. O. Simulation of multipass welding of a thick plate. *Int J Numer Meth Eng* **44**, 1301-1316, (1999).

163 Chiumenti, M., Cervera, M., Salmi, A., Agelet de Saracibar, C., Dialami, N. & Matsui, K. Finite element modeling of multi-pass welding and shaped metal deposition processes. *Computer Methods in Applied Mechanics and Engineering* **199**, 2343-2359, (2010).

164 Denlinger, E. R., Irwin, J. & Michaleris, P. Thermomechanical Modeling of Additive Manufacturing Large Parts. *Journal of Manufacturing Science and Engineering* **136**, (2014).

165 Tang, Y., Henderson, C. L., Muzzy, J. & Rosen, D. W. in *Proceedings of the 15th Solid Freeform Fabrication Symposium* (Austin, TX, USA,, 2004).

166 Tanaka, F., Morooka, M., Kishinami, T. & Narahara, H. in *The 8th International Conference on Rapid Prototyping* 87–92 (Tokyo, Japan, 2000).

167 TruongVo, T. N., Kennedy, R. M., Chen, H., Chen, A., Berndt, A., Agarwal, M., Zhu, L., Nakshatri, H., Wallace, J., Na, S., Yokota, H. & Ryu, J. E. Microfluidic channel for characterizing normal and breast cancer cells. *Journal of Micromechanics and Microengineering* **27**, (2017).

168 Dittrich, P. S. & Manz, A. Lab-on-a-chip: microfluidics in drug discovery. *Nature Reviews Drug Discovery* **5**, 210, (2006).

169 Tegenfeldt, J. O., Prinz, C., Cao, H., Huang, R. L., Austin, R. H., Chou, S. Y., Cox, E. C. & Sturm, J. C. Micro- and nanofluidics for DNA analysis. *Anal Bioanal Chem* **378**, 1678-1692, (2004).

170 Urrios, A., Parra-Cabrera, C., Bhattacharjee, N., Gonzalez-Suarez, A. M., Rigat-Brugarolas, L. G., Nallapatti, U., Samitier, J., DeForest, C. A., Posas, F., Garcia-Cordero, J. L. & Folch, A. 3D-printing of transparent bio-microfluidic devices in PEG-DA. *Lab Chip* **16**, 2287-2294, (2016).

171 Gong, H., Beauchamp, M., Perry, S., Woolley, A. T. & Nordin, G. P. Optical Approach to Resin Formulation for 3D Printed Microfluidics. *RSC Adv* **5**, 106621-106632, (2015).

172 Han, Y., Yeo, C. C. J., Chen, D., Wang, F., Chong, Y., Li, X., Jiao, X. & Wang, F. Nanowire enhanced dimensional accuracy in acrylate resin-based 3D printing. *New Journal of Chemistry* **41**, 8407-8412, (2017).

173 Yu, C., Duan, Z., Yuan, P., Li, Y., Su, Y., Zhang, X., Pan, Y., Dai, L. L., Nuzzo, R. G., Huang, Y., Jiang, H. & Rogers, J. A. Electronically programmable, reversible shape change in two- and three-dimensional hydrogel structures. *Adv Mater* **25**, 1541-1546, (2013).

174 Osada, Y., Okuzaki, H. & Hori, H. A Polymer Gel with Electrically Driven Motility. *Nature* **355**, 242-244, (1992).

175 Kobatake, S., Takami, S., Muto, H., Ishikawa, T. & Irie, M. Rapid and reversible shape changes of molecular crystals on photoirradiation. *Nature* **446**, 778-781, (2007).

176 Yuan, C., Roach, D. J., Dunn, C. K., Mu, Q., Kuang, X., Yakacki, C. M., Wang, T. J., Yu, K. & Qi, H. J. 3D printed reversible shape changing soft actuators assisted by liquid crystal elastomers. *Soft Matter*, (2017).

177 Shenoya, D. K., III, D. L. T., Srinivasanb, A., Kellerc, P. & Ratnaa, B. R. Carbon coated liquid crystal elastomer film for artifcial muscle applications. *Sensors and Actuators A* **96** 184-188, (2002).

178 Mao, Y., Ding, Z., Yuan, C., Ai, S., Isakov, M., Wu, J., Wang, T., Dunn, M. L. & Qi, H. J. 3D Printed Reversible Shape Changing Components with Stimuli Responsive Materials. *Sci Rep* **6**, 24761, (2016).

179 Yakacki, C. M., Saed, M., Nair, D. P., Gong, T., Reed, S. M. & Bowman, C. N. Tailorable and programmable liquid-crystalline elastomers using a two-stage thiol–acrylate reaction. *RSC Adv.* **5**, 18997-19001, (2015).

180 Huang, L., Jiang, R., Wu, J., Song, J., Bai, H., Li, B., Zhao, Q. & Xie, T. Ultrafast Digital Printing toward 4D Shape Changing Materials. *Adv Mater* **29**, (2017).

181 Wu, J., Zhao, Z., Kuang, X., Hamel, C. M., Fang, D. & Qi, H. J. Reversible shape change structures by grayscale pattern 4D printing. *Multifunct. Mater.*, (2018).

182 Jamal, M., Zarafshar, A. M. & Gracias, D. H. Differentially photo-crosslinked polymers enable self-assembling microfluidics. *Nat Commun* **2**, 527, (2011).

183 Deng, T., Yoon, C., Jin, Q., Li, M., Liu, Z. & Gracias, D. H. Self-folding graphene-polymer bilayers. *Applied Physics Letters* **106**, (2015).

184 Wu, J., Zhao, Z., Hamel, C. M., Mu, X., Kuang, X., Guo, Z. & Qi, H. J. Evolution of material properties during free radical photopolymerization. *Journal of Mechanics and Physics of Solids* **Submitted**, (2017).

185 Swinehart, D. F. The Beer-Lambert Law. *J. Chem. Educ.* **39**, 333, (1962).

186 Cabral, J. T. & Douglas, J. F. Propagating waves of network formation induced by light. *Polymer* **46**, 4230-4241, (2005).

187 Vitale, A. & Cabral, J. Frontal Conversion and Uniformity in 3D Printing by Photopolymerisation. *Materials* **9**, 760, (2016).

188 Allensworth, J. R., Liu, Y., Braun, H., Genzer, J. & Dickey, M. D. In-plane deformation of shape memory polymer sheets programmed using only scissors. *Polymer* **55**, 5948-5952, (2014).

189 He, Y., Zhou, Y., Liu, Z. & Liew, K. M. Pattern transformation of single-material and composite periodic cellular structures. *Materials & Design* **132**, 375-384, (2017).

190 Liu, J., Gu, T., Shan, S., Kang, S. H., Weaver, J. C. & Bertoldi, K. Harnessing Buckling to Design Architected Materials that Exhibit Effective Negative Swelling. *Adv Mater* **28**, 6619-6624, (2016).

191 Vasiliev, V. V., Barynin, V. A. & Rasin, A. F. Anisogrid lattice structures-**survey of development and application**. *Composite Structures* **54**, 361-370, (2001).

192 Santo, L., Quadrini, F., Accettura, A. & Villadei, W. Shape Memory Composites for Self-deployable Structures in Aerospace Applications. *Procedia Engineering* **88**, 42-47, (2014).

193 Liu, Y. J., Du, H. Y., Liu, L. W. & Leng, J. S. Shape memory polymers and their composites in aerospace applications: a review. *Smart Materials and Structures* **23**, (2014).

194 Zarek, M., Mansour, N., Shapira, S. & Cohn, D. 4D Printing of Shape Memory-Based Personalized Endoluminal Medical Devices. *Macromol Rapid Commun* **38**, (2017).

195 Lendlein, A. & Langer, R. Biodegradable, Elastic Shape-Memory Polymers for Potential Biomedical Applications. *SCIENCE* **296**, 1673, (2002).

196 Ware, T., Simon, D., Hearon, K., Liu, C., Shah, S., Reeder, J., Khodaparast, N., Kilgard, M. P., Maitland, D. J., Rennaker, R. L., 2nd & Voit, W. E. Three-Dimensional Flexible Electronics Enabled by Shape Memory Polymer Substrates for Responsive Neural Interfaces. *Macromol Mater Eng* **297**, 1193-1202, (2012).

197 Yu, Z., Zhang, Q., Li, L., Chen, Q., Niu, X., Liu, J. & Pei, Q. Highly flexible silver nanowire electrodes for shape-memory polymer light-emitting diodes. *Adv Mater* **23**, 664-668, (2011).

198 Li, Y. C., Zhang, Y. S., Akpek, A., Shin, S. R. & Khademhosseini, A. 4D bioprinting: the next-generation technology for biofabrication enabled by stimuli-responsive materials. *Biofabrication* **9**, 012001, (2016).

199 Momeni, F., M.Mehdi Hassani.N, S., Liu, X. & Ni, J. A review of 4D printing. *Materials & Design* **122**, 42-79, (2017).

200 Santo, L., Quadrini, F., Squeo, E. A., Dolce, F., Mascetti, G., Bertolotto, D., Villadei, W., Ganga, P. L. & Zolesi, V. Behavior of Shape Memory Epoxy Foams in Microgravity: Experimental Results of STS-134 Mission. *Microgravity Science and Technology* **24**, 287-296, (2012).

201 Lotkov, A. I., Kashin, O. A., Kudryashov, A. N. & Krukovsky, K. V. Structure and properties of self-expanding intravascular NiTi stents doped with Si ions. *Materials Today: Proceedings* **4**, 4647-4651, (2017).

202 Imbalzano, G., Tran, P., Ngo, T. D. & Lee, P. V. S. A numerical study of auxetic composite panels under blast loadings. *Composite Structures* **135**, 339-352, (2016).

203 Lee, J. H., Singer, J. P. & Thomas, E. L. Micro-/nanostructured mechanical metamaterials. *Adv Mater* **24**, 4782-4810, (2012).

204 Yuk, H., Lin, S., Ma, C., Takaffoli, M., Fang, N. X. & Zhao, X. Hydraulic hydrogel actuators and robots optically and sonically camouflaged in water. *Nat Commun* **8**, 14230, (2017).

205 van Oosten, C. L., Bastiaansen, C. W. & Broer, D. J. Printed artificial cilia from liquid-crystal network actuators modularly driven by light. *Nat Mater* **8**, 677-682, (2009).

206 Gladman, A. S., Matsumoto, E. A., Nuzzo, R. G., Mahadevan, L. & Lewis, J. A. Biomimetic 4D printing. *Nat Mater* **15**, 413-418, (2016).